UNIVERSITA' DELLA CALABRIA

Dipartimento di Ingegneria Meccanica Energetica e Gestionale

Dottorato di Ricerca in

Ingegneria Civile ed Industriale

CICLO

XXXIII (2017-2020)

The Role of Physics Based Modeling of Macro/Micro Machining Operations in the Era of Electric Vehicles Revolution.

Settore Scientifico Disciplinare: ING-IND/16

Coordinatore: Ch.mo Prof. Enrico Conte

Firma_____

Supervisore/Tutor: Ch.mo Prof. Domenico Umbrello

Firma_____

Dottorando: Dott. Sergio Rinaldi

Firma _____

UNIVERSITA' DELLA CALABRIA

Dipartimento di Ingegneria Meccanica Energetica e Gestionale

Dottorato di Ricerca in

Ingegneria Civile ed Industriale

CICLO

XXXIII (2017-2020)

The Role of Physics Based Modeling of Macro/Micro Machining Operations in the Era of Electric Vehicles Revolution.

Settore Scientifico Disciplinare: ING-IND/16

Coordinatore: Ch.mo Prof. Enrico Conte

Firma____ Firma oscurata in base alle linee guida del Garante della privacy

Supervisore/Tutor: Ch.mo Prof. Domenico Umbrello

Firma____ Firma oscurata in base alle linee guida del Garante della privacy

Dottorando: Dott. Sergio Rinaldi

Firma Firma oscurata in base alle linee guida del Garante della privacy
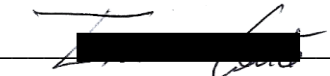
UNIVERSITA' DELLA CALABRIA

Dipartimento di Ingegneria Meccanica Energetica e Gestionale

Dottorato di Ricerca in

Ingegneria Civile ed Industriale
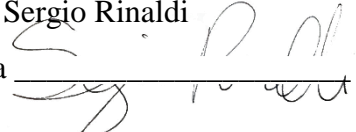
CICLO

XXXIII (2017-2020)

The Role of Physics Based Modeling of Macro/Micro Machining Operations in the Era of Electric Vehicles Revolution.

Settore Scientifico Disciplinare: ING-IND/16

Coordinatore: Ch.mo Prof. Enrico Conte

Firma_____

Supervisore/Tutor: Ch.mo Prof. Domenico Umbrello

Firma_____

Dottorando: Dott. Sergio Rinaldi

Firma_____

University of Calabria

DIMEG – Department of Mechanical, Energy and Management Engineering

Ph.D. Thesis

XXXIII Cycle (2017-2020)

Ph.D. in Civil and Industrial Engineering

The Role of Physics Based Modeling of Macro/Micro Machining Operations in the Era of Electric Vehicles Revolution.

Candidate

Sergio Rinaldi

Ph.D. Coordinator: Supervisor:

Prof. Enrico Conte   **Prof. Domenico Umbrello**

To my family, with a particular regard to my father,
if I am so austenite it is surely his merit.

Looking up from here, it's as if
each flame were a small dream from
each person. They're like a bonfire of dreams
don't they? I'm just a temporary visitor
taking comfort from the flame…
(Guts - Berserk)

A guardarle così sembra che dentro ognuna di
quelle piccole luci dimorino i loro piccoli sogni e i loro
ideali. Il falò dei sogni... [...] Uno per uno sono arrivati
qui portando le loro piccole fiammelle. Poi, per non lasciar
spegnere quei piccoli fuochi li lanciano in uno più grande...
in una fiamma enorme chiamata Grifis. Però il mio fuoco
non è qui. Può darsi che senza riflettermi mi sia solo
fermato a scaldarmi a quel falò...
(Gatsu - Berserk)

Acknowledgments

At the end of this path, I can surely assert that I am a very lucky man. I met lots of people that were and are still important for me, and an incredible number of fantastic friends.

At first, I would thank my family, my mother, my father and my sister Gabriella, I am sorry that I could not dedicate my master thesis to you, but once I decided to attend the Ph.D. course, it was clear that you will be in the first page of this thesis.

Moreover, I want to extend these thanks to all my relatives, in particular to aunt Anna, that is the one that stressed me much more with her support during the Ph.D. period.

An important mention is also for my grandparents, above all for you Vincenzo, you gave me your support from wherever you are, I can guarantee that I felt it every single day.

I thank plentifully Dr. Domenico Umbrello, because every time that I got a knock on my back throughout my period as researcher, he was there. Furthermore, I owe a deep sense of gratitude for Dr. Shreyes Melkote, for his support during my research period in the USA.

I am extremely thankful to all my friends, and the first that I want to mention are you Andrea, Ercole and Niccolò, you are my historical friends and you always gave me your support, not only during my research period.

Another mention goes to Stano, I thank you for dragging me when I was uncertain for all the problems that I encountered to join the Ph.D., it was essential. Without your help, I surely left it before beginning.

Then is the turn of my friends from Kraken, you are all important for me, but I must give a special thanks to Tiziana and Angelo, that are the ones that chose my same path in research. You can understand better than any other how much is arduous to cross this road.

The period in the USA was probably the most terrible challenge in my life, and two people in particular assisted me to face it up. My dear Natalia and Crystal, as promised, you are in my acknowledgements, I will not forget how much you helped me.

I also want to give my acknowledge to Vittorio, at first a colleague and then a friend, our walks around the UNICAL bridge speaking about our future were special for me.

Last but don't least, I want to thank Stefania. Your support was fundamental during the last year and thanks to you I found the real love.

This page intentionally left blank.

Index

List of Figures

List of Tables

Sommario

Al giorno d'oggi, la rivoluzione dei veicoli elettrici ha mostrato un inarrestabile fermento, guidata dalle pionieristiche tecnologie sviluppate da *Tesla Motors*, *BYD Auto*, e vari altre compagnie che per prime le hanno adottate. Ciò è stato causato da una tendenza crescente che porterà i motori a combustione a divenire una tecnologia obsoleta in un periodo di tempo relativamente breve.

Questo evento influenzerà profondamente il segmento dell'industria automobilistica che concerne la produzione dei motori a cilindri monoblocco. Questi rappresentano uno dei sottoinsiemi di mercato che maggiormente coinvolge i processi di asportazione di materiale tradizionali, a causa della complessità geometrica intrinseca del blocco motore. Tale evenienza costringerà le industrie che realizzano manufatti mediante processi di taglio e i produttori di attrezzature tecnologiche per realizzare operazioni di asportazione di materiale, al fine di affrontare tale tendenza discendente.

I segmenti di mercato attualmente in crescita e allo steso tempo interessati da processi di taglio coinvolgono principalmente le industrie biomedicali, aeronautiche/aerospaziali e della difesa. Pertanto, spostarsi in un segmento di mercato così diverso, implica che le strategie di produzione e vendita iniziali delle compagnie interessate debbano essere riviste seguendo le nuove richieste, al fine di rispettare i vincoli produttivi tipici di questi nuovi campi di interesse. In particolare, considerando gli elevati standard qualitativi che i prodotti finiti devono soddisfare per poter operare in tali settori, è fondamentale che questi manifestino prestazioni di alto livello e che i processi produttivi siano altamente ripetibili. Inoltre, i manufatti devono sopportare differenti generi di carichi di esercizio, anche ciclici e ad elevate temperature, devono essere durevoli e deve inoltre essere considerata una elevata sicurezza per l'operatore già nella fase di progettazione.

Larga parte delle caratteristiche dei prodotti descritti possono essere ottenute mediante trattamenti secondari o, mirando alla riduzione delle fasi del processo produttivo, scegliendo correttamente i parametri di processo, considerando l'integrità superficiale dei componenti lavorati. In questo contesto, al fine di evitare lunghe e dispendiose campagne sperimentali, è possibile sviluppare dei modelli numerici affidabili, da validare mediante l'utilizzo di piani degli esperimenti ridotti, che possano rappresentare delle linee guida per la progettazione di strategie e metodologie di produzione più efficaci. Inoltre, basando la modellazione del flusso plastico del materiale sui fenomeni metallurgici che concorrono durante i processi deformativi, diventa uno strumento anche più efficace per comprendere le modifiche microstrutturali, sia positive che negative, che possono avvenire durante i processi produttivi. Nonché, ciò rappresenta un mezzo importante per poter misurare indirettamente i vari fenomeni intriseci che avvengono nel materiale processato, anche

quando le comuni strumentazioni non lo permettono, raggiungendo potenzialmente un livello di conoscenza di tali fenomeni ancora più profondo.

Abstract

Driven by the pioneering prowess performed by *Tesla Motors*, *BYD Auto*, and various other first adopters, the Electric Vehicles (*EVs*) Revolution has gained an unstoppable momentum. This caused a progressive trend that will bring, in a relatively brief period, the Internal Combustion Engine (*ICE*) to become an outdated technology. This occurrence will deeply influence the segment of the automotive industry that pertains the engine cylinder blocks manufacturing. The latter represents one of the market subsets that is more interested by the traditional material removing operations, due to the so complex shape of the engine block. This eventuality will force the companies that work with machining operations and the manufacturers of cutting tools to intercept new market segments, aiming to face this descendant trend.

The market segments that are actually growing and are also broadly interested by machining operations principally involve biomedical, aeronautic/aerospace, and defense industries. Moving in a so different market subsystem implies that the original marketing and manufacturing strategies need to be revised, following the new specific requirements, in order to respect the production constraints that are typical of these new field of interest. In particular, considering the higher quality standards that products must be satisfied to operate in these sectors, huger performances for the final products and higher process repeatability need to be guaranteed. Moreover, strong resistance to the different operating loads, higher components duration, and more elevated safeness for the operators have to be considered in process/product design phase.

A large part of the described product characteristics can be obtained by secondary treatments, or, aiming to reduce the production operations, the same result can be reached properly optimizing the process parameters, taking into account the surface integrity characteristics of the processed parts. In this context, in order to avoid long and expansive experimental campaigns, an appropriately validated numerical model represents an effective instrument to give guidelines concerning the best production strategies to bail out the most performing conditions from the manufacturing process and from the final product performances. Furthermore, when the numerical model is coupled with a physics based representation of the material plastic flow, it became an even more efficacious mean to comprehend all the positive and negative metallurgical alterations that can occur during the workpiece processing. Besides, it represents a fundamental tool to deeply analyze the different microstructural phenomena that results at the end of the machining operations, allowing to achieve a level of consciousness of the inner effects that is extremely difficult or even impossible to be attained with common experimental measurement procedures.

CHAPTER I

In the first chapter, the main topics discussed in the PhD thesis research work are introduced. A general overview of the effect of the studies on the global market is reported, focusing on the opportunities for the involved stakeholders to invest in new market segments, reporting a preliminary analysis of the Electric Vehicles Revolution economic impact in possible future scenarios, according with the statistical analysis of the market future trends. The dissemination scheme of the investigated topics in the subsequent chapters is also reported, providing a general outline of the researches carried out during the overall PhD period, with particular emphasis on the achieved research objectives.

General Introduction

In a world where energy saving and environment preservation are primary concerns, the technologies related to Electric Vehicles (EVs) are gaining a growing consideration. They were very popular and reasonably sold in '20s. Nevertheless, when the Internal Combustion Engine (ICE) began to thrive, a strong reduction of EVs selling were relieved in the global market, until the 1933 when the number of sold EVs faded until nearly zero. In particular, this dropping was primarily due to the slower speed and higher sold prices EVs respect to their ICE counterpart [1]. In last decades, important factors encouraged the revival of EVs, such as competitive energy cost, energy independence, and ecological protection, vividly reducing the air pollution in congested urban areas. Furthermore, the upcoming shortage of gasoline productions, its costs and supplying limitations encouraged people to take into account EVs as a possible alternative transportation. Moreover, considering that electricity can be generated from many different sources, these vehicles represent a more flexible alternative than the fuel ones [2, 3]. Consequently, in next years the production of ICE based vehicles is expected to decade, strongly influencing all the related market segment. In Fig. 1 are reported some predicting trends concerning EVs vs ICE selling taken from [4, 5]. Here it is possible to see that, despite the substantial quantitative differences in the data predicted from different organizations, in the long period the overall growing trend of vehicles selling will majorly accommodates the various typology of EVs.
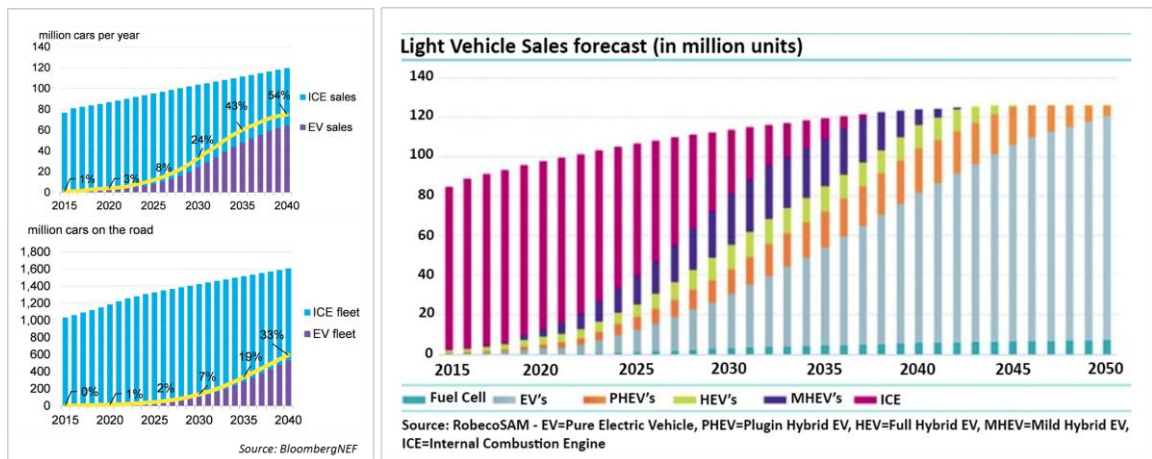
Fig. 1 Vehicle market evolution predictive trends [4, 5].

Downstream of the considered data, a market contraction concerning *ICE* based vehicles is expected and this will force all the involved businesses to intercept new market segments, rebuilding their production and selling strategies and reengineering their products and services capabilities.

Moreover, it is worth to highlight that the predictive trends that inspired the research works subsequently presented were relieved before the pandemic due to *COVID-19* disease. Hence, the proposed considerations need to be delayed of a certain period referring to the market recovery that will occur once the critic situation will be damped, hoping for the best and fastest resolution of the market crisis. Howsoever, this contingency will be exhaustively discussed in Paragraph 1.1.

1.1. Economic Impact of *COVID-19* – Estimation of Scenarios

The *COronaVIrus Disease 2019* (*COVID-19*) is an infectious disease coming from Severe Acute Respiratory Syndrome COronaVirus 2 (SARS-CoV-2). It was first identified in December 2019 in Wuhan, Hubei, China, and has resulted in an ongoing pandemic able to quickly involve the entire planet, killing over 100000 individuals and infecting more than 3 million people in the sole first 4 months [6]. As businesses have shut down to fulfil the government stay-at-home restrictions, the main part of the workers have been laid off and many industries were left upended. The subsequent acute shock has the potential to trigger a global economic crisis of significant dimensions, potentially affecting all industries in the planet [7]. The recession expected after the global crisis will reduce the consumptions by multi-digit percentages in 2020, followed by a slow recovery that will lag behind Gross Domestic Product (*GDP*) rebound by one or two years. The duration and

severity of economic recovery is being compared to a *V*, *U*, *W* or *L* shape function, as visible in Fig. 2.
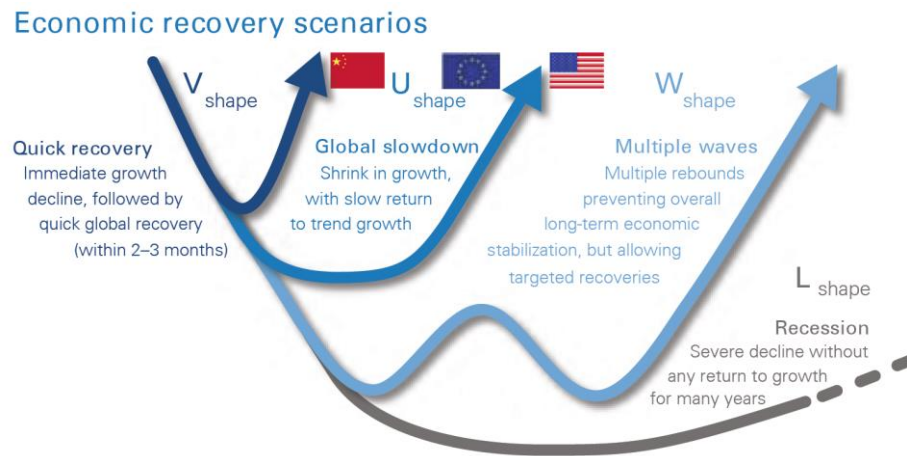
Fig. 2 Different scenarios of duration and slope of economic recovery.

A "*V-shaped*" recovery would be fast and without severe long-term effects, a "*U-shaped*" recovery would imply lower short-term growth rates and consequently more significant effects in the medium term. Differently from these relatively stable recovery trends, a "*W-shaped*" pattern would incorporate multiple waves of partial recoveries and setbacks, lengthening the time to an overall recovery. Finally, the "*L-shaped*" curve describes a serious recession with incalculable long-term effects on the whole economy, low *GDP* growth rates, and only a very long-term return to the pre-crisis status [8]. Focusing on Automotive, Aerospace/Aeronautic and Defense industries, they will all suffer this economic stroke, resulting in a delay of the previously discussed rising and descending trends, waiting for the market rebounds. Concerning Automotive and Aerospace/Aeronautic industries, their representative post-*COVID-19* predicted evolution trends are visible in Fig. 3 and Fig. 4, respectively [9, 10].
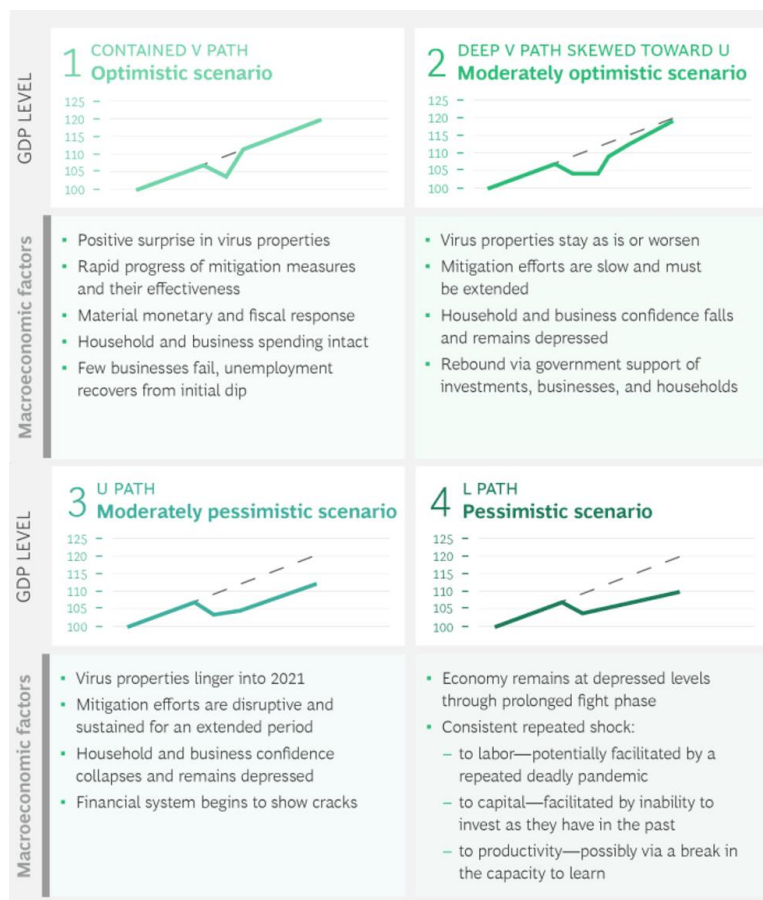
Fig. 3 Predicted scenarios for automotive market crisis recovery [9].
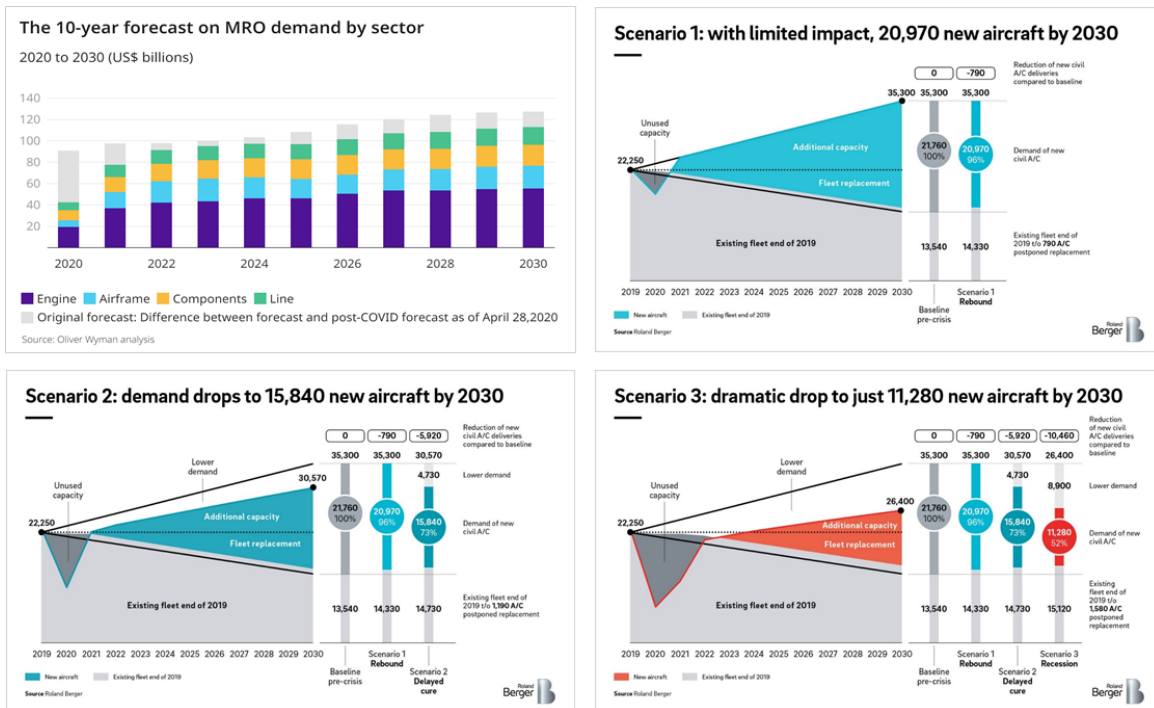
Fig. 4 Predicted scenarios for Aeronautic/Aerospace market crisis recovery [10, 11].

1.2. Machining Operations – New Marketing Strategies

The uncertainty about the future direction of the powertrain, is slowly causing turmoil among the traditional engines production stakeholders. In order to deal with this occurrence, they will need to adapt their products/services to the next generation platforms and expand their portfolio to new and more advantageous market segments. On the manufacturing point of view, the *EV*s show very low complexity than their *ICE* based competitors. An electric car can be divided into three main components, namely the electric motor, a battery pack and a transmission. The battery pack has not any moving part and the electric energy is obtained from them via chemical processes that aim to power the motor. It transfers power to the wheels through a small transmission (typically a single speed transmission for *Tesla* vehicles). Consequently, the overall requirements concerning the machining operations of automotive components are extremely lower compared to the *ICE* vehicles production and regard above all the motor and minimally the transmission. Therefore, among all the different businesses that will be interested from the market contraction that is expected due to the *IGE* selling shortage. The presented research work will focus on the ones that offer services and products concerning machining operations, such as cutting tools producers, machining centers manufacturers, mechanical workshops, steelworkers and so on [12, 13]. The focus of this work on machining processes is mainly due to the enormous reduction of the machining requirements that are necessary to manufacture *EV*s than the *ICE* vehicles. In order to show the differences in machining operations requirements to manufacture both electric vehicle and internal combustion motors. In Fig. 5 are reported all the process operations needed to manufacture *EV*s motors and transmissions, while in Fig. 6 are shown the sole machining operations required to build up an *ICE*.
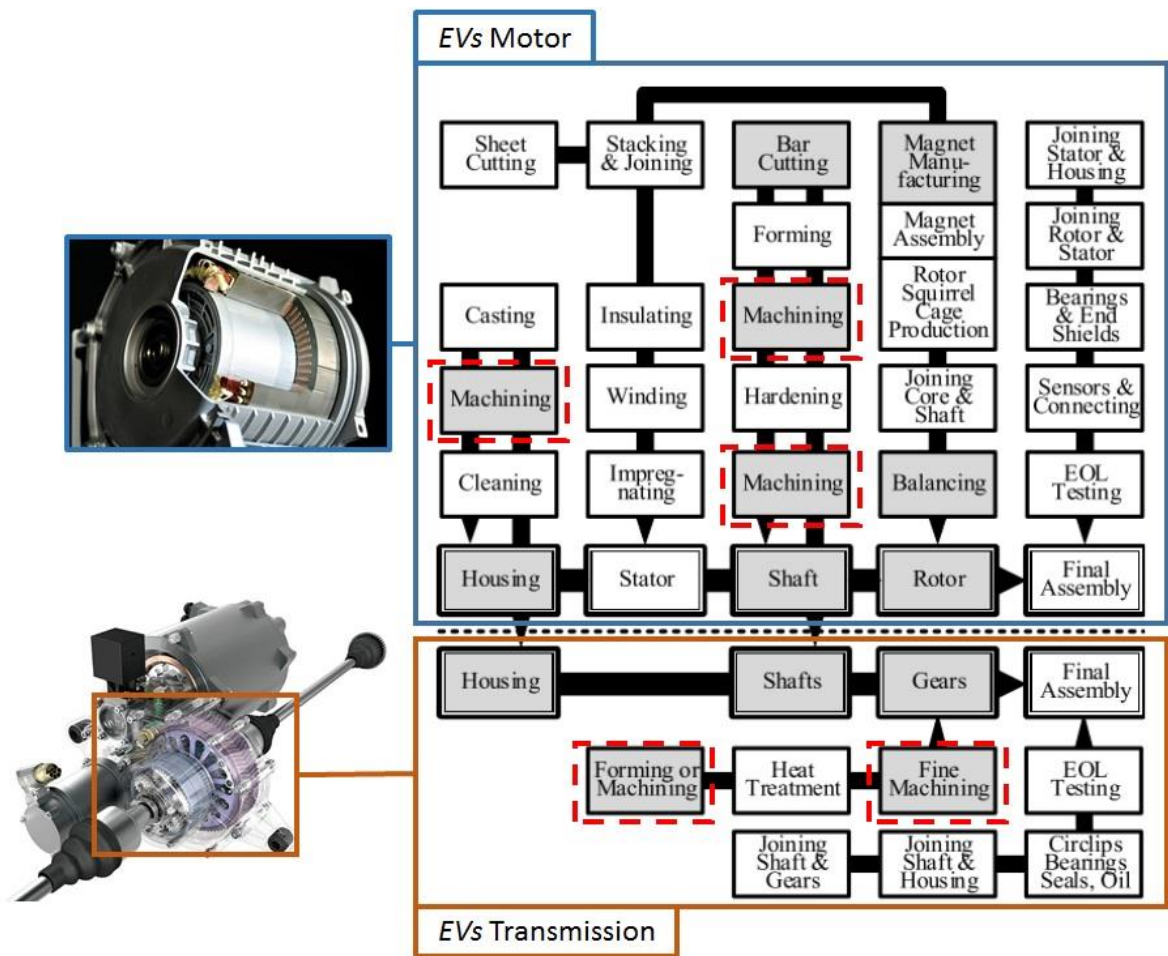
Fig. 5 Overview of the production processes of EVs motors and transmissions with marked machining operations [13].

Considering the previously discussed issues, it is well legitimate to assume that the perused stakeholders will invest their efforts following the direction of the growing up market section that involves machining structured systems. Taking into account the actual predictions, the most promising sectors that involve machining operations and are showing substantial growing up trends in the global market are principally the ones that involves precision machining and hard-to-cut alloys machining. In particular, the most promising sectors result to be the biomedical industries for what concern the production of higher performances prostheses, aeronautic/aerospace and defense industries for what concerns the manufacturing of high performance alloy components (Fig. 7) [14–16].

Fig. 6 Scheme of 4-cylinder block manufacturing instructions, (a) designing features, (b) work-cycle flow of machining elements (*fme*), and (c) priority constraints of feature machining elements [12].

Name	No.	Feature Machining Elements (*fme*)
Top Face	1	Rough milling (fme_{11}), semi-finish milling (fme_{12}), finish milling (fme_{13})
Front Face	6	Rough milling (fme_{61}), semi-finish milling (fme_{62}), finish milling (fme_{63})
Left Face	10	Rough milling (fme_{101}), semi-finish milling (fme_{102}), finish milling (fme_{103})
Right Face	18	Rough milling (fme_{181}), semi-finish milling (fme_{182}), finish milling (fme_{183})
Rear Face	22	Rough milling (fme_{221}), semi-finish milling (fme_{222}), finish milling (fme_{223})
Bottom Face	28	Rough milling (fme_{281}), semi-finish milling (fme_{282}), finish milling (fme_{283})
Cylinder Hole	2	Rough boring (fme_{21}), semi-finish boring (fme_{22}), finish boring (fme_{23}), honing (fme_{23})
Composite Hole 1	3	Drilling (fme_{31}), tapping (fme_{32}), expanding (fme_{33})
Long Oil Hole	23	Drilling (fme_{231}), expanding (fme_{232}), reaming (fme_{233})
Pin Hole	33	Drilling (fme_{331}), expanding (fme_{332}), reaming (fme_{333})
Tappet Hole	34	Drilling (fme_{341}), expanding (fme_{342}), reaming (fme_{343})
Composite Hole 2	8	Drilling (fme_{81}), reaming (fme_{82}), tapping (fme_{83})
2-Φ30	9	Rough boring (fme_{91}), finish boring (fme_{92})
Water Hole	11	Rough tapping (fme_{111}), finish tapping (fme_{112})
Cam Shaft Hole	24	Rough boring (fme_{241}), finish boring (fme_{242})
Crank Shaft Hole	25	Rough boring (fme_{251}), finish boring (fme_{252})
Φ30	26	Rough boring (fme_{261}), finish boring (fme_{262})

Name	No.	Feature Machining Elements (*fme*)	Name	No.	Feature Machining Elements (*fme*)
16-M12	4	Drilling (fme_{41}), tapping (fme_{42})	Angle Oil Holes in Top Face	5	Drilling (fme_{51})
18-M8	7	Drilling (fme_{71}), tapping (fme_{72})	8-M10	12	Drilling (fme_{121}), tapping (fme_{122})
2-M8	13	Drilling (fme_{131}), tapping (fme_{132})	M16	14	Drilling (fme_{141}), tapping (fme_{142})
NPT1/16	15	Drilling (fme_{151}), tapping (fme_{152})	NPT1/4	16	Drilling (fme_{161}), tapping (fme_{162})
Angle Oil Hole	17	Drilling (fme_{171})	4-M12	19	Drilling (fme_{191}), tapping (fme_{192})
8-M10	20	Drilling (fme_{201}), tapping (fme_{202})	2-M8	21	Drilling (fme_{211}), tapping (fme_{212})
8-M10	27	Drilling (fme_{271}), tapping (fme_{272})	4-M10	29	Drilling (fme_{291}), tapping (fme_{292})
Crank Shaft & Angle Oil Hole	30	Drilling (fme_{301})	10-M14	31	Drilling (fme_{311}), tapping (fme_{312})
18-M8	32	Drilling (fme_{321}), tapping (fme_{322})	Slot	35	Milling (fme_{351})

In the referred sectors, the final product requirements are strongly different respect to the automotive application, then new researches need to be designed and carried forward, bracing the stakeholders for the new challenges that will be tackled, gathering know-how about the new technologies and manufacturing strategies that will be faced. In detail, the aerospace/aeronautic, defense, and biomedical product requirement consist above all in high affordability and repeatability of the manufacturing processes, high quality and operative performances of the produced artefacts and high reliability during their useful life. Substantially, an overall superior product and processing quality have to be guaranteed [17]. Aiming to obtain these characteristics, high efficiency alloys are frequently employed. A significant part of these, because of their superior thermo-mechanical properties and affinity with the machining tools, are enclosed into the set of

the so called hard-to-cut materials [18]. Consequently, before they can be processed into the manufacturing chain, deep analyses and researches have to be carried out in order to get solid guidelines about the proper design of the process and quality of the artifacts. In such way, it is possible to yield the involved processes to manufacture more performing products, and to avoid the common defects that can occur on a badly processed workpiece.
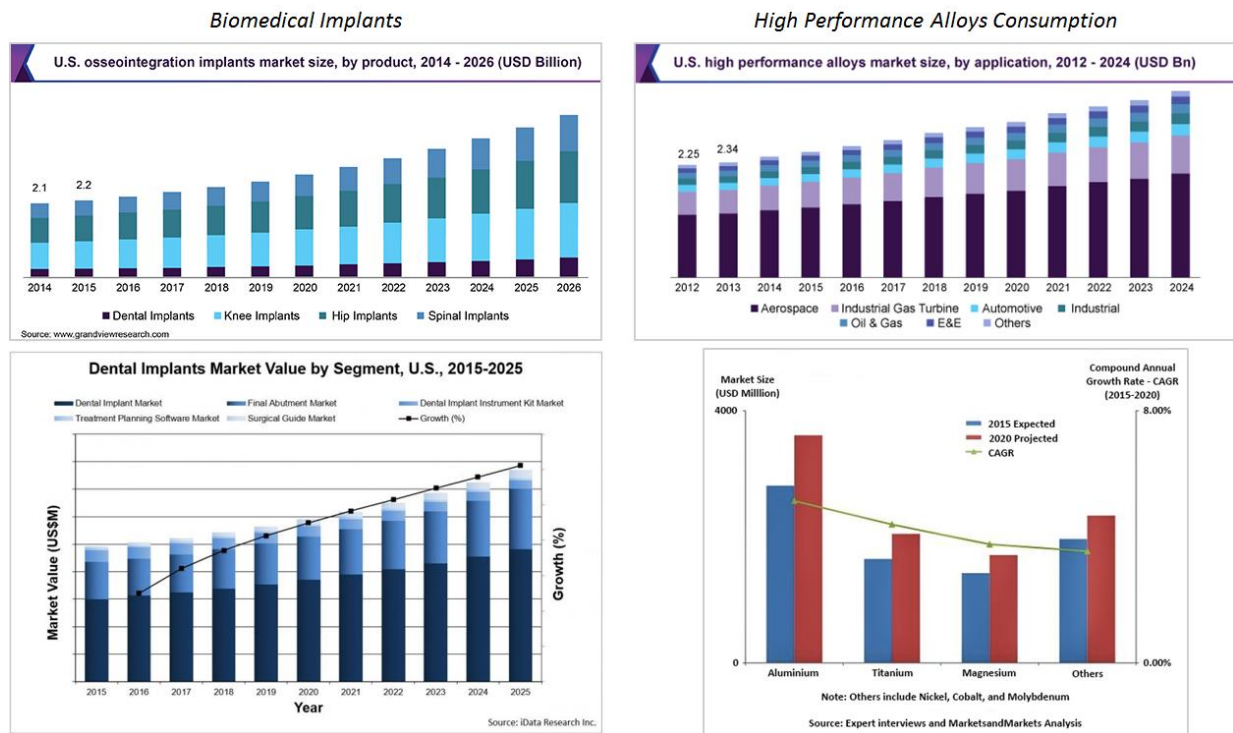
Fig. 7 Predictive trends of the evolution of the biomedical implants and high performance alloys consumptions market [19–22].

1.3. Machining Operations – Modeling to Enhance Features

In general, the rupture of high-performance metal artefacts is due to wear, corrosion or fatigue, and these so different kind of failure phenomena have some common points. In particular, they all involve the generation and propagation of some kind of defect on the artefact's surfaces. Therefore, a proper design of the surface inner conditions represents an interesting strategy to find higher performance products [23].

The local properties of a general metal material can be improved by changing the spatial distribution of its microstructural elementary structures, opportunely modifying the production strategies, and leading to the manufacturing of Functionally Graded Materials (*FGMs*). The latter represents an important mean to reduce the cost and the final weight of the component, while its

operative features are guaranteed or even improved [24]. In this context, machining processes represent an interesting tool to locally induce Severe Plastic Deformations (*SPD*) on a manufactured part, causing considerable microstructural modifications, that, if properly structured, they can allow to achieve final products of higher quality [25, 26].

The desired product performances, or at least a good compromise solution, can be obtained with a correct set up of the finishing/semi-finishing parameters, focusing on microstructural conditions of the processed material after the manufacturing processes.

Severe deformation processes significantly influence the microstructural status of a general polycrystalline material. In particular, the machining-induced microstructural modifications, both on the processed surface and subsurface, can be considered as a local *SPD*, and modelled as such. Under large deformation conditions, many metallurgical phenomena pertain the processed surface, locally modifying the macroscale behavior of the involved material [27]. Exploiting the common means of analysis, it can be extremely difficult or even impossible to have a deep and precise comprehension of the metallurgical behavior of the material once it is subjected to the flow stress induced by plastic deformations. In this context, physics based modeling of the material flow represents a fundamental means to make up for the lack of capabilities of measurement instrumentations, and in addition allows to investigate the metallurgical phenomena active during the manufacturing process. In such way, it is possible to obtain a deeper and wider comprehension of the physics phenomena that occur inside the material during the plastic flow and to predict the resulting quality of the processed surface [28].

In this PhD thesis three case studies were selected in accordance with the previously highlighted topics that are object of industrial and scientific interest. These case studies represent the body of the presented work and they will be deeply discussed through the chapters. In particular, the first case study regards the study of the machining process of Nickel-Chromium superalloy (*Waspaloy*), and has applications that are strictly related to the production of high-performance jet engines. The second case study concerns the micromachining of Commercially Pure Titanium (*CP-Ti*) that is commonly and principally employed for biomedical applications, howsoever it has also a minimum number of aeronautic/aerospace applications. The third one regards the machining process of the most commonly used titanium alloy (*Ti6Al4V*), that claims an "all purpose" functionality and shows an extremely broad extension of applications, involving, among the others, both biomedical and aerospace/aeronautic industries.

1.4. Research Objectives

The discussed predictive trends highlighted the growing interest in researching the best way to produce innovative and high-performance components, as well as new and more repeatable production processes to be implemented into the manufacturing chains. Further investigations are also necessary to understand the plastic behavior of the processed parts under different machining conditions. Besides, it was also emphasized the importance to improve the quality of the product, in order to satisfy the severe requests that are indispensable in higher performance artefacts produced using the chosen materials, with a main focus on biomedical and aerospace/aeronautic industries. The presented studies aim to give important guidelines and generate databases that represent the foundations to manufacture featured products that can be competitive in their own specific market segment. In order to meet all the performance requirement of final products and industrial processes, an extremely useful tool is represented by the numerical modeling, that will be broadly exploited and discussed in this research work. In this perspective, the application of physics based flow stress modeling methodologies is a strong mean to properly understand the thermo-mechanical behavior of the manufactured parts. It provides a profound knowledge of the microstructural evolution of the material that is deformed by the processing tools, permitting to predict not only the macroscopic variables of industrial interests, but also an in-depth comprehension of the metallurgical status of the workpiece, during the machining process and subsequently to it. The latter is the base to correctly choose the process parameters that can lead to the manufacturing of components with engineered surfaces, that show higher operative performances and are evaluable in terms of surface integrity. Three case studies of huge industrial importance were taken into account, for a broad range of outstanding application and giving the instrument to potentially enlarge their employment, because of the obtained information on manufacturability and process optimization. In Fig. 8 are summarized the details concerning the chosen case studies and the investigation approaches that were exploited to analyze the metallurgical modifications induced by the machining process.

Taking into account the main design improvement opportunity highlighted by the predicting trends, the main objectives of this research are:

- to investigate the machinability and study the surface integrity of *Waspaloy* machined parts after semi-finishing machining processes under different cutting parameters and lubri-cooling methods;

- to investigate the machinability and study the surface integrity of *CP-Ti* macro/micro machined parts after semi-finishing machining processes under different cutting parameters and process conditions;

- to investigate the machinability and study the surface integrity of *Ti6Al4V* machined parts after semi-finishing machining processes under different cutting parameters and lubri-cooling methods;

- to define the mechanical behavior flow stress of all the investigated materials in order to simulate the specific machining operations;

- to perform further investigations to assess the surface integrity in terms of microstructure deformation shape and hardness changes;

- to develop physically-based model of all the investigated materials to simulate the specific machining operations;

- to describe the physical reasons of the microstructural variations and to understand their effects on hardening or softening governing phenomena;

- to predict and analyze the main fundamental variables such as cutting forces and temperature and the microstructural modifications occurring during the manufacturing processes.
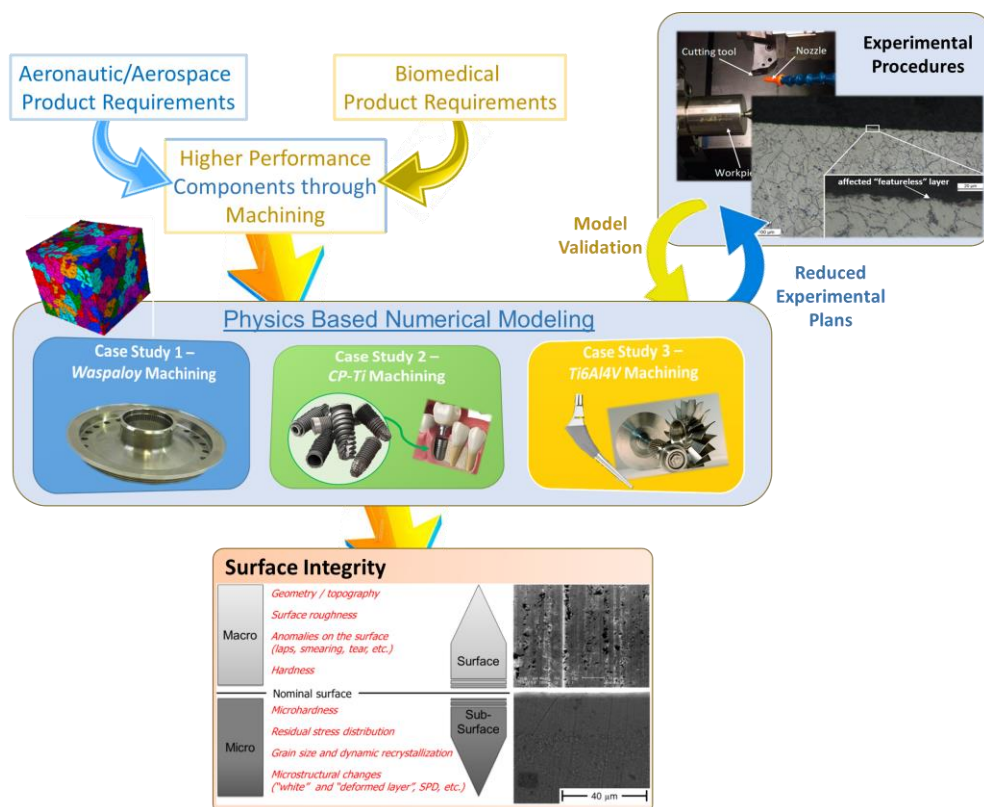
Fig. 8 Representative scheme of the research activities developed in this Ph.D. thesis.

1.5. Dissertation Outline

The schematic representation of this PhD thesis workflow is reported in a flow chart, as visible in Fig. 9. It reports the organization of the analyzed topics (state-of-the-art), and the experimental and numerical procedures that involved each case study.

Chapter II shows a literature review that at first aims to generally analyze the machining processes and their numerical modeling procedures. The chapter highlights the fundamental importance of the proper reproduction of the plastic flow stress behavior in order to properly define a robust and reliable numerical model.

Chapter III details the basis of the inner stress modeling and then focus on the main physics phenomena that promotes the metallurgical modifications occurring during the plastic flow at micro/nano scale and result in the material general thermos-visco-plastic flow behavior. Furthermore, it is reported a broad description of the main physics based modeling methodologies able to simulate these effects. A focus on machining operation is also stated, in order to describe the occurrence of these phenomena during the machining process.

Chapter IV describes the experimental tests and the measurement methods used to analyze the selected materials machinability under the selected cutting parameters and eventually the different lubri-cooling conditions. The used instrumentation is extensively described and the methodologies for the microstructural analysis are deeply explained.

Chapter V highlights the plastic flow modeling and subsequent Finite Element (*FE*) implementation for all the case studies that were investigated. In particular, the metallurgical phenomena are taken into account to reproduce the various microstructural strengthening/softening effects. Moreover, the main characteristics of the boundary conditions setting and the contact behavior modeling are also reported

Chapter VI reports the validation procedures of the various proposed numerical models. Here the predicted values coming from the numerical models are compared with the experimental results giving an estimation of the model prediction errors and consequently a key parameter to evaluate its affordability. Moreover, the numerical models are also exploited in Finite Element Analysis (*FEA*), aiming to investigate the effects of the processes on the material under unexplored deformation conditions.

Finally, the conclusion remarks will summarize the obtained results and highlights the probable future improvements that would worth to be investigated by eventual future works.
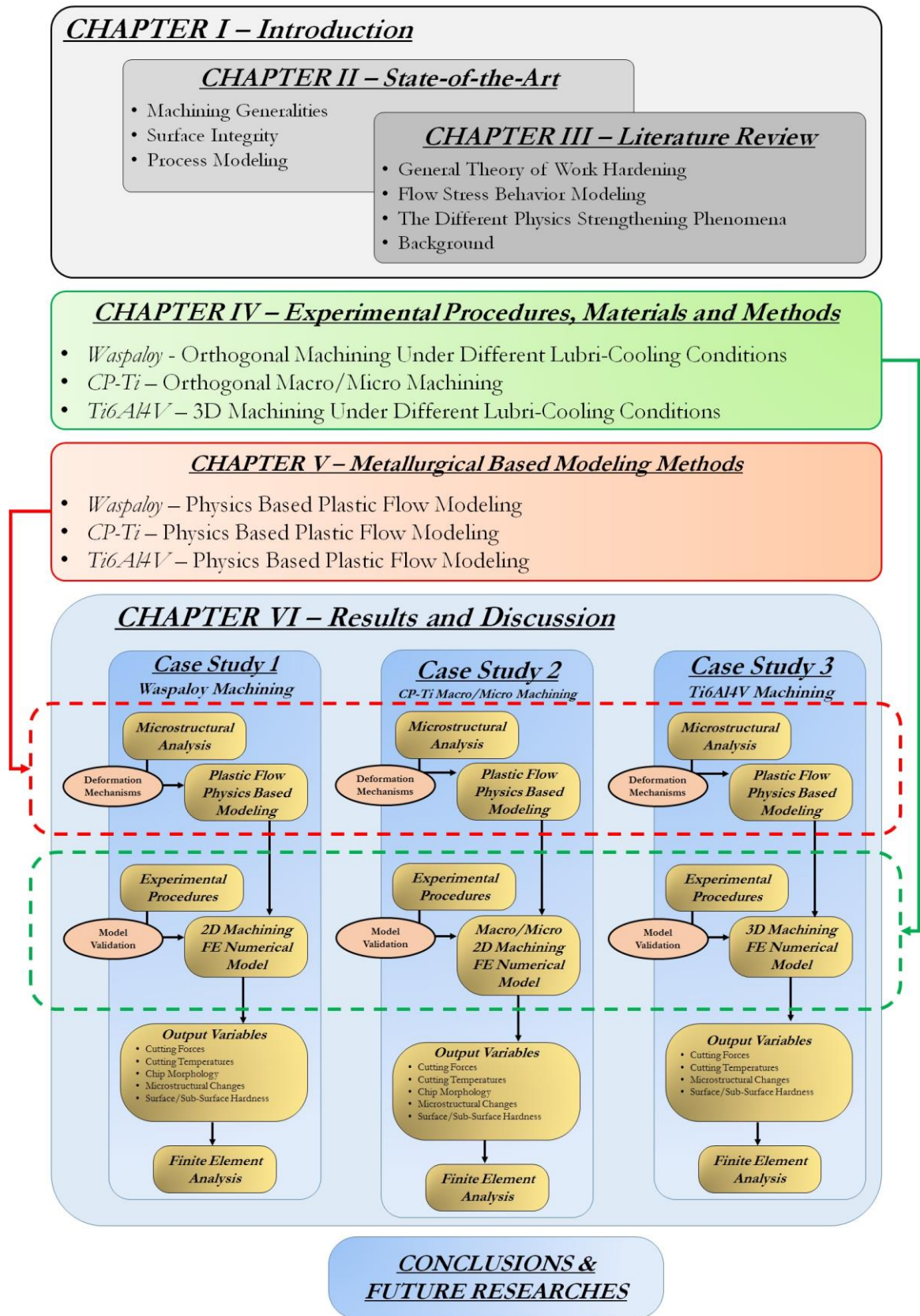
Fig. 9 Flow chart of the *Ph.D.* thesis.

CHAPTER II

In this chapter, a deep analysis of the state-of-the-art of the topics that represent the foundations of the developed researches is reported. More in detail, the chapter pay strong consideration on the general characteristics of the machining processes and their performance indicators, with a particular attention to the surface integrity. Furthermore, this chapter gives emphasis on the Finite Element modeling general techniques.

Machining Processes – Generalities and Modeling

Nowadays, conventional and advanced machining processes continue to occupy a dominant role among all manufacturing operations. During the last decades, a significant enhancement in manufacturing industries developing has been the introduction and development of predictive models for machining operations. Machining modeling often targets the prediction of fundamental variables evolution (such as stresses, strains, strain-rates, temperatures, etc.), on varying the process conditions and parameters. However, in order to be useful to industries, these variables must be related to performance measures: product quality (accuracy, dimensional tolerances, finish, etc.), general surface and subsurface integrity, tool-wear, chip-form/breakability, burr formation, machine stability, etc. (Fig. 10). The adoption of machining models by industries critically depends on the capability of a model to correctly pose these links and to predict machining variables and performances [29].

Moreover, the research activities are showing a strong emphasis on improving the current models and on finding other material constitutive laws in order to predict the machining variables, in order to improve the reliability and the stability of these models, accommodating the market demands. Despite significant prediction models are available as design tool, interest in numerical modeling, e.g. the Finite Element Modeling (*FEM*) and others, is continuing to raise due to advances in computational techniques and capabilities of modern calculators, such as adaptive meshing and automatic remeshing. Spurred by the high industrial demands, several numerical models have been developed for machining of different materials, such as hardened steels, alloy steels, titanium and nickel-based superalloys. Besides, modeling of serrated and segmented chip formation, using damage criteria, has been proposed in many studies [29, 30].
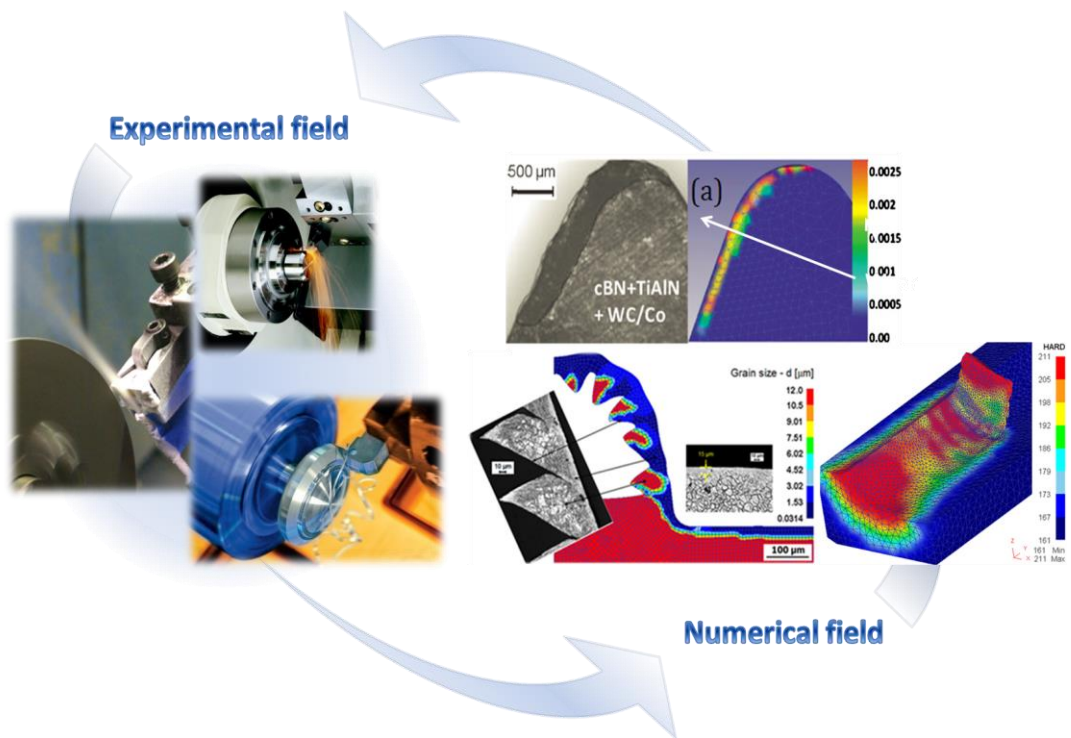
Fig. 10 Finite elements output results used by industries to predict the machining performance experimentally evaluated [29].

In order to properly predict the different variables of industrial and scientific interest, it is necessary to match the predicted value with the empirical value, appreciating the reliability of the model. However, there are some variables, such as stresses in the workpiece or in cutting tool, that cannot be empirically measured during the cutting process, consequently a proper validation of a numerical model needs to be carried out using global measurable variables, such as cutting forces, temperatures and general surface modifications [31, 32].

During cutting processes, the fundamental variables which must be taken into account to set up the best parameters are [31, 32]:

- cutting forces;

- chip-formation and its morphology;

- temperature fields and heat partition;

- stresses, strain and strain-rate;

- material inner structure modifications.

Several efforts of researchers from academia and industries have been made to transform and modify these models, in order to develop and make them able to predict the machining performance measures of particular industrial interest [33], such as:

- tool-life/tool-wear predictions;

- surface integrity;

- phase and microstructure transformation.

Finally, machining is moving through the development of sustainable, or at least lower impacting, lubri-cooling conditions. consequently, additional efforts in the are made in implementation, calibration and validation of affordable *FE* models able to take into account the presence of different cooling techniques [34–36].

2.1. Surface Integrity

The performances of a machined component, its general quality, and the reliability of its manufacturing process can be directly related to surface integrity achieved by the final machining operations. When metal components are machined with the objective of reaching high reliability levels, surface integrity evaluations represent a fundamental pointer to lead the manufacturers to introduce in the market affordable products that can be employed under critical thermo-mechanical loading conditions [37].

The concept of surface integrity (*SI*) was defined by Field & Kahles, and according with the authors "surface integrity means the inherent or enhanced condition of a surface produced in machining or other surface generating operation" [38]. The same authors identified also some key features that represent the reference index to estimate the *SI* conditions of the products, they are evaluated in three different levels and are listed in Table 1 [39]. When a general Severe Plastic Deformation (*SPD*) process is exploited to manufacture a metal, depending on the setting up of the parameters and working conditions, it can be an effective instrument to improve or worsen the workpiece characteristics. In this context, aiming to produce artefacts of higher performances, broad and depth researches have to be conducted to lead the designers in a correct integration of this process into a high performance manufacturing chain [40]. In order to address this concern, the mathematical modeling denotes a necessary support to connect the material characteristics and the process operating conditions. It allows to obtain a better understanding of the physical and chemical inner mechanisms underlying the material processing and to predict the final product

characteristics. In such way, it is possible to optimize the existing systems and processes, improve the product quality, develop new processes, and produce a variety of new materials, while expansive and time consuming experimental campaigns are avoided [41].

Table 1 Different levels of Surface Integrity (*SI*) [39].

Minimum SI Data Set	Standard SI Data Set	Extended SI Data Set
Surface Finish	**Minimum SI Data Set**	**Standard SI Data Set**
Macrostructure (10x or less)	**Fatigue Tests** (Screening)	**Fatigue Tests** (Extended to obtain design data)
• Macrocracks		
• Macrotech Indications		
Microstructure	**Stress Corrosion Tests**	**Additional Mechanical Tests**
• Microcracks		• Tensile
• Plastic Deformations		• Stress Rupture
• Phase Transformations		• Creep
• Intergranular Attack		• Other specific Tests (friction evaluation, sealing properties of surfaces, etc.)
• Pits, Tears, Laps, Protrusions		
• Built up Edge		
• Melted and Redeposited Layers		
• Selective Etching		
Microhardness	**Residual Stress and Distortion**	

In aerospace/aeronautic industries, the materials mostly used are nickel and titanium, and their alloys, instead of steel, because of their better strength at low and high temperatures. They are more resistant to wear and chemical degradation, which make them favorable [42]. However, their poor thermal properties at elevated temperatures make the production of good machined surface challenging [37]. Substantially, final surface status of a machined metal part directly influences its processing and end use. These influences can be categorized as frictional and wear behavior at the tool-workpiece interfaces, effectiveness and control of cooling and lubrication conditions during

processing and in end use, appearance and the role of the surface in subsequent surface finishing operations (cleaning, coating, or surface treating), initiation of surface cracks and residual stresses, that strongly influence fatigue life and corrosion properties, and global heat transfer between two bodies contacting each other [43–45].

At microscale the surface layer on the machined surface is not smooth and may show various different features that can represent a performance improvement or cause premature failure, such as micro cracks, craters, folds, laps, seams, inclusions, plastic deformation, residual stresses, oxide layer, and metallurgical transformations. In most applications, having the smoothest possible surface is desired, especially when the fatigue life of a machined part is important. However, in some cases, having a rougher surface can be preferred. These cases generally occur in the biomedical field [46, 47]. More in detail, a sufficient severe machining process locally affect various surface integrity attributes on the processed component. These can be grouped as: topography characteristics (textures, surface roughness), and mechanical properties affected (residual stresses, hardness, metallurgical modifications) [37]. Furthermore, a fundamental scope in machining models developing is the prediction of surface and sub-surface integrity due to the fact that it relates directly to the quality, performance and life of machined components.

2.2. General Modeling and Simulation Methodologies

The fundamental tenet of the scientific research is to understand and control some systems that are substantially portion of the universe, or able to represent them with sufficient approximation. Unfortunately, some of these systems are not sufficiently intelligible to be comprehended without a previous abstraction, due to their intrinsic counterintuitiveness or complexity. In operative terms, scientific abstraction consists in substituting the investigated parts of the universe by a representative model able to represent them with sufficient accuracy. This operation of replacing real systems with representative models, can be considered as the most general and original principle of modeling, namely formulating an imitation of a real system by using similar, but simpler (or in any case with a lower degree of complexity), structures [48]. Moreover, not all scientific questions are directly amenable to experiment. There is a hierarchy of questions whose levels are determined by the generality of the required answers. An experimenter might formulate and answer that question precisely, and yet have only a vague, intuitive appreciation of its "higher", more general and abstract implications. Therefore, scientists lay down as a general rule that "high" order, very abstract and universal questions, are not directly amenable to an experimental test, needing to

analyze them in depth and translating them into more specific terms, that are directly translatable into experimental procedures. Thus, there are two qualitatively different operations involved in the process of formulating the examination of a general statement, or in the converse process of formulating a new theory from experimental data. One of these operations consists in moving up or down the scale of abstraction; the other requires the conversion of abstraction into experiments, or vice versa [49]. In the light of the above, aiming to obtain a suitable picture of the examined system, a sort of "phenomenological portrait" has to be taken from it. Afterwards, this picture has to be translated into a mathematical model, using an approach that is referred as the "generalized state variable concept". The convenience of the exerting of a model based on mathematic reside in the enormous parametrizing possibilities and manipulability that mathematical structures can provide. However, a proper structured mathematical modeling procedure, requires the appropriate selection of independent variables, state variables, equations, parameters and initial values [50].

The independent variables can, by definition, be freely chosen and they typically quantify the spacetime of the system. In contrast, the state (or dependent) variables are function of the independent ones. The latter can identify the specific state of an investigated system at any instant, irrespective of their history. More in detail, they cover the static of the system at a certain point of the spacetime, while its kinetics (so, its evolution) is described by the mathematical equations. The selection of adequate state variables, state equations and evolution equations can be made heuristically, on the basis of ab-initio concepts, or on the basis of phenomenological observations [51].

2.2.1 Material Modeling, Scale Considerations

Modern materials science is based on the fundamental experience that the properties of whatever material cannot be directly determined from their general chemical composition, but their inner crystalline structures and their topography strongly influence their behavior, mainly for what concerns the mechanical and electromagnetic properties of the investigated material. Aiming to give a possible definition of the metal microstructure, it can be "the totality of all the thermo-dynamic non-equilibrium lattice defects on a space scales that ranges from Angstroms to meters. Its temporal evolution ranges from picoseconds to years". One of the major objective of material science is to quantitatively relate macroscopic samples behavior to their microstructure [48, 52]. Following the proposed length scale hierarchy, it is possible to identify different levels of

microstructure modeling, that can be roughly grouped on varying the length and time scales, as shown in Fig. 11.
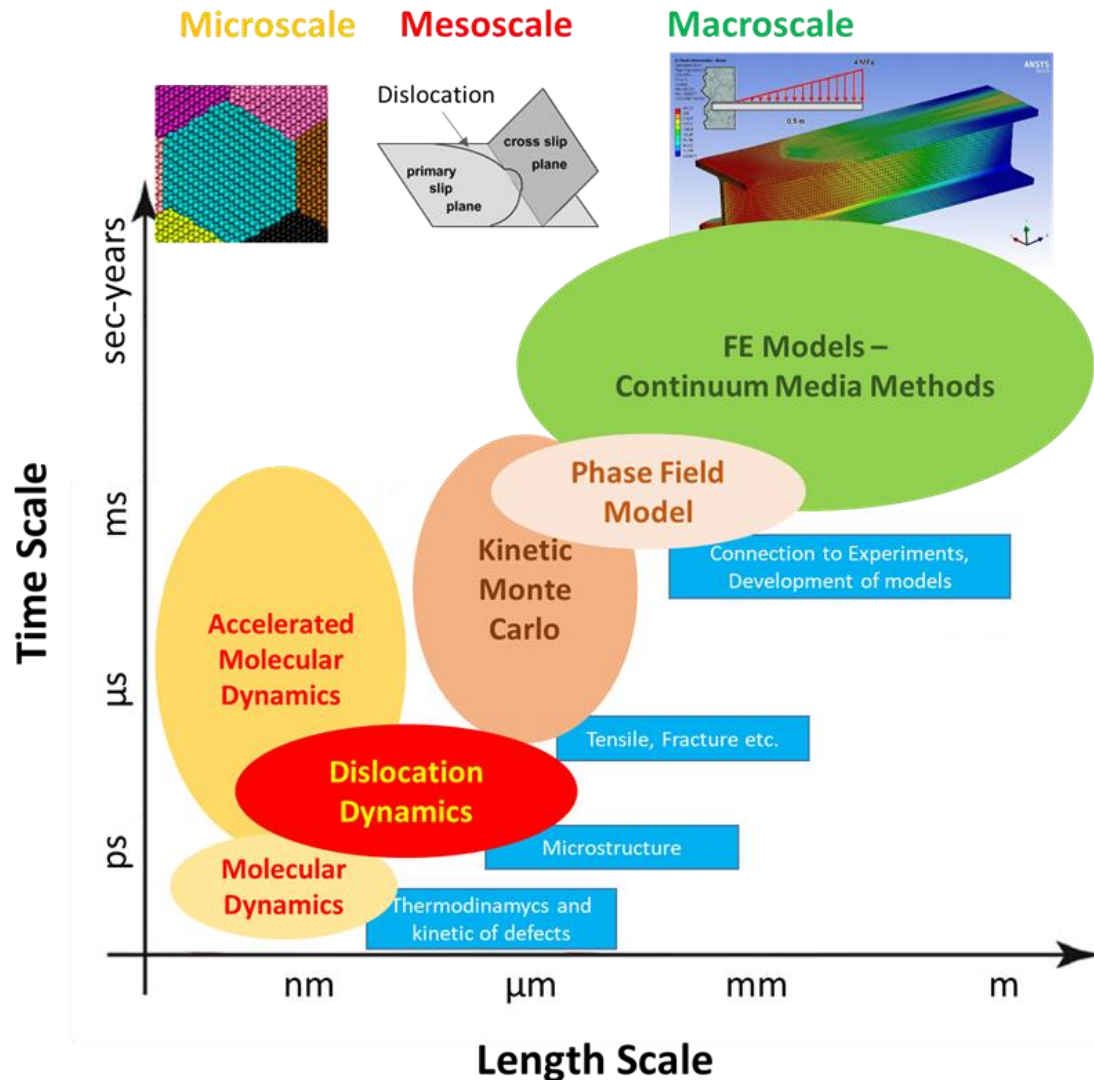
Fig. 11 Rough representation of the principal characteristic modeling strategies depending on the length scale and time scale.

Due to the large spatial and temporal spread of microstructural ingredients that can be considered for a specific analysis, and the complexity of the phenomena that can occur among them, a quantitative physical prediction of the material microstructural evolution strongly requires the employment of modeling and simulation. Furthermore, for practical engineering researches, the predictive capabilities of a well-posed numerical procedure represent an extremely useful tool to reduce the large number of experiments that is typically required in the design and optimization of new materials and industrial processes [48, 53].

Over the last 45 years or so, computational solid mechanics has become an integral part of theoretical materials science. Computational studies concerning crystal plasticity, material instabilities, and fracture mechanisms provided essential contributions to the current understanding of the mechanical behavior of materials when subjected to huge cyclic thermo-mechanical loads and/or large strain deformation fields [54].

Despite its broad functionality, conventional continuum mechanics formulations show a subsistent lack of effectiveness reducing the material length scale. For example, the prediction of a material fracture toughness requires a smaller length scale, if only from dimensional considerations [55, 56]. In order to face these weaknesses, physically based continuum models of fracture processes that contain a length scale were developed. Moreover, incorporation of a length scale is also needed to predict important features concerning the material behavior when depends on local microstructural effects, such as shear bandwidths or in general metallurgical changes. This mesoscale size range is of importance for several reasons. Microprocesses work in this size range and nowadays are showing a strong increasing in technological significance. Furthermore, also processes that control the mechanical integrity of microelectronic devices, both during processing and in service, take place on this size scale. Finally, this is the size scale for key deformation and fracture processes in structural metals [57, 58].

Large varieties of theoretical frameworks are emerging to define inelastic and plastic deformation material behavior at the mesoscale, and these are posing hard numerical challenges. In detail, three main frameworks are representative, each involving a length scale and each one demonstrates different characteristics: discrete dislocation plasticity, nonlocal plasticity and the coupling of matter diffusion and deformation. In discrete dislocation plasticity, the dislocations are treated as line singularities in an elastic solid. Using this approach, many body interaction problems involving the discrete dislocations needs to be solved together with a more or less conventional solid mechanics boundary value problem. Plastic flow processes on the mesoscale can also be studied using a nonlocal plastic constitutive relation, where a material length scale is incorporated directly into the constitutive description and the structure of the boundary depends on how that is done. Finally, diffusion is a microstructural mechanism of deformation occurring at the temperatures encountered in the manufacture of semi-conductor devices. In particular, the surface diffusion driven deformation of thin films lead to insulated formations, which gives a possible means of producing quantum dots that can be used as inner structure of this simulation approach [56]. The close interaction between mechanics and materials science issues in the mesoscale regime is worth noting. Mesoscale mechanics is being used to elucidate basic mechanisms of material

behavior that are difficult, if not impossible, to be analyzed via direct atomistic analysis or conventional, scale independent continuum analysis. At the same time, materials science problems are driving the development of new mesoscale continuum formulations that, in turn, demand the development of new computational strategies [56].

Considering general machining processes as explicative reference cases, here thermo-mechanical loads and microstructure evolution are both involved when the workpiece is processed. Indeed, the loading conditions became more intense during the chip formation. This has substantial consequences on the metallurgical modifications at different zones in the workpiece (generated surface, chip and tooltip). In this context, machining simulations strongly depend on the plastic flow stress behavior, that plays a fundamental role to correctly reproduce the deformed material evolution during the manufacturing process, relating the physics variables involved during the metal deformation (strain, strain rate, temperature, microstructure, etc.) with the resulting stress and microstructural variables occurring at different deformation fields [59–61].

2.3. Material Constitutive Modeling

Based on what explained in the previous chapter, the advanced microstructural based simulations have to satisfy three fundamental requirements. First, they should enable the operator to use, or even derive, advanced path-independent microstructure-material properties relations with quantitative validity. Second, they should provide insight into the underlying thermo-dynamic and path-dependent physical principles that govern the nature of microstructure evolution. Third, the model should allow to replace and complement experimentation by simulation, at least in certain ranges and conditions [48].

In the microstructure based modeling, among the state variables, it is relievable a further distinction, namely that between implicit and explicit state variables. The explicit state variables describe the local material microstructural features, while the implicit ones represent the mesoscopic or macroscopic averages. In particular, the latter type of state variables is of fundamental relief in the resuming of microstructural properties in Finite Element (*FE*) simulations. This simulation technique, is minded to provide approximate solutions to coupled set of partial differential equations subject to appropriate boundary and initial value conditions. *FE* first applications in material science was solely oriented to solve elastic and simple plastic problems at the macroscopic level using averaged constitutive laws and the conditions for equilibrium and

compatibility. However, through the introduction of improved constitutive laws, *FE* methods are capable of simulate materials heterogeneity also at the mesoscopic level [48, 53].

2.3.1 Constitutive Models, Material Elastic Behavior

The elastic behavior of a general material that is subjected to a certain deformation field show a relatively reduced influence by its inner microstructure status. Nevertheless, in some specific conditions, it have to be considered to properly represent its mechanical behavior, such as the self-blocking of lattice dislocations on different slip systems [48, 62]. However, in most cases mesoscale and macroscale models exploit methods that level out these fine details of the microstructure, substituting it by an appropriate constitutive description and including certain assumption of material homogeneity. The principal model used to relate the strain loads that affect a material with its inner stress status is the well-known Hooke's law. This law means that for small external or internal forces the time independent reversible response of the material, which is quantified by the displacement field, can be linearly related to that force. More in detail, the strains, that are expressed by the symmetric part of the displacement gradient tensor, then describe a linear elastic shape change which is proportional to the stress [63, 64]. The Hooke's law is reported in tensor form in Eq. 1:

$$\sigma_{ij} = C_{ijkl}\, \varepsilon_{kl} \tag{1}$$

Where σ_{ij} is the stress tensor, representing the inner pressure status induced by the external or body forces applied on the investigated material. ε_{kl} is the strain tensor, that is representative of the material induced deformation status, while C_{ijkl} is the stiffness matrix, that proportionally relates the deformation status of the material to its inner stress status [48, 63].

2.3.2 Constitutive Models, Material Yielding

Once the deformation exceeds a certain limit (yielding limit) the deformations became irreversible. In this field, the material behavior is strongly microstructure dependent, and consequently it becomes extremely difficult to be modeled. Thus, complex methods have to be implemented to properly simulate the modifications that occur on the material, both on macroscale and mesoscale. The phenomenological methodologies that are exerted to depict such constitutional behavior at the macroscale are often grouped into rate-independent or yield surface approaches

and rate-dependent or viscoplastic approaches. The rate independent description is framed in stresses space, or Haigh–Westergaard (*HW*) space, and also in strain spaces. This is sometimes referred to as the elastic-plastic description. The construction of a yield surface is based on the assumption that irreversible deformation starts when a critical shear stress (σ_{crit}) is reached. The tensor expression that defines this critical stress in the *HW* space as a function of the applied stress tensor describes the yield surface. It is referred to as a yield criterion and is formulated as (Eq. 2):

$$f(\sigma) = \sigma_{crit} \tag{2}$$

In Fig. 12 are reported the two classical yield criteria in the principal *HW* stress space, namely the Tresca and von Mises criteria.

Yield surfaces of the kind presented in Fig. 12 have some important features. Stress states outside the yield surface cannot occur. At the stress state below the yield surface the material can be only elastically deformed. Any imposed stress status that resides on the yielding surface induces plastic deformation. Meaning that all the admissible stress conditions for plastic flow must stand on the yield surface. The latter surface cannot be modified in terms of shape, though only expand in stress space due to material work-hardening phenomenon.
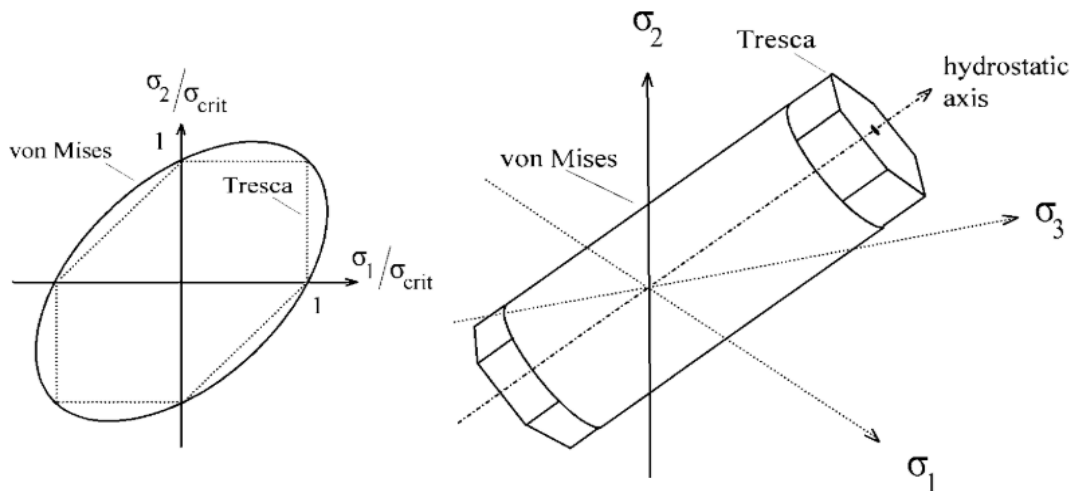
Fig. 12 The two classical yielding criteria in the principal Haigh–Westergaard stress space: Tresca and Von Mises yield criteria [48].

Fig. 13 shows two typical cases of hardening as used frequently in the conventional isotropic rate independent approach. In Fig. 13a is reported the isotropic work hardening, in these conditions the yield surface is only allowed to expand isotropically in stress space. Likewise, in Fig. 13b is reported the kinematic hardening, this effect forces the yield to shift without changing its original shape.
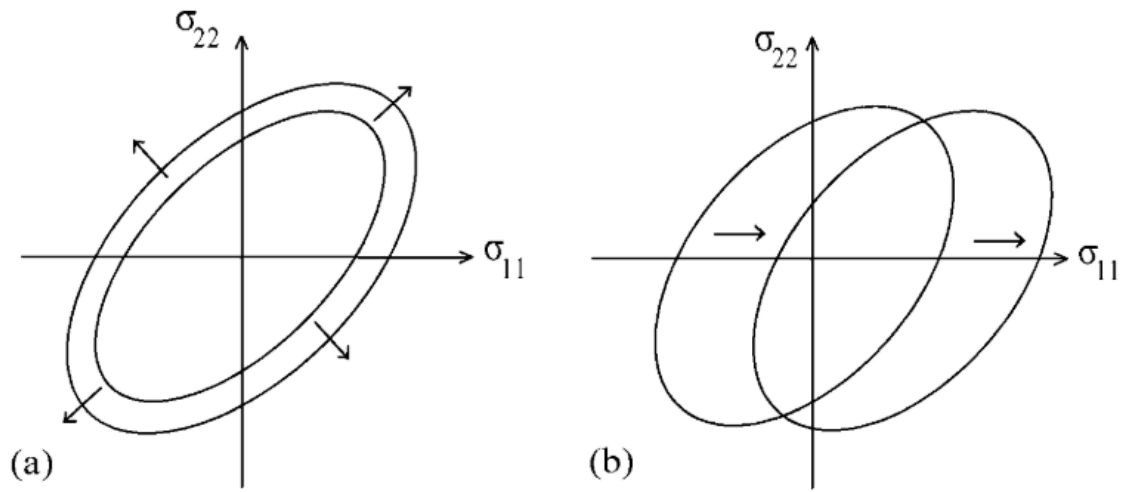
Fig. 13 Two examples of material hardening in the rate-independent constitutive approach. (a) Isotropic work hardening and (b) Kinematic hardening [48].

CHAPTER III

In this chapter, hefty attention is given to the specific flow stress modeling techniques and their importance in the evaluation of quality and performances of the final product, exploiting surface integrity analysis. Moreover, a general background on the mathematical theories founding the physics based flow stress modeling is reported, focusing on the main issues that occur in the large plastic strain deformation modeling procedures, and in particular for what concerns the general machining modeling methodologies.

General Theory of Work Hardening

Considering a general Face Centered Cubic (*FCC*) lattice material, its proper flow curve at relatively low temperatures (from 30% to 40% of melting point), can be divided into four different stages, or behaviors, as indicated in Fig. 14a. These various stages of work hardening are most clearly distinguished on a diagram that represent the θ vs τ relation, where $\theta = \frac{\delta\tau}{\delta\gamma}$, as visible in Fig. 14b. This kind of plot is commonly referred to as Kocks-Mecking diagram [65].

Stage I is identified as easy glide region and typically show a low degree of hardening. Indeed, the coefficient of work hardening shows a rather small value (θ/G, where G is the material shear modulus). It is strongly dependent on the orientation of the crystal and tends to not occur when the deformation takes place by multiple slip from the beginning.

Stage II is characterized by the steepest rate of work hardening $\theta_{II} \approx G/200$ for multiple slip) which has a linear behavior and it is only weakly sensitive to temperature and strain rate (except for the temperature dependence of the shear modulus G).

Stage III begins when the flow curve deviates from linearity with an increasing slope. This stress, is strongly strain rate and temperature dependent, a dependence associated with athermally activated process where the rate controlling reaction is generally believed to be cross-slip.

A further characteristic that differentiates the last two stages is that *Stage II* is material insensitive, while *Stage III* strongly depends on the material. In particular, it is directly related to the material proper Stacking Fault Energy (*SFE*).

Stage IV is most easily distinguished from the θ-τ plot (Fig. 14b). In the work hardening curve this stage often appears with a linear hardening rate (although deviation from linearity is frequently observed) with $\theta_{IV} \approx 2*10^{-4}$. Another characteristic aspect associated with the temperature

dependence of *Stage IV* and indicated in Fig. 14b is that θ_{IV} is linearly dependent on τ_{IV}, typically having a value of 0.1 [65, 66]. Following the comportment of this flow curve characterization, Zehetbauer and Seumer [67] introduced a *Stage V* before reaching the saturation stress (τ_s).

The curves in Fig. 14 showed plastic strain only, in the abscissa. The initial elastic region is not included. However, if considered, it would not appear in these plots, because it is so steep in comparison to all measured strain-hardening rates [65].
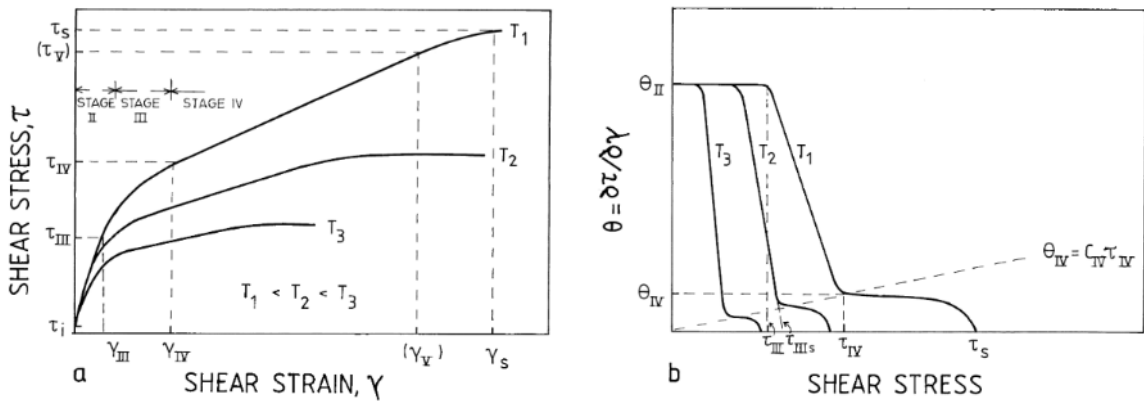
Fig. 14 Schematic stress-strain curves (a) and strain hardening (θ) vs flow shear stress (τ) curves for *FCC* metals (b) [65].

3.1. Flow Stress Behavior Modeling

The plastic materials flow behavior during general hot deformation processes it is well-known to be very complex to be investigated and, in general, numerically reproduced. The different hardening and softening mechanisms that concur together in the material plastic strain evolution are both significantly affected by the processing temperature and strain rate. The understanding of this behavior is of great importance for designers and researchers that work with production engineering sub-sets that are related to the plastic deformation processes of metals, because of its effective role in the simulation of the metal flow behavior as well as the occurrence of metallurgical transformation, and the constitutive relation is often used to describe the plastic flow properties of the metals and alloys. In general, these latter are expressed in a form that can be used in computer code to model the deformation response of a general workpiece under the imposed loading conditions [68].

3.1.1 Empirical Flow Stress Modeling

Empirical constitutive models provide global description of the yield/flow stress that is fundamentally based on empirical observations of the material thermo-viscoplastic behavior. They consist of certain mathematical functions that tend to represent the material behavior when subjected to thermo-mechanical loads, lacking the physical inner phenomena occurring inside the deformed material. While the process of phenomenologically formulating models can be regarded as an essential step among the building operations of a model, it must be decided which state variables are of strong and which ones of slight influence on the global system behavior. In this context, empirical models do not distinguish between important and unimportant contributions. In these models, yield stress is usually an explicit function of state variables, such as accumulated plastic strain, strain rate and temperature, implying that empirical models are not load history dependent. Moreover, the problem with the accumulated plastic strain is that it is a non-measurable virtual variable. Furthermore, empirical constitutive models are normally characterized by reduced number of material constants and easiness of calibration, that makes them more efficient and easier to be implemented. However, due to their empirical characteristics, they usually cover a limited range of applicability, show reduced flexibility, and offer low accuracy. Empirical (or phenomenological) models are also named engineering models as they are more common in engineering applications than the physics-based material models. A number of common empirical constitutive models of metals thermo-visco-plasticity are usually incorporated in commercial *FE* software [69–71]. A phenomenological model that is worth to be mentioned and plays a determinant role in *FE* analysis of large and high strain rate deformation strain fields is the Johnson-Cook (*JC*) model. Due to its simplicity of implementation, it is also the most widely used in machining simulations, that are the object of interest of this research work, because it is defined through simple interpolation of experimental data and can properly simulate the flow stress in a broad range of strain rate and temperature conditions with sufficient approximation. This model provides a description of the relationship between true stress and true strain at various strain-rate and temperature, during different deformation mechanisms [31, 72]. *JC* based numerical models can be also coupled with microstructural dependent semi-empirical models, making possible to get important information about the surface modifications. Unfortunately, they frequently need to be re-calibrated considering the possible dissimilar working conditions and different initial microstructural status of the processed material, and the obtained numerical constants have not physical meanings [32, 48, 73].

3.1.2 Microstructure Based Flow Stress Modeling

Microstructural or physics-based constitutive models consider the microstructure, and consequently the physical aspects of the material behavior. In these models, the knowledge about the underlying microstructural effects, including the dynamic of dislocations, is exploited to formulate the Thermo-Micro-Mechanical (or thermo-mechanical-microstructural) constitutive equations. Moreover, since these material models can reproduce the occurring microstructural phenomena that are promoted by the material mechanical response to plastic deformation, they can be applied under large ranges of deformation parameters (strain rate and temperature) and loading/deformation modes (tension, compression, creep, and relaxation). For what concerns the industrial metal forming processes, materials can experience a wide variety of possible thermo-mechanical loads. Furthermore, history-dependent microstructural based constitutive models are much more suitable and robust for comprehensive simulations of complex industrial metal deformation processes. Hereupon, physics based models may follow different approaches to describe the metallurgical evolution/kinetics in polycrystalline metallic materials when subjected to large strain/strain rate deformation fields, as highlighted by Motaman & Prahl [74]. These authors distinguish two different approaches, depending on the possible preliminary considerations about the manner in which the dislocations are considered:

- Discrete Dislocation Dynamics (*DDD*) where slip/glide/motion and interaction of the single dislocations are considered, and, in such way, the rheological response of the material is a result of direct simulation of a broad collection of dislocations in a very small Representative Volume Element (*RVE*). These algorithms are sorely time consuming due to their typical high computational load, and result to be extremely difficult to be implemented in commercial *FE* software for industrial application.

- Continuum Dislocation Dynamics (*CDD*) that indirectly describe the microstructure, and consequently the micro scale phenomena that affect the material plastic behavior are represented, as averaged quantities, at the macroscale level. This methodology is the main subject of the presented research work, using the notion of dislocation density, which is measurable to some extent by electron microscopy and X-ray techniques. Due to their physical nature, constitutive models based on different types of dislocation densities have the potential of predicting many other important processes and treatments that can act on the material, such as creep, relaxation, dynamic strain aging, static aging, and bake hardening [74].

3.2. The Different Physics Strengthening Phenomena

Using the indirect *CDD* approach, dislocation density-dependent rheological models represent a connection between the micro-level phenomena and macro-level continuum mechanical quantities. Furthermore, simulations performed using these constitutive models are much less demanding in terms of computational cost, almost in the same range of common empirical constitutive models. Moreover, they are less difficult to be implemented in a commercial software compared to their counterpart based on *DDD*. Hence, they can be easily included or formulated using customized codes in standard *FE* software. In the proposed research work, the models are considered to be into the isotropic case, consequently Bauschinger, asymmetrical and anisotropic effects are not considered in the presented *TMM* constitutive models. However, the possibility of applying the proposed plastic flow models in a general crystal plasticity modeling structure, can allow to account for anisotropic effects caused by nonuniform dislocation density evolution on each slip system.

3.2.1 Dislocation Strengthening

One of the most surprising observations in the dislocation theory of plasticity is the linear relation between plastic shear stress (τ) and square root of the dislocation density (ϱ). It holds, with little regard to the arrangement of dislocations, with such generality for all those cases where the flow stress is solely controlled by dislocations self-interaction, as in pure *FCC* materials deformation [75, 76]. More in detail, when metals are deformed at room's temperature, it is possible to relief a variation in the average dimension of subgrains structures (cells). On the other hand, in common polycrystals deformation that are subjected to multiplane slip, it is possible to identify regions with higher dislocation density that are interconnected in diffused cell walls, and regions less dense of dislocation that are the out-and-out cells (Fig. 15) [66].
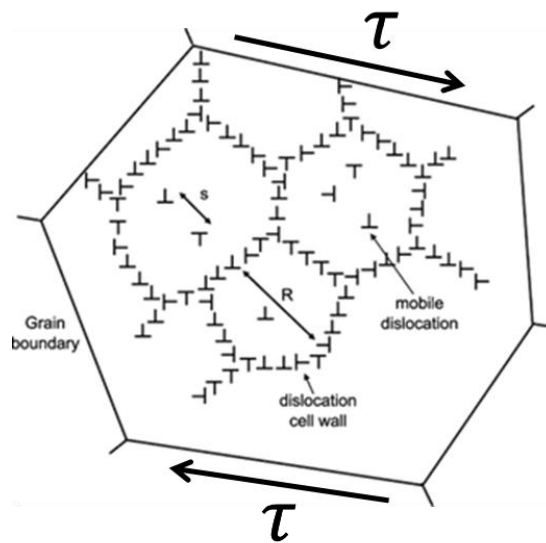
Fig. 15 Dislocation distribution in a crystalline grain subjected to a shear stress status, dislocations are distributed into the cells, that are delimited by high dislocation density regions (cell walls).

Cell sizes are strictly related to dislocation spacing, so the cell size evolution during the deformation process can be also involved in a more precise description of the material hardening due to dislocation accumulation. As observed in highly deformed pure metals, the cell structure gives the impression of being a two-parameter disposal. Nevertheless, this is deceptive, because the cell diameter (for reasonably equiaxed cells) is known not to be an independent parameter, but be inversely proportional to the square root of the average dislocation density and thus to the 'first' state parameter related to the plastic flow stress. At this point, it has become the fashion in the dedicated scientific literature to describe the dislocation density evolution of a deformed material explicating the dependence from the cell structure. In particular, the dislocation density of the cell interiors and the cell walls are treated as separate phases that both contribute to the total dislocation density of the material. The rule of mixture is used to consider both phases contributions, weighting them considering their respective volume fraction [77–79].

In essence, it is doubtful whether the description of the flow stress as function of the cells microstructure is more appropriate than the simple proportionality with the dislocation spacing. However, although this modeling approach shows a better description of the involved physics/microstructural phenomena, its application frequently leads to useless complication of the mathematics. Therefore, a modeling approach based on the global evolution of the average

dislocation density without specifying their inner nature, can also simulate the material flow behavior with excellent approximation [80–82].

3.2.2 Thermally Activated Strengthening (Peierls Stress)

Referring only to the motion of dislocations through the material lattice, and consequently ignoring the possible obstacles that can be present, it is possible to notice their ability to move under the action of relatively small forces. The mobility of dislocations crucially depends on the different possible pinning mechanisms. Despite the main contribution in pinning effects is due to imperfections of the crystal structure (impurities, precipitates, etc.), it is worth to notice that some pinning phenomena are relievable also in perfect crystal materials. These are due to the intrinsic barriers for dislocation motion that are caused by the discreteness of their crystal lattices (also called Peierls-Nabarro barriers), as visible in Fig. 16. Their magnitude may be characterized by stress of the pinning, or Peierls stress, giving raise to the resistance forces exerted by the crystal lattice, per unit length of the dislocation line. Since dislocation mobility is affected by the Peierls-Nabarro barriers, the mechanical properties of materials depend on such fundamental characteristics as the type of crystal structure and character of chemical bonds between the atoms [83–85]. Substantially, the Peierls-Nabarro barriers impede the dislocation motion, and consequently the material flow, atom-by-atom globally acting as a friction force, and impeding the free dislocation motion into the lattice [86, 87].
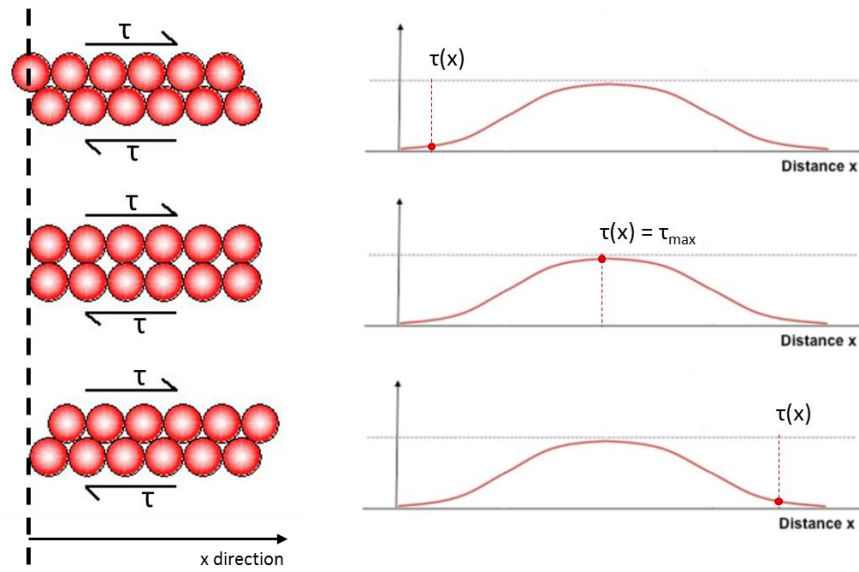
Fig. 16 dislocation motion and Peierls-Nabarro force per unit length of the dislocation line
(reported as an acting shear stress τ(x)) evolution during the dislocation motion.

3.2.3 Dislocation Drag Strengthening

In quantum physics, a phonon is a collective excitation in a periodic, elastic arrangement of atoms or molecules in condensed matter, specifically in solids and some liquids. It is often considered as a quasiparticle, it is an excited state in the quantum mechanical quantization of the modes of vibrations of elastic structures of interacting particles [88]. The anharmonic interaction and scattering of the phonons by a moving dislocation, the so-called phonon wind, imparts a certain drag resistance on the dislocations motion. This quantum phenomenon influences the material response to the high speed mechanical loads, significantly increasing the material strain rate sensitivity, and contributing in a higher short-range strengthening effect. This phenomenon is usually negligible at low deformation speeds. However, it can represent a substantial increment in terms of materials inner strengthening when the strain rate reaches order of magnitude results in the order of 10^3 s^{-1} or higher [87].
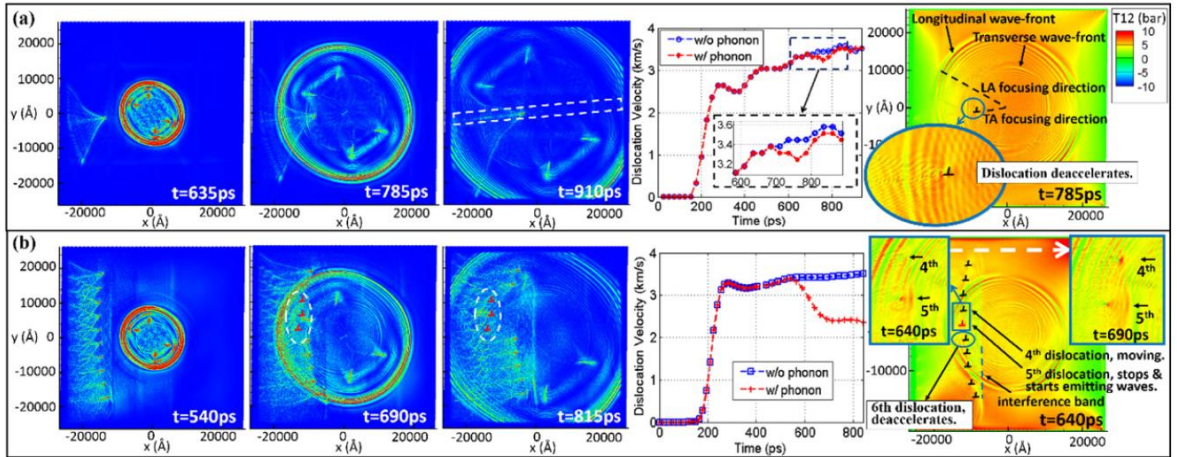
Fig. 17 Normalized kinetic energy distributions show the transient processes of the propagation of (a) a single dislocation and (b) multiple dislocations and their interactions with a coherent phonon [89].

3.2.4 Grain Boundary Strengthening

The crystalline grain boundaries are another important cause of the strengthening of the metal materials. This is the phenomenon of grain boundary strengthening, also known as *Hall-Petch* (*H-P*) effect, and is due to the piling up phenomena that occur at the grain boundaries, leading to the activation of other slip systems in the surrounding grains. This particular strengthening effect is more pronounced as much as the probability of encountering a grain boundary is higher. Consequently, having a reduced grain size, and therefore a higher density of grain boundaries, results in a more strengthened behavior of the investigated material [87]. In grain size ranges that start from hundreds of microns to dozens of nanometers, hardness increases as grain size decreases, according to the *H-P* strengthening model. On the other hand, nanocrystalline grains materials may be considered as being microstructurally heterogeneous, comprising building blocks (i.e., crystallites) and regions between adjacent building blocks. The presence of large amounts of grain boundaries in nanostructured materials is crucial for many of their properties. Thus, it is reasonable to expect that a critical grain size at which the *H-P* relation remains valid and beyond it, the inverse *H-P* effect occurs and the strengthening effects reverts its behavior respect to the grain size, tending to promote the dislocation motion and consequently reducing the grain strengthening phenomenon. Nano-effect or size effect can be considered as a special case of the *H-P* effect, it occurs when the mean grain diameter tends to nanometers [90]. Moreover, it is worth to point out that under certain thermo-mechanical loading conditions the grain structures can evolve, influencing the material behavior.

50

As relieved by Sargent et al [91], different static and dynamic grain size modification phenomena occur when a general material is largely deformed at elevated temperatures. Static Recrystallization (*SRX*) takes place when strain hardened metallic materials are processed at around the 50% of their melting point (in Kelvin). This effect depends on specific material factors such as the type of lattice, concentration of alloying elements, and size distribution of second phases [92, 93]. On the contrary, the Dynamic Recrystallization (*DRX*) takes place during the high strain rate deformation of the processed material, as long as the temperature is above about the half of its melting point [94]. More in general, the new grains appear when certain nucleation conditions are achieved, tending to replace, or in any case modifying, the initial microstructure. As in the case of *SRX*, there is a gradual transformation of the subgrains nucleated mainly in the closeness of the grain boundaries into nuclei [92]. It has been recognized that the dynamic mechanism differs considerably from that operating during static recrystallization. The latter leads to the evolution of a uniform and dislocation-free grain structure after full annealing, accommodating the protruding of crimped grain boundaries, Fig. 18 [95].
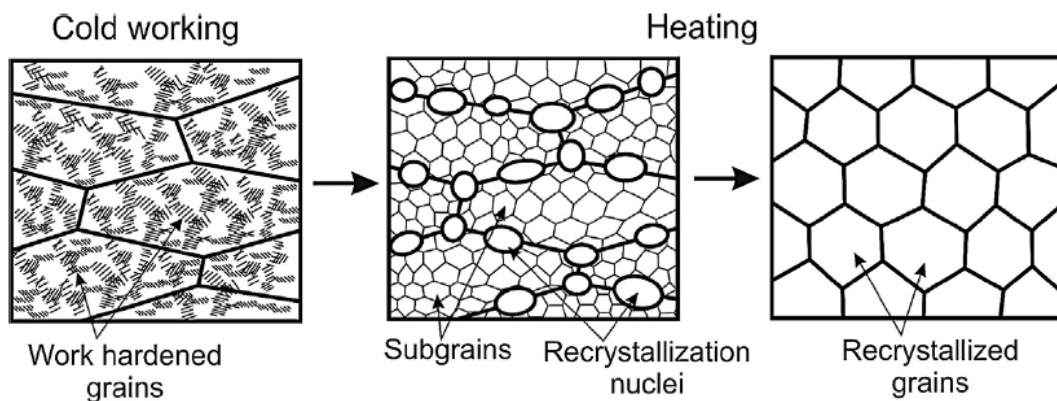
Fig. 18 Schematic representation of the discontinuous static recrystallization (*SRX*) taking place during the annealing of strain [95].

In contrast, the dislocation density is controlled by two competing processes during the material high temperature and high strain rate deformation processing. Continuous generation of dislocations due to plastic flow, that leads to material work hardening, and dislocation annihilation to Dynamic Recovery (*DRV*), leading to a softening response of the deformed material. *DRX* occurs when the dislocation density reaches a critical value. For materials with a relatively high stacking fault energy, dislocation movement is relatively easy, therefore *DRV* can grasp a dynamic equilibrium with work hardening at a relatively low dislocation density status, and the dislocation density cannot reach the critical value for *DRX* [96]. In contrast, in materials that are more prone

to *DRX*, the strain hardening produced by deformation is counteracted by this mechanism. It gradually reduces the work hardening rate until a flow stress maximum is reached after which there is strain softening. In these materials, the dislocation density increases to a high level and eventually some of the local differences in density reach a high enough level to permit the nucleation of new grains (Fig. 19) [95].
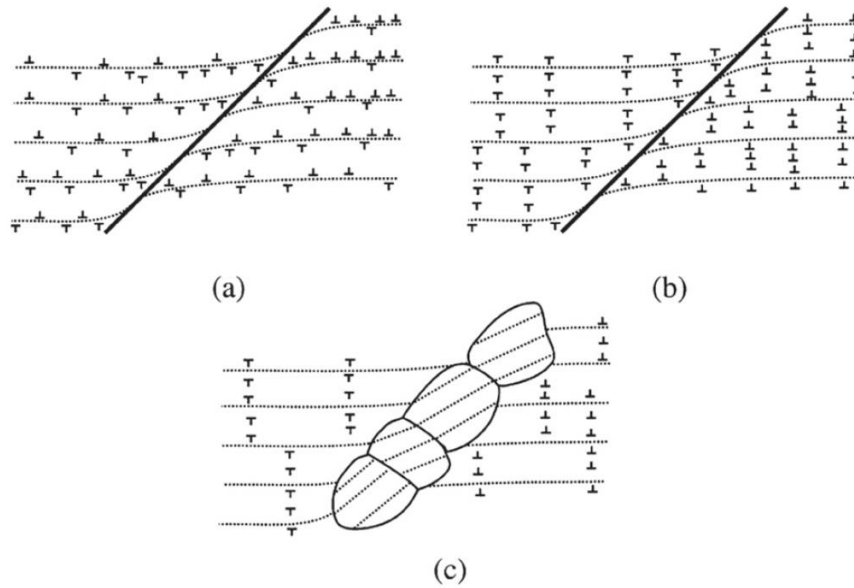
Fig. 19 Schematic diagram showing the proposed mechanism of *DRX* in magnesium, by progressive lattice rotation and *DRV* at grain boundaries [93].

3.2.5 Crystal Twinning Strengthening

When a metal or alloy is plastically deformed, its shear strain can result in deformation twinning, especially at low temperatures and low strain rates. Other deformation mechanisms such as dislocation slip, recrystallization phenomena, and diffusion, become significant at relatively high temperatures, especially when the grain sizes are large [97]. Deformation twinning is a common and important phenomenon in metals and alloys. Conventionally, deformation twins in *FCC* metals are believed to be formed by the glide of partial dislocations with the same Burgers vector on successive planes. This collectively produces a macroscopic strain to accommodate the imposed thermomechanical loads [98]. Bulging of parts of a serrated grain boundary accompanied with the evolution of dislocation sub-boundaries or twinning, leads to the formation of a new grains (Fig. 20) [99].
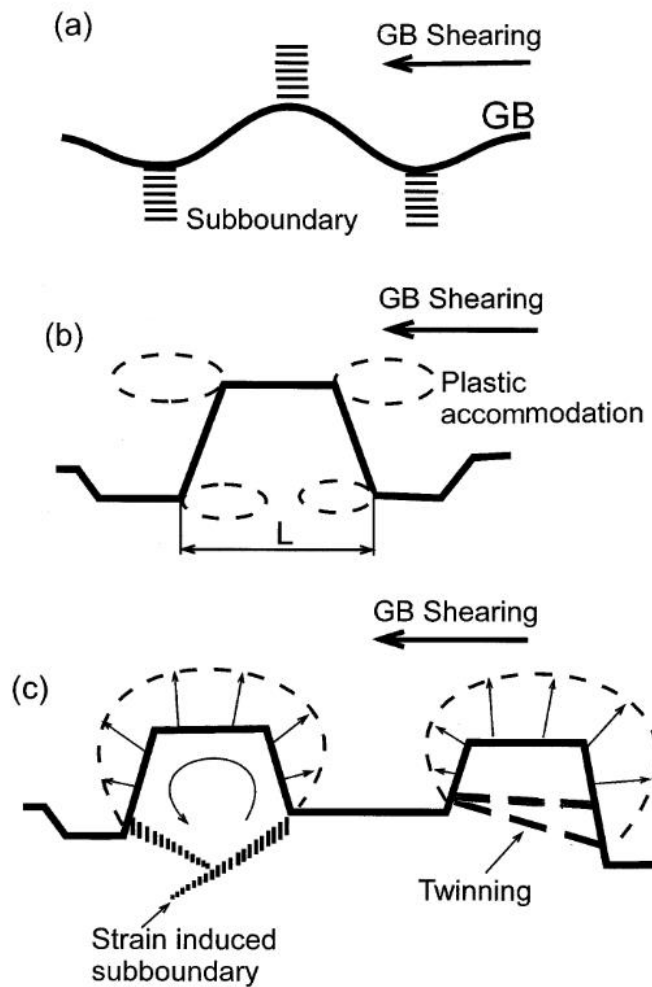
Fig. 20 Schematic representation of the nucleation of *DRX* or twinned grains. Boundary corrugation accompanied by the evolution of sub-boundaries (a). Partial grain boundary sliding/shearing, leading to the development of inhomogeneous local strains (b). Bulging of parts of a serrated grain boundary accompanied with the evolution of dislocation sub-boundaries or twinning (c) [99].

3.2.6 Solid Solution Strengthening

Impurity atoms in solid solution increase the strength of crystalline materials. This is due to the mechanical interaction that take place between moving dislocations and solute atoms. As reported in previous paragraph, the dislocation stress field is a long-range acting one, so solute atoms, located both on the slip plane and above/below it, interact with dislocations. Solute atoms are generally considered "weak" hardeners, and this is true above all concerning substitutional elements that produce spherically symmetrical distortions within the crystal. On the other hand, certain

interstitial elements produce nonspherically symmetric distortions and this leads to appreciable strengthening in the solute material. If the solute atom has an atomic size less than the host (solvent) atom (that constitute the material lattice) the dilation is negative, because the atomic volume is locally decreased in the solute atoms' vicinity. On the contrary, so far as it has a higher size than the host, the dilation results to be positive.

The resultant stress field due to the presence of a solute atom affects the one produced by dislocation accumulation, giving rise to an atom-dislocation interaction energy. Considering, as example, a moving dislocation encountering a smaller solute atom lying directly above its slip plane (Fig. 21), the interaction energy results to be negative. The small atom reduces the dislocation energy resulting from the compressed volume lying above the dislocation core. Hence, the interaction outcomes in an attraction effect from the dislocation to the solute atom. It is worth to notice that, if the small atom were lying directly below the glide plane, the situation would be reversed and a positive interaction energy would result, and the dislocation would be repelled by the solute atom [100, 101].
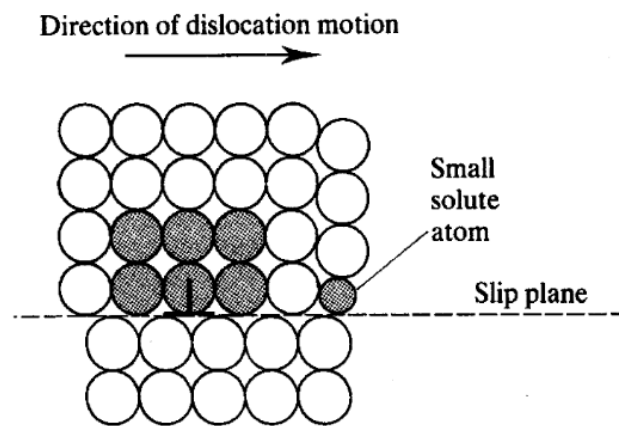
Fig. 21 Interaction between a moving (edge) dislocation on a slip plane containing a solute atom of lower atomic size than the solvent [100].

3.2.7 Particle Hardening

In general, small particles of a second phase dispersed in a matrix can markedly affect the material yield strength, even when the dispersoid volume fraction is low. This effect is due to the greater resistance to dislocation penetration shown by an aggregate of atoms respect to an insulated atom in solid solution. Furthermore, particle sizes of dimensions ranging around thousands atom diameters promote a hardening effect.

The interaction at interfaces between particles and matrix can depend by different issues, as example particles dimensions and/or their distribution into the solute matrix. Small particles produced by precipitation from supersaturated solid solutions frequently have interphase boundaries that are coherent with the matrix. Atomic bonds match up across such an ordered interface even though the interatomic spacing between particle and matrix may be different (Fig. 22a). Under these specific conditions, the lattice distortion gives rise to a coherency strain. Dislocations interact with the stress field of a coherent particle similar to the way they interact with solute atoms having a different size from the solvent. Conversely, during precipitation, coherency can be lost when the particle attains a certain size. Substantially, the energy associated with the strained interface becomes too high and it is replaced by a disordered interface (Fig. 22b). Similarly, disordered interphase boundaries are obtainable when the particle dispersion is "artificially" forced into the matrix, as example in powder metallurgy and ceramic processes. An intermediate structure (a partly ordered boundary, as in Fig. 22c) can also be found at particle matrix interfaces. In this case, the volume difference (and the resulting strain) between the particle and the matrix is partially accommodated by interphase boundary dislocations [100, 102, 103].
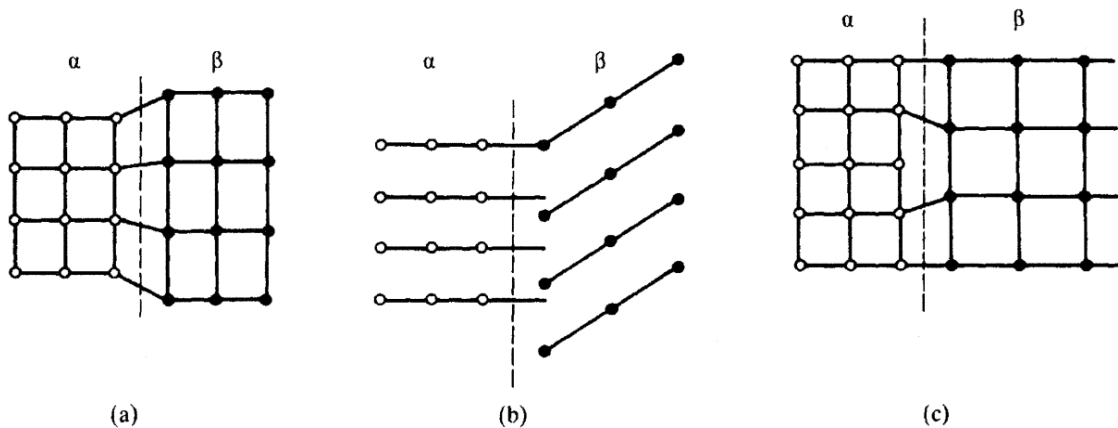
Fig. 22 Three types of interphase boundaries (α and β are the solute and the particle respectively). In particular, in (a) is shown a coherent or ordered interphase boundary exists between a α and β; in (b) is shown a fully disordered interphase boundary; while in (c) is reported an intermediate interphase boundary (or partially ordered) [100].

Coherent boundaries and small particles result in dislocations passing through (or "cutting") the particle, generating preferential paths for the dislocation motion and promoting the concentration of the plastic flow within their areas. On the contrary, when the particles result to be larger or with disordered interphase boundaries, dislocations tend to bow between them resulting in a consistent hindering of the dislocation motion (or "bowing"), consequently impeding of the plastic flow and

resulting in a general material hardening. Substantially, the occurrence of a softening or a hardening effect in the material is due to the predominance of dislocation "cutting" or "bowing" [100, 101, 104].

3.3. Background

The achievement of a general and well-defined theory of *CDD* modeling methodology of the materials work hardening has had an arduous path. The first endeavor to the formulation of the theory was taken in 30s by the pioneering research works of Taylor [75] and Orowan [105]. In particular, they introduced the relationship between the mesoscale mechanical variables, strain and strain rate, of a deformed metal with its yielding stress. They considered the main interaction phenomena between dislocations occurring during the material plastic flow in terms of dislocation density evolution. This modeling method was surely inadequate, both in terms of predicted work hardening rate and in terms of the stability of the dislocation structures. However, it represented the starting point to the definition of all the subsequent theories that were found in subsequent years. In late 50s and early 60s, the formulation of a work hardening theory was object of debate, dominated by the personalities of Alfred Seeger, Peter Hirsch and Jacques Friedel [66]. Despite all the different and conflicting opinions, the two fundamental matters of work hardening were established in good general agreement: the presence of an athermal hardening rate, and the existence of a phenomenon identified as, 'dynamic recovery', which characterizes the strongly temperature and rate dependent decrease of the hardening rate at very large strains. The decrease, is not dependent on diffusion, while it is strongly associated to the involved material stacking-fault energy (*SFE*) [106]. Later it was relieved that these two effects are strictly related with the "*Stage II*" and "*Stage III*" of the work hardening behavior, where the two effects tend to respectively predominate. Basing on their works, Johnston and Gilman [47] proposed an upgraded model that took into account the material dislocation density evolution as simple superposition of a hardening term and a recovery term, aiming to simulate the dislocation multiplication and annihilation phenomena. In subsequent years, a similar approach was widespread adopted in the plastic flow stress modeling strategies, as example by Bergström [48] and Mecking and Kocks [37]. Then, many physics based constitutive models were proposed taking into account the different typology of dislocation density. Bammann and Aifantis [49], Estrin and Kubin [50] classified the different dislocation density kinds with respect to their mobility features. In the same years, a new important discovery was taken by Sevillano et al. [107], they identified a low strain hardening rate deformed material's behavior at very large strains, subsequently baptized as "*Stage IV*". It appears to have a

number of variants, depending on material and temperature, and it is usually seen in torsion tests. In recent years Hansen et al. [51] and Li et al. [52] proposed a new classification regarding the arrangement of dislocations in their distribution network. Other important modeling approaches that incorporated the crystal grain size to the dislocation hardening-recovery phenomena, were proposed as example by Estrin and Mecking [53], Mukherjee et al. [54], and more recently by Motaman and Prahl [55].

Focusing on machining processes, physics based simulation methodologies, that are the main object of investigation of the presented research work, a first physics based approach to simulate the metallurgical effect of a general cutting process was proposed by Mohamed [108]. He used a dislocation density based flow stress relationship to predict the minimum grain size obtainable during ball milling process of various metals. The proposed model considered a balance between the hardening rate arising from the dislocation multiplication and the recovery rate induced by the dislocation annihilation. Afterwards, Ding et al. [109] developed a coupled phenomenological and dislocation density *FE* model, built on the *JC* model, to predict the grain refinement and microstructure evolution in orthogonal cutting of *OFHC* copper and *AA6061 T6* aluminum alloy. Subsequently, Ding and Shin integrated the same model to study the microstructural behavior of different metals. They investigated the microstructural effects of orthogonal machining on Commercially Pure Titanium (*CP-Ti*) [110] and of two different hard steels, *AISI 52100* [111] and *AISI 1045* [112]. All these works presented a modeling strategy able to predict the sub-grain modification caused by the high speed thermo-mechanical loads induced by machining process. Similarly, Liu and Melkote [113] exploited a *JC*-dislocation density based model as an investigation instrument, to explore the effects of different rake angles and the edge radius of the cutting tool on *Al5083-H116* aluminum alloy machinability in micro-cutting conditions, allowing to in depth understand the physics of an industrial process that is well-known to be extremely difficult to be explored. Another research concerning *Al6061 T6* was conducted by Wu et al. [114], they implemented the model proposed in [109] in a *FE* commercial software to study the effects of cutting tool microgrooves on the metallurgical evolution in terms of grain size and dislocation density. However, in these models, the researchers considered the plastic flow behavior and the microstructural modification separately and they made the assumption of considering grain cells as grain structures. Furthermore, Melkote et al. [86] considered a physics based modelling strategy to simulate the flow stress of *CP-Ti*, taking into account the grain refinement and dislocation accumulation phenomena in order to comprehend the serration behavior of the machined chip induced by the materials softening phenomena, including also the inverse *H-P* softening effect due to the ultrafine grains relieved into the adiabatic shear bands. Concerning the physics based

modelling of aerospace hard-to-machine alloys, Fernandez-Zelaya et al. [87] and Imbrogno et al. [72] demonstrated the importance of the employment of a validated physics based model to in depth comprehend the machining process variables of industrial interest. In detail, they studied the machining forces and chips as macroscale representative variables and the metallurgical evolution as microscale variables of experimentally investigated machining condition inside the chip shear bands and on the processed surfaces. More specifically, these latter works represent a first approach to in depth study the machinability of the hard-to-cut materials using physics based modeling as an analysis tool.

CHAPTER IV

In Chapter IV, all the experimental procedures and analysis methods are explained for all the three case studies. In particular, machining conditions are indicated for each processed material, giving a depth description of the experimental set up. The measurement instrumentation for the variables and measurements that are object of analysis are also described and the sample mounting, cleaning, grinding and polishing procedures, that have the objective of make the specimens manageable for the more sensitive microstructural analysis and measurements.

Experimental Procedures, Materials and Methods

In order to build up a performing numerical model, the validation procedures are of fundamental importance, hence a decent amount of experimental data is needed to verify the correctness of the numerical model. In detail, sufficient experimental tests are unavoidable to calibrate the parameter of the models or verify their accuracy. At first, these tests must concern the analysis of the material plastic behavior under different deformation conditions, such as tensile tests, Split-Hopkinson Pressure Bar (*SHPB*) tests, inverse analysis, etc. Furthermore, when the numerical model is used to simulate the severe plastic deformation process conditions, a second experimental validation is due, in order to evaluate the accuracy of the specific modeling strategy, that have to take into account more simplifications and approximations than the sole plastic description of the material behavior. In detail, when a general numerical model, with particular regard to *FE* method, is build, a certain number of approximations must be considered. They are indispensable to simplify the mathematical reproduction of the investigated phenomena, or in certain circumstances, the numerical model cannot even be solved avoiding them. These can refer to the geometrical description of the domain, its discretization, the numerical fitting of the material behavior, the proper reproduction of the tribological conditions between contact bodies, that are particularly difficult to be mathematically reproduced, and so on. Consequently, in order to have a global validation of the proposed physics based model, specific experimental tests were carried out for each investigated material under the process conditions of interest, these tests are described in subsequent sub-paragraphs.

4.1. *Waspaloy* - Orthogonal Machining under different Lubri-Cooling Conditions

The aerospace industries have to guarantee extremely high reliability and duration of the manufactured artefacts, consequently, one of the most important topics of interest into this sector concerns the prediction of the aero-engine component failure. This latter is extremely hard to be estimated, mainly because a complete and deep knowledge of the inner microstructural changes occurring during all the deformation history of the processed material cannot be obtained only via experimental analysis. Moreover, having a deep knowledge of the microstructural behavior of the material under large strain deformation can lead to the improvement of its mechanical properties. This improvement can be achieved optimizing the process parameters and conditions, with the aim of enhance thermo-mechanical performances of the processed material.

In the manufacturing of jet engines, the components produced by super alloys represent about 50% by weight. This broad contribution is mainly due to their superior mechanical performances under critical working conditions [115–117]. Although they have superior quality, they usually show poor machinability, indeed these materials are also known as "hard-to-cut" materials. Focusing on nickel-based alloys, *Waspaloy* is mainly used in jet engines rotating components manufacturing, thanks to its superior mechanical properties, high oxidation resistance, stiffness and strength to weight ratio [34]. In last decades, the researches focusing on this material are increasing, mainly because, many efforts are needed to adequately choose process parameters and lubri-cooling conditions, select the correct tooling, control the machine shop and consequently reduce the work in process [118].

In this context, the numerical simulations lead a significant contribution in improving the product quality by optimization of the manufacturing process parameters, without performing costly experiments. Moreover, the numerical simulation is a very effective approach for gaining fundamental insight into the evolution of the material microstructure during the metal cutting process [29]. Considerable progresses were reached in describing the constitutive relations using dislocation based models, particularly for pure metals and alloys. These complex models provide more information on microstructural modifications during the evolution of the deformed material flow and they consider these effects in the flow behavior [119]. Therefore, they represent a tool to analyze and understand the effects of the metallurgical micro-scale mechanisms.

Concerning *Waspaloy*, various researches on its mechanical behavior and metallurgical changes were carried out to date. Chamanfar et al. [120] studied the evolution of the flow stress and

microstructure at higher temperature performing isothermal compression tests. They proposed a phenomenological material constitutive model. The metallurgical evolution was well investigated, but the material behavior was not affected by the microstructural changes experimentally evaluated. Likewise, Shen et al. [121] performed hot compression tests under different thermo-mechanical conditions, investigating the microstructure modification they discovered different stages of evolutions. They implemented the microstructure model into FE simulations to predict detailed thermo-mechanical histories during forging. However, the material constitutive model did not take into account the microstructure evolution and its effects on the material behavior. In contrast, Del Prete et al. [122] developed a phenomenological constitutive model based on the workpiece initial hardness to simulate the material behavior of *Waspaloy* during machining. They validated the model through the prediction of the cutting forces, temperature into the cutting zone and chip morphology. Also Caruso et al. [31] proposed an innovative phenomenological modeling approach to take into account the microstructural changes effect on the material *JC* flow stress, implementing the developed model into FE software to simulate the machining process. It is clear by analyzing the literature, that the microstructure and metallurgical changes play an important role on the material behavior and, although several material behavior models have been proposed, these still show poor or missing links between the material modifications and the mechanical properties.

4.1.1 Waspaloy – Orthogonal Machining Experimental Procedures

Waspaloy disks of outer diameter 127 mm and thickness of 3 mm were bolted to a shaft and used as workpiece material. Orthogonal turning trials were performed in a random order, in order to get reliable results, three repetitions for each analyzed case were carried out (also randomized), using a MAZAK stiff high speed CNC turning center, by means of a radial facing operation. Test were performed using S quality rhomboidal 55° coated carbide tool with ISO code DNMG 15 06 12 - SMR S05F quality, mounted on a DDJNR 2525M 15 tool holder. The tool holder was held on a Kistler 9257 piezoelectric dynamometer, for forces detection: F_c (Cutting Force) and F_t (Thrust Force). A K-type thermo-couple, set in a slot behind the cutting tool at a distance of around 1 mm from the cutting edge, has been used to detect the local value of the cutting temperature beneath the cutting tool. Moreover, an infrared thermo-camera was used during the experiments to detect, having a known value of emissivity, the whole thermal field. In order to have a known and homogenous value of emissivity, the disks were painted using a black thermal-resistant paint. Taking into account that in wet conditions the lubricant could dilute the black paint on disks or affect the emissivity, the local temperature measured by thermocouple has been used to determine,

by inverse numerical methodology, the temperature at the tool cutting edge as in [123]. In particular, temperatures in cryogenic machining tests have been measured using both methodologies, avoiding the possibility that the fog due to evaporating cryogenic vapors could affect the thermal fields measured by thermo-camera. The temperature spectra given from the *IR* thermo-camera were taken as reference for the subsequent analysis, while the results obtained from thermocouple were used to confirm the affordability of the *IR* results. Depending on the cutting parameters, the cutting time of the experiments ranged from 60 to 300 s in order to reach the steady state conditions and to avoid final outer diameter of the disks too close to the shaft. The experimental tests were performed under three different cutting conditions: dry, wet and cryogenic. In wet condition the lubri-coolant was applied by a single nozzle to the area of interest, influencing all primary, secondary and tertiary shear zones. The lubri-coolant used in wet cutting condition was "Brugarolas Cutting Oil 4010062" at a flow rate ranging from 50 to 60 ml/s. Fig. 23 shows the general characteristics of the experimental set up, Fig. 24 shows the details of the different lubri-cooling technologies, and Fig. 25 shows the temperature influenced area that was taken into account in the *IR* temperature analysis.
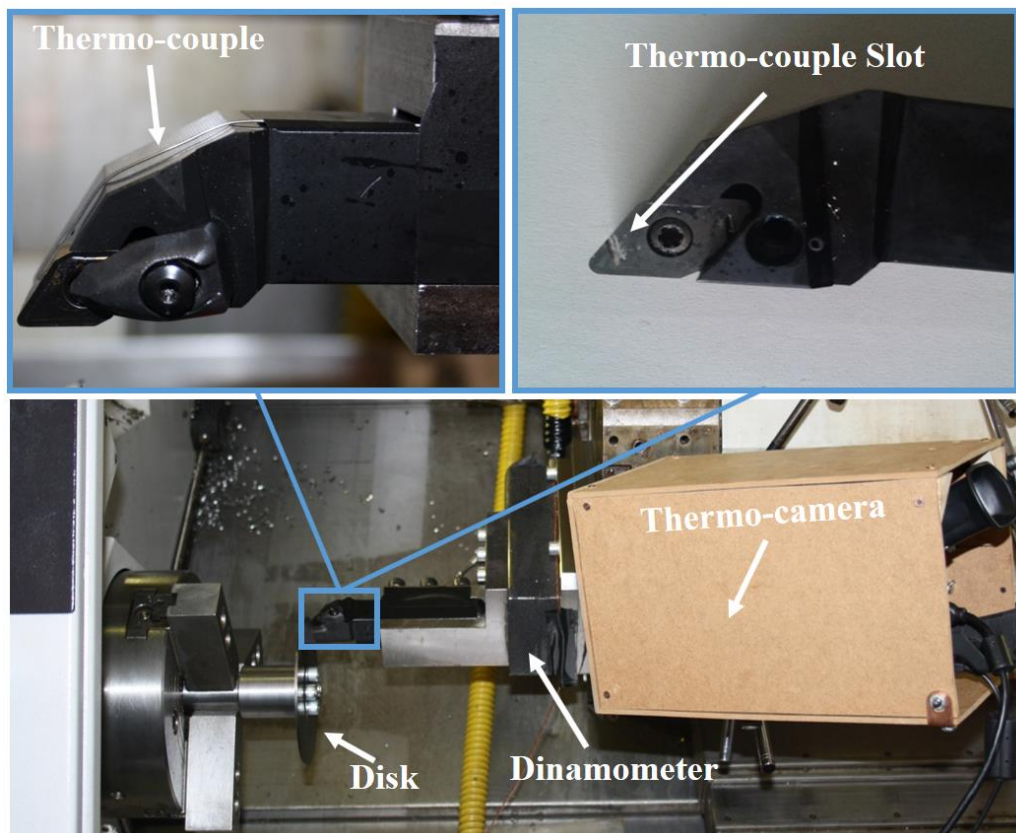
Fig. 23 Experimental set-up: orthogonal cutting with disk, dynamometer, thermo-couple and thermo-camera position [34].
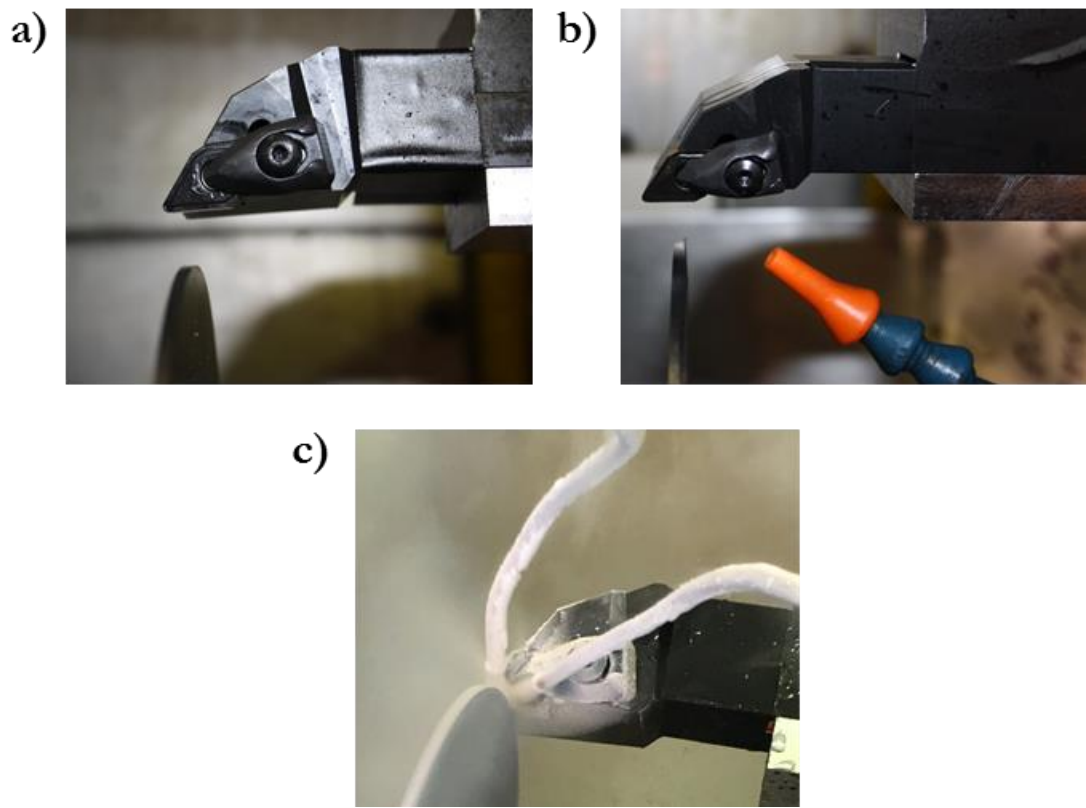
Fig. 24 Experimental set-up: a) dry orthogonal cutting, lubri-cooling nozzle position for b) wet and c) cryogenic experiments [34].
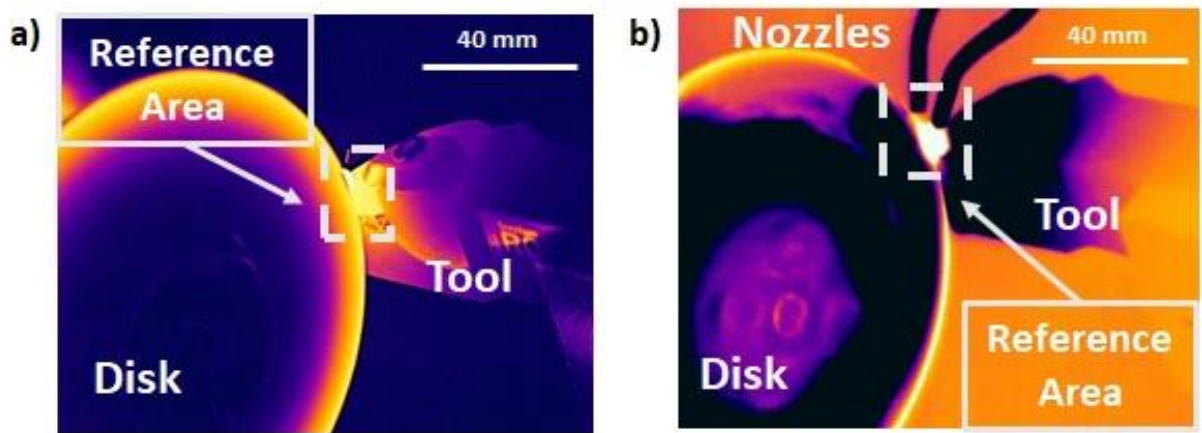
Fig. 25 Temperature fields in the reference area for a) dry machining and b) cryogenic machining condition [34].

As shown in Fig. 24c, in cryogenic cutting condition a couple of nozzles was positioned reproducing the experimental set up used in [35]. The inner diameter of both nozzles in cryogenic lubri-cooling system was 2 mm and the pressure of liquid nitrogen was regulated at 9 bar, with a flow rate of nearly 0.010 l/min. The nozzles were oriented to spray on the workpiece and not on the tool, in order to have a consistent improving on surface quality of the machined part.

4.1.2 *Waspaloy – Microstructural Analysis Methods*

Cross section samples of processed surface and machined chips were were mounted using a Struers® Citopress-1, mechanically polished using a Struers® Tegramin-25, and chemically etched for the metallurgical analyses. The samples were dabbed for 1 min using Kalling's no. 2 reagent (*CuCl2* 5 grams, Hydrochloric acid 100 ml, Ethanol 100 ml), while the grinding/polishing procedure is reported in Table 2.

Table 2 *Waspaloy* grinding/polishing procedure steps.

Cloth/Paper Name (Struers)	Granulometry	Suspension/Lubricant	Force per Sample [N]	Time [min]
Piano 220	69 μm	Water	30	1:50
Largo	9 μm	DiaP. All/Lar.9	30	3:30
Dac	3 μm	DiaP. Dac3	30	3:30
Chem	0.5 μm	OP-S	15	1:10

The microstructure of the worked surface and chips samples were analyzed using a Leica© DFC320 (1000x) optical microscope. The microhardness ($HV_{0.01}$) was measured on polished samples using a QNES 10 micro-indenter for 10 s of pause time.

The experimental plan was based on nine different combinations of three levels of cutting speed and three levels of feed rate, either for dry, wet and cryogenic cooling conditions (

Table 3), with a repeatability of three experiments for each test. For each test is reported the average value and the standard deviation (as error bar) of the three repetitions for each measured value.

Table 3 *Waspaloy* Experimental test conditions.

Cutting Speed [m/min]	Feed Rate [mm/rev]	Cutting Condition
40	0.05/0.10/0.15	Dry/Wet/Cryogenic
55	0.05/0.10/0.15	Dry/Wet/Cryogenic
70	0.05/0.10/0.15	Dry/Wet/Cryogenic

For what concern the dry machining tests at feed rate of 0.15 mm/rev and cutting speed of 55 and 70 m/min, these specific case studies shown an excessive wear that caused a premature catastrophic failure of the cutting tools, so they are not involved in any analysis of the different variables that are reported in this research. The force recording of the experimental tests and the relative worn tools are reported in Fig. 26.
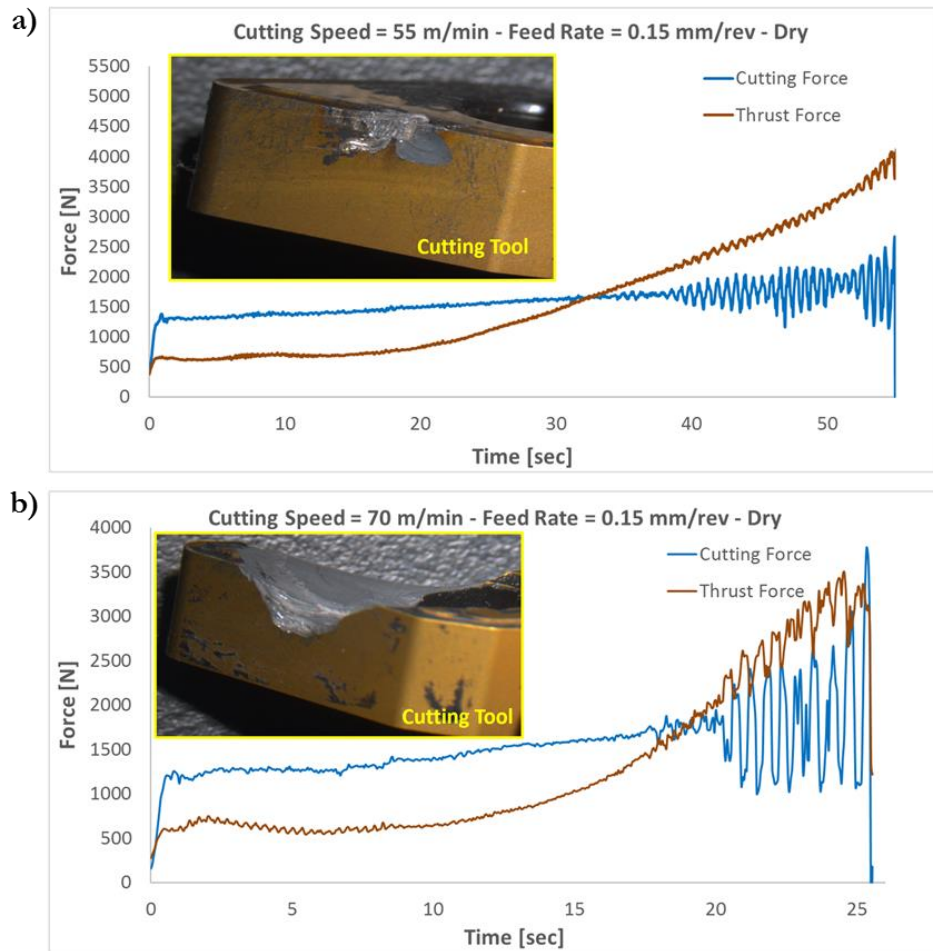
Fig. 26 Forces registered and worn tools in dry machining tests at feed rate of 0.15 mm/rev and at cutting speed of (a) 55 m/min and (b) 70 m/min [34].

Due to the consistent abrasive load that usually occur in *Waspaloy* machining, the tool wear rate was relieved and is reported in Fig. 27. As visible, cutting speed slightly affects the wear rate, while the feed rate has a significant effect on it, due to the higher portion of removed material. On the side of the exploited lubri-cooling techniques, wet machining conditions tends to reduce the abrasive loads because of the friction reduction and the capability of the fluid to remove particles and debris generated during the cutting process. On the other hand, these effects are not so consistent under cryogenic conditions, and the higher work hardening effect predominates, negatively affecting the wear resistance of the machining tool.
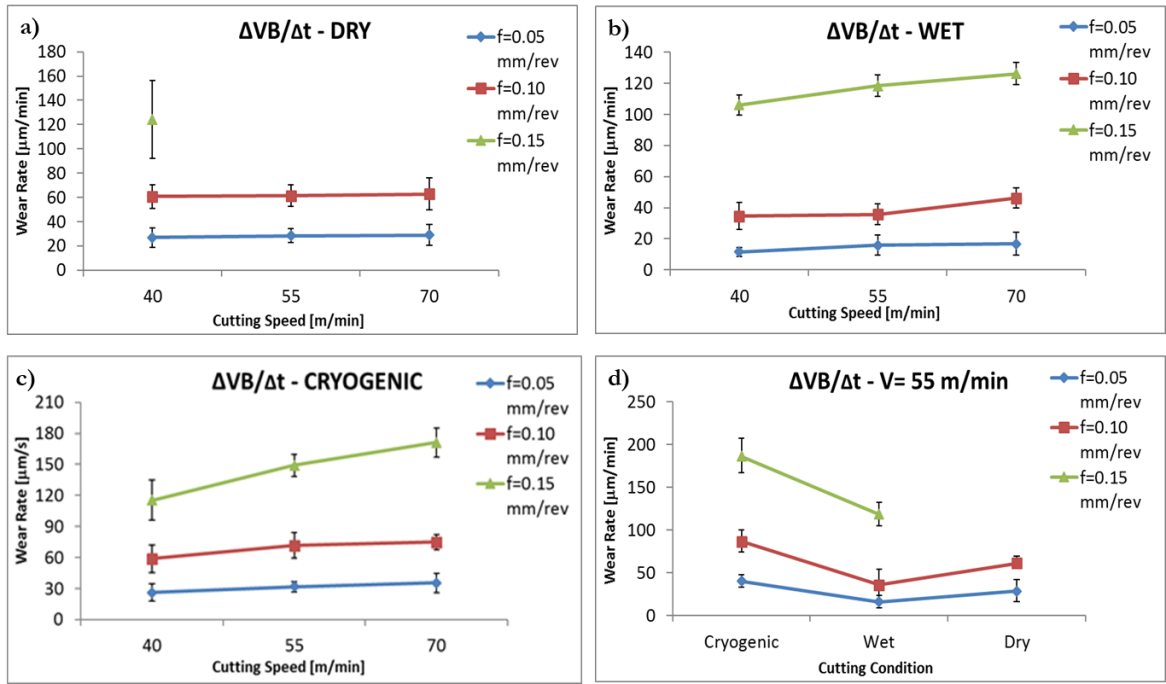
Fig. 27 Variation of tool wear rate at varying a), b) and c) cutting speed and feed rate, d) cooling condition for Waspaloy machining.

4.2. *CP-Ti* – **Orthogonal Macro/Micro Machining Process**

Dental implants are frequently produced by micromachining of Titanium (*Ti*) based materials, because of their passivity and mechanical properties, such as good biocompatibility, high corrosion resistance in body fluids, mechanical strength, and fatigue endurance. The mechanical characteristics of Commercially Pure Titanium (*CP-Ti*) are limited and cannot sustain high load-bearing situations. Indeed, the addition of alloying elements (*Al* and *V* for example) yields a significant improvement in its properties. Despite their superior characteristics, the use of *Ti* alloy based implants reveals elevated concentration of metal ions in the tissues around the implants, as well as in serum, urine, and even in tissues distant from the implants, therefore compromising their long-term safety. On the other hand, although *CP-Ti* can serve as a latent alternative to *Ti* alloys by lowering the risk of contamination, its low surface mechanical properties and poor heat treatability remain a limiting factor for such applications [124–126]. However, the surface mechanical properties of *CP-Ti* can be enhanced by inducing certain microstructural modifications that can be achieved through proper design of the manufacturing process, leading to the production of cheaper and safer implants that can potentially compete with those manufactured using *Ti* alloys [127, 128].

The manufacturing of dental implants requires a combination of processes; above all, these consist of machining operations such as turning, milling, boring, broaching, and threading [129]. Such a broad range of material removal processes highlights the importance of having a deeper comprehension of the material machinability in order to properly design the manufacturing process chain [34]. Furthermore, machining processes represent an interesting approach to locally induce Severe Plastic Deformations (*SPD*) on a processed part, causing conspicuous microstructural modifications, and thereby enabling the production of final products that exhibit superior performance [25, 26].

In a general machining process, the evolution of microstructure is governed by different microstructural phenomena that can result in strengthening of the machined surface. During *SPD* processes, strengthening effects are induced by changing the spatial distribution of the microstructure, leading to hindrance of dislocation motion, and giving rise to superior strength [24, 130].

Among the strengthening effects obtained from the microstructural modifications, those related to dislocation accumulation, crystal twinning, and the *Hall-Petch* (*H-P*) effects are dominant [131, 132]. Several authors have demonstrated that the best durability enhancement of dental implants is obtained by enhancing their surface hardness, resulting in a consistent improvement of its surface wear resistance and frictional properties [133, 134]. Therefore, a clear understanding of material strengthening effects occurring in the machined material is important to optimize the process parameters so that the material strengthening phenomena can be suitably controlled [72, 135].

The available materials micro/nanostructure investigation techniques, such as Digital Image correlation (*DIC*), Electron Back-Scatter Diffraction (*EBSD*), Atom Probe Tomography (*APT*), Small-Angle Neutron Scattering (*SANS*) and Transmission Electron Microscopy (*TEM*), focus on detection of the global effects of strain fields on the material macro/micro state. Once detected, these effects have to be related to the material flow behavior using mathematical models in order to get information about the global strengthening, not providing particularly accurate information about the contributions of different metallurgical phenomena that may be active [136, 137]. On the other hand, a different approach to investigating local material strengthening involves micro/nanohardness measurements. This inspection strategy can only afford information about the localized yielding/hardening status of the material, without giving any information about the physical origin of the different strengthening phenomena [138, 139].

Therefore, it can be extremely difficult or even impossible to have a deep and precise comprehension of the respective contributions of the underlying material strengthening mechanisms. In this context, physics based modeling of the material flow behavior represents a fundamental means to make up for the lack of capabilities of measurement instrumentation and in addition allows investigation of the metallurgical phenomena active during the manufacturing process.

While several researchers have analyzed the flow behavior of severely deformed metals using different numerical simulation approaches [29, 140], only a small number of the reported studies concern physics based modeling of machined *CP-Ti*. Ding and Shin [110] used a coupled Johnson-Cook and dislocation based modeling approach to simulate orthogonal machining process of *CP-Ti*, predicting the sub-grain modification caused by the machining induced large deformation fields, making the assumption that cell structure can be considered as grain structure. Melkote et al. [86] implemented a physics based model that took into account the grain refinement and dislocation accumulation phenomena in order to comprehend their effects on the chip serration due to flow softening caused by the inverse H-P effect. Nevertheless, none of these models considers crystal twinning and dislocation strengthening effects separately. As reported by Alexandrov et al. [141], crystal twinning plays a central role in the hardening of hexagonal close packed structure (hcp) materials such as *CP-Ti*. Therefore, in order to properly understand the role of different strengthening mechanisms on surface hardening in machining, the individual material strengthening mechanisms have to be modelled and their relative contributions analyzed [142, 143].

4.2.1 CP-Ti – Orthogonal Macro/Micro Machining Procedures

Orthogonal tube dry cutting experiments of *CP-Ti* grade 2 were performed on a *CNC* lathe. The tubes were annealed for 2 hr at 800°C to relax any residual stress [135]. To ensure plain strain conditions, the tube wall was restricted to 3 mm and machined using a fresh TPG321 Grade HT10 Carbide Sharp insert for each experimental test. This specific insert provides rake and clearance angles of 0° and 11°, respectively, a cutting edge length of 16.5 mm and a small cutting edge radius (15±1 μm). The insert was held in a Hertel CTAP toolholder in turn fixed to a Kistler 9257B dynamometer to monitor the evolution of the main cutting force (F_t) and thrust force (F_t). Three different cutting speeds (15, 20, 25 m/min) and feed rates (0.04, 0.06 and 0.08 mm/rev) were used and four repetitions of each experimental case study were performed. The choice of parameters

was set by ensuring consistency with a range that can involve both micro and macro cutting conditions, in accordance with scientific literature [144, 145].

4.2.2 *CP-Ti – Microstructural Analysis Methods*

Each machined surface and chip sample was sectioned using a metallographic saw taking care to cut the sample far from the region of study and being sure not to contaminate the metallurgically induced modifications. Cross section samples of processed surface and machined chips were mounted using a Struers® Citopress-1, mechanically polished using a Struers® Tegramin-25, and chemically etched for the metallurgical analyses. The samples were immersed for 20 s using Kroll's reagent (92 ml of distilled water, 6 ml of HNO_3, 2 ml of HCl), while the grinding/polishing procedure is reported in Table 4.

For the metallurgical analyses both an optical microscope (Leica 320 - 1000x) and a scanning electron microscope (Tescan MIRA FE-SEMs) were used, while the microhardness ($HV_{0.05}$) of the surface and sub-surface layer was measured by means of an instrumented Buehler 1066-6406 micro-indenter.

Table 4 *CP-Ti* grinding/polishing procedure steps.

Cloth/Paper name (Struers)	Granulometry	Suspension/Lubricant	Force per Sample [N]	Time [min]
SiC Foil #320	46 μm	Water	15	3:00
SiC Foil #500	30 μm	Water	15	3:00
SiC Foil #800	22 μm	Water	15	3:00
SiC Foil #1200	15 μm	Water	15	3:00
SiC Foil #2000	12 μm	Water	15	3:00
Largo	9 μm	DiaP. All/Lar.9	30	4:40
Dac	3 μm	DiaP. Dac3	30	2:20
Chem	0.5 μm	OP-S	15	10:00

4.3. *Ti6Al4V* – 3D Machining Under Different Lubri-Cooling Conditions

Titanium alloy *Ti6Al4V* is the most commonly used (*α+β*) dual phase titanium alloy which can work below 500°C, and it represents an outstanding choice for high performance structural applications involving the main areas of the industrial scenery, including the aerospace, automotive, biomedical and chemical sectors. Such broad and diversified range of applications is due to its exceptional thermo-mechanical and chemical properties, mainly represented by its unique combination of strength-to-weight ratio, high yield and fatigue strength, and huge creep and corrosion resistance [146–148].

On the other hand, considering the low machinability of *Ti6Al4V*, due to its microstructural and chemical properties often resulting into accelerated wear of the cutting tool, the proper design of the process parameters and their optimization still represents a challenge for the manufacturers. Consequently, aiming to produce high performance artefacts, many research studies need to be conducted to lead the designers in a correct integration of this process into a high performance manufacturing chain [40]. In order to address this issue, the mathematical modeling strategies denote a necessary support to connect the material characteristics and the process operating conditions. It allows to obtain a better understanding of the physical and chemical mechanisms underlying the material processing and to predict the final product characteristics. Thus, it is possible to optimize the existing systems and processes, improve the product quality, develop new processes, and produce a variety of new materials, while expansive and time consuming experimental campaigns are avoided [41].

In the simulation of machining processes, the plastic flow stress behavior plays a fundamental role to correctly reproduce the thermo-mechanical evolution of the material, relating the physics variables involved during the metal deformation (strain, strain rate, temperature, microstructure, etc.) with the resulting stress occurring at different deformation fields.

Referring to last decades' studies, a dominant role in material behavior modeling during high strain rate deformation is played by physics based modeling strategies. These latter represent a fundamental tool to relate the starting microstructural status of a polycrystalline material and its evolution during large deformation processes with the material viscoplastic stress, giving important information on its metallurgical characteristics that are of fundamental importance to design the inner integrity of the final product [149]. These models can give a detailed description of the occurrence of microstructural evolution, which facilitates deeper understanding of metallurgical

alterations during the high strain rate jump that are typical of the machining of polycrystalline materials [150].

4.3.1 Ti6Al4V – 3D Machining Procedures

Turning tests were conducted on *Ti6Al4V* bars with a diameter of 10 mm (382 $HV_{0.01}$) at fixed feed rate and depth of cut of 0.15 mm/rev and 0.05 mm respectively. The tests were conducted on a Mazak® Quick Turn Nexus 220-II CNC lathe at varying cutting speed (30, 50 and 70 m/min) as visible in Fig. 28a. The lathe was equipped with a self-designed cooling line to supply different cooling and lubrication strategies, involving dry, cryogenic cooling, High Pressure Air Jet (*HPAJ*), and Minimum Quantity of Lubricant (*MQL*), as visible in Fig. 28b, Fig. 28c, and Fig. 28d, respectively. The *HPAJ* and the *MQL* tests were performed applying respectively air and vegetable oil emulsion through a single external nozzle (with a section of nearly 0.8 mm^2 in both conditions) to the cutting zone at the pressure of 7 bar (with a rate of 60 ml/h for the *MQL*). The nozzle had a section of nearly 0.8 mm^2 in both the lubri-cooling conditions, and in *MQL* tests the oil emulsion was made to drip by gravity. In contrast, the cryogenic coolant (*LN$_2$*) was applied at the pressure of 9 bar and a flow rate of nearly 0.010 l/min, through two nozzles (with a diameter of 3 mm) to the cutting region.

Coated Coro Cut *N123H2-0400-RO 1105 PVD TiAlN* insert with a clearance angle of 7° and a rake angle of 0°. The cutting tool edge radius was measured to be 15 µm by means of a no contact 3D confocal profilometer. The rake face was flat oriented in the tool holder (Sandvik RF123H25-2525BM) that was fixed to a Kistler 9257 three component piezoelectric dynamometer in order to monitor the evolution of the cutting forces during the process permitting to obtain the steady state mean values for the subsequent analysis. Furthermore, a thermocouple (K-type) was embedded into the tool-holder and the tool interface to measure the local temperature at the cutting tool back, at a distance of around 1 mm from the cutting edge, during machining (Fig. 28e). This temperature was used to determine the temperature at the interface between the cutting tool edge and the machined surface by an inverse numerical methodology as done in [34].

Coupled with the described methodology, the cutting temperatures at the tool-workpiece interface were also investigated employing an *IR* thermo-camera in order to get information not only at the tool-workpiece interface, but also concerning the areas around it. In order to get the best temperature spectra recording, the emissivity of the material was calibrated before the experimental procedures. Moreover, during the *IR* temperature acquisition, some reflections were

relievable on the processed material, that can affect the temperature measurements. Therefore, in order to avoid any affection on the temperature measurement by this effect, for each repetition a different shot was considered, improving the affordability of the measurement. It is important to point out that the cutting temperatures in cryogenic machining tests have been measured using both (*IR* camera and thermocuple inverse numerical method) methodologies, avoiding the possibility that the fog due to evaporating cryogenic vapors could affect the thermal fields measured by thermo-camera.

The cutting temperature taken as reference for the experimental analysis and the numerical model validation is the maximum one developed on the workpiece into the shown reference area registered by the *IR* thermo-camera (Fig. 28e), while the temperature relieved using the thermocouple was used to confirm the affordability of the *IR* temperature measurement at the tool-chip interface.
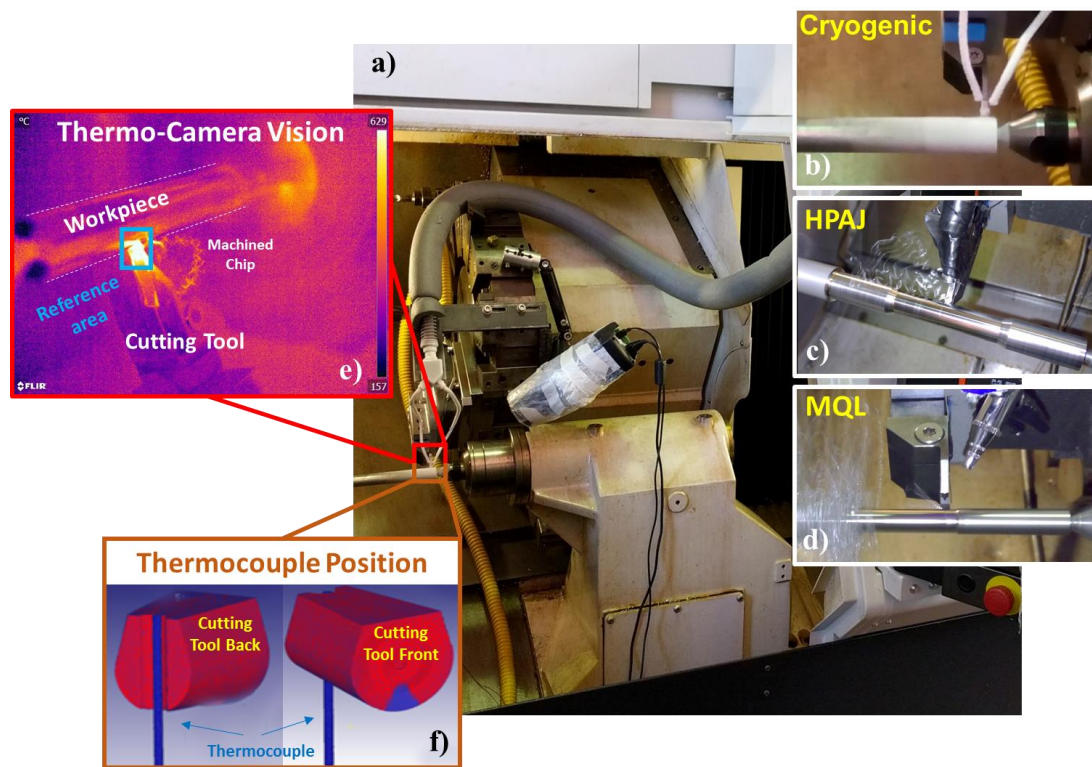
Fig. 28 Experimental set-up for machining test (a), nozzle configuration for Cryogenic (b) HPAJ (c), MQL (d) and cryogenic lubri-cooling, particular of the thermo-camera vision (e) and thermocouple position (f).

4.3.2 *Ti6Al4V – Microstructural Analysis Methods*

The machined surfaces of each experimental test investigated were cut out from the samples and mounted into a resin holder for microstructural analysis and hardness measurements. The samples were mechanically polished and etched using Kroll's reagent (92 ml of distilled water, 6 ml of nitric acid, 2 ml of hydrocloridric acid), while the grinding/polishing procedure is reported in

Table 5.

The microstructure was analyzed by means of an optical microscope LEICA DFC 320 (until 1000x of magnification), while the microhardness ($HV_{0.01}$) was measured on polished samples by means of a *QNES10* micro-indenter using 10 s of holding time.

Table 5 *CP-Ti* grinding/polishing procedure steps.

Cloth/Paper name (Struers)	Granulometry	Suspension/Lubricant	Force per Sample [N]	Time [min]
SiC Foil #320	46 μm	Water	15	3:00
SiC Foil #500	30 μm	Water	15	3:00
SiC Foil #800	22 μm	Water	15	3:00
SiC Foil #1200	15 μm	Water	15	3:00
SiC Foil #2000	12 μm	Water	15	3:00
Largo	9 μm	DiaP. All/Lar.9	30	4:40
Dac	3 μm	DiaP. Dac3	30	2:20
Chem	0.5 μm	OP-S	15	10:00

4.4. *Short introduction to the experimental results*

In order to have a better comprehension of the presented work, a brief introduction to the experimental results is here presented. However, the experimental results of each experimental campaign will be singularly and expansively discussed and compared with the numerical predictions in Chapter VI. Severer machining conditions cause significant increments in thermal loads on the cutting tool and on the processed surface, with a subsequent increasing of cutting temperatures at the tool-workpiece interface. Depending on the considered material and on the selected process parameters, the temperature raising can trigger or not the thermal softening effects occurring on the worked material. Moreover, there is a strengthening effect that concurs with the thermal load

and is directly related to the increasing of the cutting speed (and consequently the strain rate). As example, for *CP-Ti* machining tests the machining conditions were slighter (with a consequent slight increasing in machining temperatures) than in *Waspaloy* study, consequently in the first case the strengthening effect tends to be more relevant than in the second one. In fact, in *Waspaloy* machining tests the cutting forces diminish with the rising cutting speed, while for *CP-Ti* tests they are not significantly affected by thermal softening, causing a slight affection of the cutting speed on the machining forces. For what concerns the microstructural (and consequently the microhardness) modifications, the effects are extremely dependent by the deformation energy induced by the different cutting conditions. In general, severer machining conditions result in a hardened surface, however if this energy is higher enough to trigger the dynamic recrystallization phenomenon, an increased hardening is relievable on the processed surface, due to the grain refinement layers that could be generated on the machined surface and extremely below it. For what concerns the different studied lubri-cooling conditions, depending on the employed fluid the effects on the material can be extremely different. *HPAJ* methodology affects only the temperatures at tool-workpiece interface, while the friction conditions tend to remain the same. Moreover, the effects of this technique tend to be less efficient with the rising cutting speed, resulting in a machining process that is scantly different from dry conditions. Lubri-cooling conditions that employ oils affect both cutting temperatures and friction behavior. More in detail, traditional wet machining results in a relevant reduction of temperatures and friction at the tool-workpiece interface, lightening the machining effect on the processed surface, while *MQL method* tends to affect majorly the friction behaviour with a limited effect on the interface temperature, due to the limited cooling effect of the oil emulsion drops. In these cases, the forces and temperatures reduction are more relevant than using *HPAJ*. On the other hand, cryogenic based lubri-cooling shows completely different effects. The consistent temperatures reduction results in a huge material strengthening, negatively affecting the machining forces, also considering the poor lubricant capabilities of LN_2 [198]. The explained effects also result in a higher surface hardening effect, causing a consistent quality improvement on the machined surface. In essence, the employment or not of a lubri-cooling method is strongly related to the final product desired performances and if the stakeholders can sustain the implementation cost of this techniques to reach them.

CHAPTER V

In this chapter, the various steps of the plastic flow behavior modeling procedure are reported for each investigated material. In particular, so-far-as insufficient information on its rheological modeling are available in scientific literature, a first microstructural analysis of the processed material is carried out. This is fundamental to have a clear comprehension of any physics/metallurgical phenomena occurring in the deformed material, allowing to identify the various strengthening or softening material before finding a mathematical expression that can properly represent them.

Metallurgical Based Modeling Methods

In a general machining process, surface modifications are directly related to the material dynamic evolution during the process that affects the thermo-mechanical properties of the materials. The physics phenomena are difficult to be experimentally evaluated during the cutting operations and frequently also on the processed material. The comprehension of these phenomena represents the basis for a correct representation of the plastic stress behavior of the investigated materials. Moreover, it is worth to notice that on different materials can occur different physics phenomena, even if the deformation conditions are similar, or the same phenomenon can be negligible depending on the studied material main characteristics (stacking fault energy, initial microstructure, different atomic interactions involved, etc.). Therefore, in order to build up an efficient plastic flow modeling it is of fundamental importance to analyze the processed material, in order to grasp the physics/metallurgical phenomena occurred at microstructural level and exploit the analysis to mathematically simulate the various relieved strengthening/softening phenomena [48, 151, 152].

5.1. *Waspaloy* – Plastic Flow Modeling

In order to ensure the designed mechanical properties of *Waspaloy* made artifacts, a deeper knowledge of physics correlation between the mechanical behavior and the microstructural evolution under high dynamic loading is required. Thus, the main aspects studied are:

(i)   to investigate the deformation mechanisms of the *Waspaloy* machined under different lubri-cooling conditions and cutting parameters;

(ii)   to develop a physically based constitutive model to simulate the material behavior during orthogonal machining;

(iii)   to develop a Finite Element strategy for numerical prediction of the surface integrity during machining of *Waspaloy*.

5.1.1 *Waspaloy – Deformation Mechanisms*

Generally, during metal machining processes, the material is subjected to severe plastic deformation fields and the mainly interested regions are both the surface-subsurface zone and the chip. The metallurgical phenomena induced by the tool action are usually characterized by strongly deformed grains (shape modification), changes in dislocation density and their accumulation region, grain refinement (dynamic recrystallization that lead to new microstructures formation) as well as precipitation and phases modifications [37, 153]. Nickel-based super alloys, when subjected to machining operations, usually show recrystallized and highly deformed region within the grains and different altered layers on varying the deformation severity on the processed surface and subsurface of the worked material. Normally the affected layer shows the generation of slip band, grains elongation in the cutting direction, white layer formation and dynamic recrystallization due to the thermo-mechanical loads induced by manufacturing processes [37, 115]. Concerning *Waspaloy*, a schematic representation of the different metallurgical phenomena induced by different rate of plastic deformations is represented by Fig. 29.
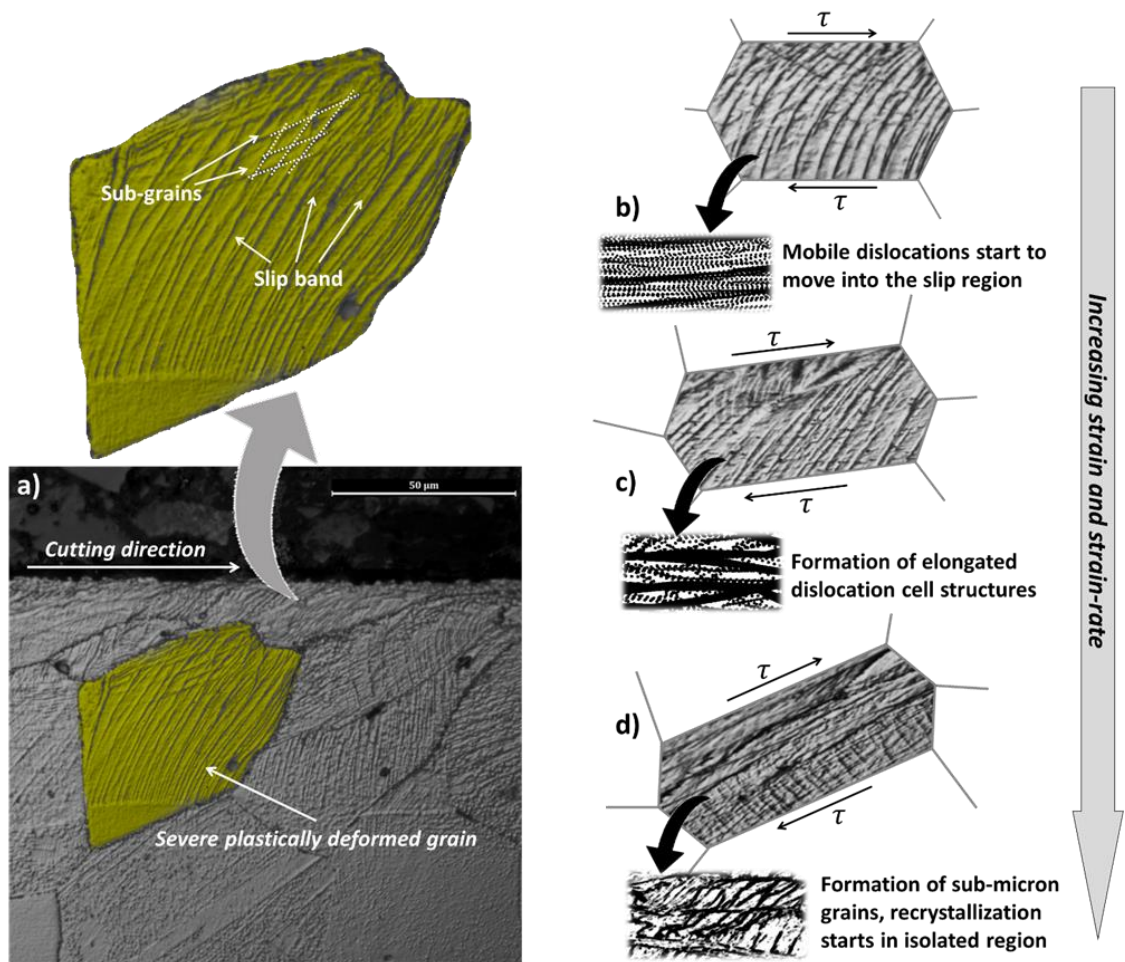
Fig. 29 Deformation mechanisms induced on *Waspaloy* machined surface; (a) V_c = 55 m/min f = 0.1 mm/rev dry condition, (b), (c) and (d) different stages of deformation mechanisms.

Fig. 29a is representative of the machined material cross section. The strongly deformed grains were isolated to investigate the different deformation mechanisms (Fig. 29b, Fig. 29c and Fig. 29d). At lower aggressive machining conditions (low feed rate and cutting speed) the main deformation mechanism that characterize the microstructure is represented by Fig. 29b. The grains subjected to plastic deformation show wide regions of slip band concentrations. The glide of many dislocations, resulting in slip bands, is the most common manifestation of plastic deformation in crystalline solids, causing in the increasing of the material strength (strain-hardening). Their presence represents the paths of dislocations during movement, that happens in the direction where the atoms are most closely spaced [66]. When strain and strain rate increase (corresponding to the increasing of cutting speed and feed rate), slip bands affected areas start to form cell structures due to the double-cross slip mechanism. This effect leads to the growth of slip bands by the sidewise spreading of slip, as shown Fig. 29c. The double-cross slip events of smaller intensity may lead to

multiplication at higher stresses, while the slip bands tend to become narrower at low temperatures [154, 155]. When machining conditions became aggressive, then sub-micron grains with sharp boundaries are formed in severer deformation conditions, due to the reorganization of the dislocations within the dislocation cells (Fig. 29d) and some grains start to recrystallize [156], resulting in material strengthening due to *Hall-Petch* effect [157].

The different deformation mechanisms described before are visible in the machined chip and both in machined surface and sub-surface (Fig. 30).
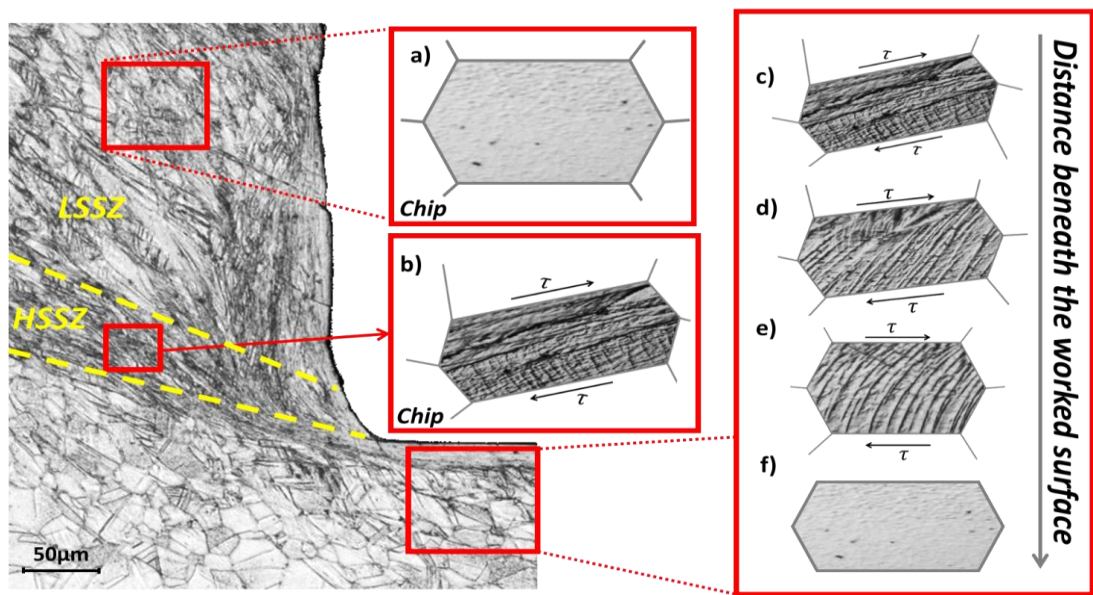
Fig. 30 Different deformation mechanisms in chip (a) and (b) and beneath the machined surface (c), (d), (e) and (f).

In serrated chip, two different deformation mechanisms are visible in two insulated zones identified as the Low Shear Strain Zone (*LSSZ*) and the High Shear Strain Zone (*HSSZ*). In *LSSZ*, that is far from shear band, the microstructure showed poor deformation and the grains had almost the same size of the as-received microstructure (Fig. 30a). In *HSSZ*, that is within the shear band, it was possible to observe elongated grain structures and grain refinement due to the extremely large deformations (Fig. 30b). Analyzing the microstructure of the machined surface, it is possible to notice that all the previously explained deformation mechanisms are clearly visible. Indeed, in the region that is the closest to the worked surface, the grain refinement is quite appreciable (Fig. 30c). This result was very highlighted when severer cutting conditions were adopted. Generally, the highly deformed microstructure was always present in each sample (Fig. 30d). From the worked surface to the depth, the effects of the large deformations fade away, showing slight deformation

effects (Fig. 30e) in the sub-surface and undeformed microstructure distant from the machined surface (Fig. 30f).

5.1.2 *Waspaloy – Physics Based Model*

The real description of the material behavior in terms of true stress-true strain represents a key role for understanding the reasons of the mechanical response of the manufactured components under different strain, strain rate and temperature conditions. Physics based models are preferred because they can catch the natural phenomena dominating the deformation basing on the physics events coupled with the microstructure evolution [66]. In this case study, a physically based plasticity model for *Waspaloy* has been developed and implemented in machining simulation. The macroscopic flow stress is assumed to consist of additive long range and short range contributions (Eq. 3).

$$\sigma = \sigma^* + \sigma_G + \sigma_{HP} \tag{3}$$

where σ^* is the *Peierls* Stress. σ_G denotes the long range strengthening induced by dislocation accumulation, while σ_{HP} is the *Hall-Petch* stress.

5.1.2.1 *Long Range Contribution - Dislocation Hardening*

The long-range contributions are sometimes considered as athermal contribution because the thermal vibrations cannot assist a moving dislocation to pass the region subjected to long range lattice modifications due to grain boundary or dislocations forests [158].

The long range interaction due to the interference among moving dislocations and immobile dislocations is the physical basis of the strain-hardening of a metal. This contribution to the material resistance is represented by σ_G (Eq. 4) [159].

$$\sigma_G = \alpha M G b \sqrt{\rho_i} \tag{4}$$

Here, α is a proportional constant, M is the Taylor factor, ρ_i is the density of immobile dislocations and G is the temperature dependent shear modulus, b is the Burger's vector (2.50E-10 m [160]).

The immobile dislocation density evolution is described by Eq. 5 (accumulation of dislocation evolution) [161, 162]. The evolution equation consists of two terms: $\dot{\rho}_i^{(+)}$ that is representative of the hardening and $\dot{\rho}_i^{(-)}$ that is representative of the softening effect due to the recovery phenomena.

$$\dot{\rho}_i = \dot{\rho}_i^{(+)} - \dot{\rho}_i^{(-)} \tag{5}$$

The mobile dislocations may encounter obstacles that prevent further movement and as a result become immobilized due to the trapping effect of the obstacles. Moreover, when dislocations are moving next to the grain boundaries can be annihilated by the interactions with dislocations of opposite sign. The increase in dislocation density is assumed to be proportional to the plastic strain rate (Eq. 6) [163, 164].

$$\dot{\rho}_i^{(+)} = \left(\frac{1}{s} + \frac{1}{D}\right)\frac{M}{b}\dot{\varepsilon} = \frac{M}{b\Lambda}\dot{\varepsilon} \tag{6}$$

Where $\dot{\varepsilon}$ is the equivalent plastic strain rate and Λ interprets the mean free path of a moving dislocation until it is immobilized. In the Eq. 6, D and s represent the grain size and the cell size respectively. The cell size is assumed to be inversely proportional to the square root of the immobile dislocation according to Eq. 7 [165].

$$s = K_c / \sqrt{\rho_i} \tag{7}$$

where K_c is a calibration parameter.

Different processes may contribute to the reduction of the dislocation density. They are separated into static and dynamic recovery as (Eq. 8):

$$\dot{\rho}_i^{(-)} = \dot{\rho}_{sr}^{(-)} + \dot{\rho}_{dr}^{(-)} \tag{8}$$

The $\dot{\rho}_{sr}^{(-)}$ represents the static recovery. This formulation is depending on some physics constants as Boltzmann's constant (k_b) and self-diffusivity models. It is also depending on grown of dislocation density that is used in the model to prevent that the dislocation density become zero when very long times are considered in the process. In the machining simulation, a very short interval time proportional to 1E-7s is considered, consequently its contribution ($\dot{\rho}_{sr}^{(-)}$) was neglected. On the contrary, the dynamic recovery term is proportional to the immobile dislocation density and the plastic strain rate (Eq. 9). The dynamic recovery implies that moving dislocation annihilates the immobile ones.

$$\dot{\rho}_{dr}^{(-)} = \Omega \rho_i \dot{\varepsilon} \tag{9}$$

where Ω is a recovery function and its expression is reported in Eq. 10

$$\Omega = \Omega_0 + \Omega_{r0} \left(\frac{1}{\dot{\varepsilon}^p} \frac{D_v}{b^2} \right)^{1/3} \tag{10}$$

$$D_v = D_{v0} exp(-Q_v/k_b T) \tag{11}$$

Where Dv (Eq. 10) is the material self-diffusivity, Ω_0 and Ω_{r0} are two calibration parameters, D_{r0} is a numerical constant, and Q_v is the activation energy for self-diffusion. As reported in literature, the recovery for the dislocations takes place mainly in the cell walls and this process is due to climb controlled by excess vacancies created during deformation [161, 162, 164, 166].

5.1.2.2 Long Range Contribution - Hall-Petch Effect

The *Hall-Petch* effect is due to the resistance to dislocation motion offered by grain boundaries. In detail, this effect is due to the pile-up of dislocations at grain boundaries leading to the activation of other slip systems in the surrounding grains [167]. The representative model of the *Hall-Petch* contribution to the flow stress is computed as showed by Eq. 12:

$$\sigma_{HP} = k_{HP}/\sqrt{D} \tag{12}$$

Where D is the grains size. As grains are refined progressively, once they decrease under a critical value the material strength starts to decrease. This phenomenon is commonly referred to the inverse *Hall-Petch* effect and different physical explanations are available in literature [168–170]. The coefficient k_{HP} catches this physics phenomenon that is particularly evident (Fig. 29 and Fig. 30) as a grain boundary sliding coupled with significant grain refinement. This results in a softening effect on the material constitutive behavior and this effect is captured by Eq. 13 [86]:

$$k_{HP} = \alpha_G^0 tanh \left(\frac{d}{D^{-0.5}} \right)^\nu \tag{13}$$

Where α_G^0, d and ν are calibration parameters.

5.1.2.2.1 Grain Size Evolution

The grain size D has been computed taking into account the common mixture law (Eq. 14):

$$D = D_{DRX}X_{DRX} + D_0(1 - X_{DRX})$$ (14)

Where D_0 is the average initial grain size (41 μm), X_{DRX} is the volume of the recrystallized microstructure and is represented by the Avrami model asserting that the DRX has a sigmoidal evolution showed by Eq. 15. It depends on strain ε, while ε_{cr} is the critical strain for the nucleation of the recrystallized grains (Eq. 16) and $\varepsilon_{0.5}$ (Eq. 17) that is the strain referred to the 50% of recrystallized microstructure. Generally, the ε_{cr} is equal to the 80% of ε_{peak} (Eq. 18) that denotes the strain corresponding to the maximum stress. The D_{DRX} is the dynamically recrystallized grain size computed as shown by Equation 16. The D_{DRX} is a function of two material constants and the Zener-Hollomon parameter (Eq. 19). The constant R in Eq. 17 is the universal gas constant.

$$X_{DRX} = 1 - exp\left(-\log 2\left(\frac{\varepsilon - \varepsilon_{cr}}{\varepsilon_{0.5}}\right)^3\right)$$ (15)

$$\varepsilon_{peak} = 5.375 \cdot 10^{-4} D_0{}^{0.54} Z^{0.106}$$ (16)

$$\varepsilon_{0.5} = 0.1449 D_0{}^{0.32} Z^{0.03}$$ (17)

$$D_{DRX} = 8103 Z^{-0.16}$$ (18)

$$Z = \dot{\bar{\varepsilon}}^p exp\left(\frac{468000}{RT}\right)$$ (19)

The Equations from 15 to 19 are taken from [121] and from [171]. In particular, they refer to the microstructural evolution during thermo-mechanical deformations at temperature lower than 1010 °C. As a matter of fact, no thermal gradient higher than 750 °C was reached during the experimental cutting tests and this result justifies the decision to choose these set of equations, although in the work of Shen et al. [121] are developed the equations for higher temperatures as well.

5.1.2.3 Short Range Contribution – Peierls Strengthening

The σ^* term represents the material resistance to plastic deformation due to the short range interactions where thermal activated mechanisms assist the applied stress in moving dislocations through the lattice (Eq. 20). Short range obstacles are a general classification of any disturbance of the lattice that is 'small enough' so that thermal vibrations can, together with the effective stress, move the affected part of a dislocation through that region [172].

$$\sigma^* = \sigma_0 \left(1 - \left(\frac{k_b T}{\Delta f_0 G b^3} ln\left(\frac{\dot{\varepsilon}_{ref}}{\dot{\varepsilon}^p}\right) \right)^{1/q} \right)^{1/p} \tag{20}$$

where k_b is the Boltzmann constant, T is the temperature, Δf_0, q and p are calibration parameter and $\dot{\varepsilon}_{ref}$ is typically taken as 10^6 or 10^{11}, σ_0 is the frictional stress and its value is equal to 683 MPa [160].

5.1.2.4 Hardness Prediction Model

The strengthening induced by machining operations on the material can be modeled as suggested by Eq. 21:

$$\Delta h = k_h M \alpha G b \sqrt{\rho_i} \tag{21}$$

this model has been successfully implemented via sub-routine by Ding and Shin [149]. k_h is a material constant calibrated taking into account the experimental results. The obtained value was equal to 80.18, in order to compute the resulting hardness in Vickers. In Fig. 31 is reported the prediction strategy implemented by sub-routine into the *FE* software *SFTC* Deform© in order to simulate the constitutive material behavior of the *Waspaloy* during machining operations.
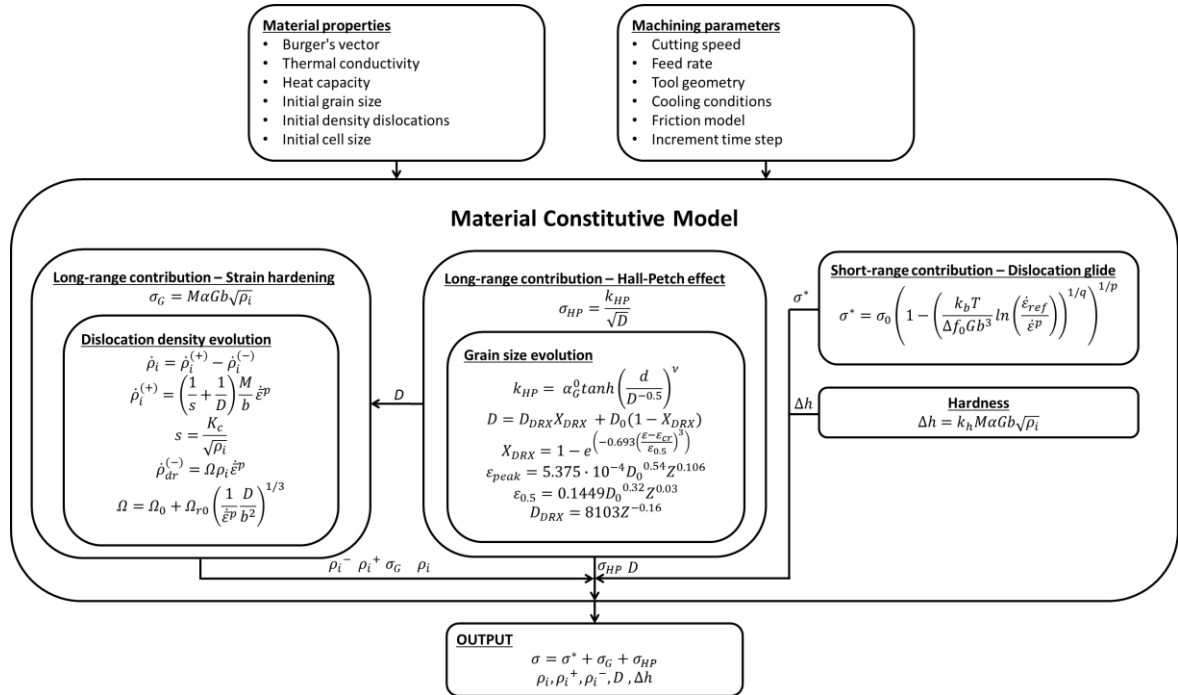
Fig. 31 Prediction strategy algorithm implemented via sub-routine to simulate the material behavior of the *Waspaloy* during machining operations.

To obtain the correct value of the numerical constants of the developed model, a fitting procedure of experimental true stress-true strain has been carried out. The calibration procedure was stopped when the error between the predicted and the experimental flow stress was minimized. The value of the constants that have been calibrated or obtained from literature are reported in Table 6.

Table 6 *Waspaloy* physics based model numerical constants identified by calibration procedure.

Numerical constants	Value	Numerical constants	Value
α	0.35	$Q_v\,[J/mol]$	220000
K_c	2.10E+01	$D_{v0}\,[m^2/s]$	5.50E-06
Ω_0	10	α^0_G	2.7
Ω_{r0}	0.18	$d\,[\mu m^{-0.5}]$	1
Δ_{f0}	0.4	v	1.40E+00
$\rho_0\,[m^{-2}]$	5.00E+11	q	1.34
p	0.27	m	3.06

5.1.3 *Waspaloy – FE Numerical Model*

A Finite Element physics-based model of the orthogonal cutting process has been developed using the commercial software SFTC Deform®. A plane-strain thermo-mechanical analysis was performed via Update-Lagrangian code with remeshing technique. The workpiece was meshed with 20000 isoparametric quadrilateral elements, with a severe mesh refining near the cutting zone, having here a mean element size of 2 µm, in order to obtain more accurate results on the worked surface and a better chip geometry. The tool has been modelled in the *FE* software as a rigid body and the geometry has been obtained studying the cutting tool using a ConScan Surface Profilometer Anton-Paar. In detail, the tool was scanned by a laser on the section transversal to the cutting direction and the obtained profile was imported into the *FE* software. The interaction between the tool and the workpiece was modelled by implementing the hybrid friction model in order to take into account both the effects of sticking and sliding at tool-chip interface. Considering the thermal aspects of the model, the global heat transfer coefficient (*h*) at the tool-workpiece interface was set equal to 10^5 kW/(m²K) according to the literature guidelines [29, 30]. Concerning the machining

tests under wet and cryogenic lubri-cooling conditions, to better simulate the two different cooling effects more considerations had to be done than dry cutting simulations. In detail, an environmental window for heat exchange have been considered and two different values for the heat transfer coefficient (h_{local}) has been set at the tool-chip interface. The value of h_{local} has been calculated using Eq. 22, according with [52].

$$h_{local} = \frac{0.20}{e^{0.35}g^{0.33}} \frac{V_f^{0.65}k_f^{0.67}c_p^{0.33}\gamma_f^{0.33}}{\nu_f^{0.32}} \qquad (22)$$

Where e is the equivalent length and g is the gravitational acceleration, while the remaining parameters are related to the cutting fluid: V_f is the velocity, k_f is the thermal conductivity, γ_f is the specific weight, ν_f is the dynamic viscosity and c_p is the specific heat capacity of the lubri-coolant fluid considered. In this specific case, the equivalent length was referred to the diameter of the nozzle.

5.2. *CP-Ti* – Plastic Flow Modeling

Focusing on the material that was considered for the second case study, a physics based model capable of simulating the flow stress behavior of *CP-Ti* is presented. All of the long range physical mechanisms that accommodate the deformation were taken into account to describe the material hardening of *CP-Ti*. Specifically, dislocation accumulation, crystal twinning, and grain refinement induced by dynamic recrystallization (*DRX*) were implemented via a user-defined *FORTRAN* subroutine in the commercial Finite Element (*FE*) software SFTC Deform®. Orthogonal cutting experiments were conducted to validate the FE model and to analyze the relative contributions of crystal twinning, dislocation accumulation, and *H-P* effect on surface hardening in cutting of *CP-Ti*. Then, the numerical model was used to comprehend the direct effects of the different process parameters over a wider range on the machined surface and to properly design the microstructural properties of the machined surface.

5.2.1 CP-Ti – Strengthening Phenomena Modeling

The proposed physics based model assumes the flow stress (σ_{pl}) as the algebraic linear sum of the contributions of the different microstructural phenomena occurring during plastic deformation processes (Eq. 23).

$$\sigma_{pl} = \sigma_G + \sigma_{TW} + \sigma_{TH} + \sigma_{HP} + \sigma_D \tag{23}$$

The term σ_G represents the resolved stress induced by dislocation accumulation and is modelled using Taylor formulation. The contributions of cell interior dislocation density strengthening and wall dislocation density strengthening are taken into account separately as shown in Eq. 24 and Eq. 25, respectively.

$$\sigma_c = \alpha_G M G b \sqrt{\rho_c} \left(\frac{\dot{\gamma}^r}{\dot{\gamma}_0}\right)^{-1/m} \tag{24}$$

$$\sigma_w = \alpha_G M G b \sqrt{\rho_w} \left(\frac{\dot{\gamma}^r}{\dot{\gamma}_0}\right)^{-1/m} \tag{25}$$

where α_G (0.25) is a proportionality constant, M is the Taylor factor (3.07 for hcp metals [173]), ρ_c and ρ_w are the cell dislocation density and the wall dislocation density, respectively, G is the thermally dependent shear modulus, m is the temperature sensitivity parameter, $\dot{\gamma}_r$ is the resolved shear strain rate, $\dot{\gamma}_0$ is the reference resolved shear strain rate and b is the Burger's vector (2.95E-10 m [174]) for hcp materials [110].

The resolved shear strain rate $\dot{\gamma}_r$ can be calculated from the von Mises strain rate ($\dot{\varepsilon}$) by using Eq. 26 [110].

$$\dot{\gamma}^r = M\dot{\varepsilon} \tag{26}$$

The cell and wall dislocation accumulation strengthening contributions are considered together using the well-known mixture law (Eq. 27) that accounts for the volume fraction of dislocation cell walls (f_{dis}) as shown in Eq. 28.

$$\sigma_G = f_{dis}\sigma_w + (1 - f_{dis})\sigma_c \tag{27}$$

$$f_{dis} = f_\infty + (f_0 - f_\infty)e^{-\frac{\gamma^r}{\tilde{\gamma}^r}} \tag{28}$$

The terms f_0 and f_∞ are the initial and the saturation volume fraction of cell walls, respectively, while γ^r is the rate of variation of f_{dis} with the resolved shear stress $\tilde{\gamma}^r$ [110].

The dislocation density evolution rates in cell interiors ($\dot{\rho}_c$) and in cell walls ($\dot{\rho}_w$) are defined by Eq. 29 and Eq. 30, respectively. Here, α^*, β^* and k_0 are the dislocation evolution rate control parameters, n is the temperature sensitivity parameter, and d is the cell size expressed in meters. This latter quantity is described by Eq. 31, where K_c is a calibration constant [110].

$$\dot{\rho}_c = \alpha^* \frac{1}{\sqrt{3}b} \sqrt{\rho_w} \dot{\gamma}^r - \beta^* \frac{6}{bd(1-f_{dis})^{1/3}} \dot{\gamma}^r - k_0 \left(\frac{\dot{\gamma}^r}{\dot{\gamma}_0}\right)^{-1/n} \rho_c \dot{\gamma}^r \tag{29}$$

$$\dot{\rho}_w = \beta^* \frac{\sqrt{3}(1-f_{dis})}{bf_{dis}} \sqrt{\rho_w} \dot{\gamma}^r - \beta^* \frac{6(1-f_{dis})^{2/3}}{bdf_{dis}} \dot{\gamma}^r - k_0 \left(\frac{\dot{\gamma}^r}{\dot{\gamma}_0}\right)^{-1/n} \rho_w \dot{\gamma}^r \tag{30}$$

$$d = \frac{K_c}{\sqrt{\rho_{tot}}} \tag{31}$$

The total dislocation density is obtained by combining the contributions of the dislocation density cell interiors (ρ_c) and the cell walls (ρ_w) by means of a mixture law that accounts for the volume fraction of dislocation cell walls (f) as shown in Eq. 32.

$$\rho_{tot} = f_{dis}\rho_w + (1 - f_{dis})\rho_c \tag{32}$$

σ_{TW} represents the twinning induced material strengthening and is given by Eq. 33. It is a function of the mean spacing of the twin lamellae (l) and the mean grain size (D) that are given by Eq. 34 [175] and Eq. 35 [72], respectively.

$$\sigma_{TW} = M\beta_{TW}Gb\left(\frac{1}{D} + \frac{1}{l}\right) \tag{33}$$

$$\frac{1}{l} = \frac{1}{2t} * \frac{f_{TW}}{1-f_{TW}} \tag{34}$$

$$D = D_{DRX}X_{DRX} + D_0(1 - X_{DRX}) \tag{35}$$

β_{TW} is a constant calibrated using tensile tests and is set as 0.9 in accordance with [175], t is the thickness of the twin lamellae (0.1 μm), f_{TW} is the twin volume fraction, D_0 is the initial grain size (31 μm), D_{DRX} is the dynamically recrystallized grain size and X_{DRX} is the volume fraction of the recrystallized grains. The terms f_{TW}, D_{DRX} and X_{DRX} are modelled by Eq. 36 [12], Eq. 37 [176] and Eq. 38 [177], respectively.

$$f_{TW} = \frac{0.417}{1+exp(-27.15*(\varepsilon-0.183))} \tag{36}$$

$$D_{DRX} = 10^{-0.102}\varepsilon^{-0.917}D_0^{0.357}Z^{-0.012} \tag{37}$$

$$X_{DRX} = 1 - exp\left(-0.00103 * Z^{-0.214} * \left(\frac{\varepsilon-\varepsilon_c}{\varepsilon_{peak}}\right)^{1.6}\right) \tag{38}$$

Where Z in Eq. 37 is the Zener-Hollomon (*Z-H*) parameter which can be written as indicated in Eq. 39 [177], and ε is the equivalent von Mises strain value. The term ε_{cr} in Eq. 38 is the peak

strain while ε_c is the critical strain for the nucleation of the recrystallized grains that is 80% of ε_{peak} (Eq. 40)[140].

$$Z = \dot{\varepsilon} \, \exp\left(218000/RT\right)$$

(39)

$$\varepsilon_{peak} = 0.002 \, Z^{0.149}$$

(40)

Where R is the universal gas constant and T is the absolute temperature.

The Peierls stress (σ_{TH}) is described by Eq. 41 and it models the thermally activated lattice friction mechanisms that obstruct dislocation motion as explained in [178].

$$\sigma_{TH} = \sigma_0 \left(\alpha_{TH} T ln \left(\frac{\dot{\varepsilon}}{\dot{\varepsilon}_{s0}} \right) \right) \left(1 - \left(-\beta_{TH} T ln \left(\frac{\dot{\varepsilon}}{\dot{\varepsilon}_0} \right) \right)^{1/q} \right)^{1/p}$$

(41)

Where σ_0 is the frictional stress, $\dot{\varepsilon}_0$ and $\dot{\varepsilon}_{s0}$ are the reference strain rates, and $\alpha_{TH}, \beta_{TH}, q$ and p are calibration constants.

σ_{HP} is the *Hall-Petch* strengthening term and is due to the pile-up of dislocations at grain boundaries leading to the activation of other slip systems in the surrounding grains [179]. The representative model of the *Hall-Petch* contribution to the flow stress is determined from Eq. 42.

$$\sigma_{HP} = \alpha_{HP} G \sqrt{b/D}$$

(42)

Where α_{HP} denotes the softening effects in material behaviour induced by sub-micron grain refinement and is captured by Eq. 43.

$$\alpha_{HP} = \alpha_{HP}^0 tanh \left(\frac{h}{D^{-0.5}} \right)^{\nu}$$

(43)

Where α_G^0, h and ν are calibration parameters [86].

Finally, σ_D represents the dislocation drag stress, that is considered to be a viscous mechanism that is due to the interaction between dislocations and lattice phonons that increase the sensitivity to the strain rate of the deformed material and is described by Eq. 44. It depends only on the strain rate and α_D is a calibration constant [180].

$$\sigma_D = \alpha_D \dot{\varepsilon}$$

(44)

The value of the constants and temperature dependent parameters used in the proposed model are obtained from literature and are reported in Table 7 and Table 8, respectively.

Table 7 *CP-Ti* physics based model numerical constants.

Numerical Constant	Value	Ref.	Numerical Constant	Value	Ref.
f_0	0.25	[110]	σ_0 [MPa]	176	[178]
f_∞	0.07	[110]	α_{TH}	0.000001	[178]
$\dot{\gamma}_0$ [s⁻¹]	100	[110]	β_{TH}	0.0000623	[178]
$\tilde{\gamma}^r$ [s⁻¹]	3.2	[110]	$\dot{\varepsilon}_0$ [s⁻¹]	4E8	[178]
α^*	0.03	[110]	$\dot{\varepsilon}_{s0}$ [s⁻¹]	1E10	[178]
β^*	0.0058	[110]	q	1.74	[178]
K_c	10	[110]	p	1	[178]
α_{HP}^0	0.4544	[86]	HV_0	79	(calibrated)
α_D	0.0045	[86]	K_{HV}	0.05	(calibrated)

Table 8 *CP-Ti* physics based model temperature dependent parameters.

Parameter	Equation	Ref.
G [MPa]	$G = 41.44 - 0.0299T$	[86]
k_0	$k_0 = 0.0000117T^{2.05}$	[110]
m	$m = 60000/T$	[110]
n	$n = 29000/T$	[110]
h	$h = 1/(0.1 + 0.0002(T - 253))$	[86]
v	$v = 2 + 0.005(T - 253)$	[86]

As suggested by Chen et al. [181], it is possible to exploit the physics based model to predict the material hardening as the sum of the isolated contributions of the different long range hardening phenomena (Eq. 45).

$$HV = HV_0 + HV_G + HV_{TW} + HV_{HP} = HV_0 + K_{HV}(\sigma_G + \sigma_{TW} + \sigma_{HP}) \tag{45}$$

Where HV_0 represents the hardness of the theoretically perfect annealed single crystal material and K_{HV} is a numerical constant. Both HV_0 and K_{HV} values were calibrated using the experimental test results and are also reported in Table 7.

5.2.2 *CP-Ti – FE Numerical Model*

In order to simulate the orthogonal cutting process, a 2D *FE* multi-physics thermo-mechanical model was implemented using SFTC Deform® aiming to predict all the main variables of industrial and scientific interest. A plane-strain Updated-Lagrangian model formulation based on the remeshing technique was used. The workpiece was modelled as a plastic body and meshed with 10000 isoparametric quadrilateral elements, while the cutting tool was modelled as a rigid body and meshed with 1000 elements. The tool was scanned by a laser non-contact Zygo Zegage Profilometer on the section transverse to the cutting direction and the obtained profile was imported as 2D geometry into the *FE* software. A higher mesh density was imposed on the tool-workpiece interface with a minimum element size of 3 μm, aiming to obtain more accurate results on the worked surface and better chip morphology. In the simulation, the workpiece was fixed while the cutting motion was assigned to the cutting tool. The thermal boundary conditions were set as suggested by Imbrogno et al. [72] for 2D orthogonal cutting. Specifically, temperatures at the bottom and left sides of the workpiece as well as on the top and right sides of the cutting tool were set equal to the room temperature, which was assumed to be 20°C. The top and right sides of the workpiece as well as the left and bottom sides of the cutting tool were allowed to exchange heat with the environment. The flow stress model was coded in *FORTRAN* and integrated into the *FE* model via a user subroutine. The boundary conditions were set and the global heat transfer coefficient was set to 10^5 kW/(m²K) according to the guidelines suggested by Arrazola et al. [29]. Furthermore, the tool-workpiece interaction was simulated by implementing a hybrid friction model at the tool-chip interface. According to the hybrid model, the sticking phenomenon is governed by a shear friction model $\tau = m\tau_0$, while the sliding effect is governed by the Coulomb friction model $\tau = \mu\sigma_0$ [182]. The friction coefficients m and μ were calibrated through a trial-and-error procedure and set to 1 and 0.7, respectively. The serration effect occurring in the machined chip was simulated using the Cockcroft and Latham (*C&L*) ductile failure model (Eq. 46) [183].

$$D = \int_0^{\varepsilon_f} \sigma^* d\varepsilon \qquad (46)$$

Where σ^* is the principal stress, ε_f is the effective strain and D is a material constant. The *C&L* material constant was also calibrated and set equal to 110 MPa, that is a slightly inferior value than the lower bound of the range suggested in [184].

5.3. *Ti6Al4V* – **Plastic Flow Modeling**

For what concerns the third case study, a physics based modeling technique able to simulate the flow stress behavior of the *Ti6Al4V* is presented. All the physical and metallurgical mechanisms that accommodate the deformation were taken into account to describe the material strengthening. In detail, dislocation accumulation dynamic, dislocation drag strengthening effect, *Peierls* softening and grain refinement induced via dynamic recrystallization (*DRX*) were implemented via user-defined *FORTRAN* subroutine in a commercial *FE* software. 3D machining experiments were conducted to validate the *FE* model and to analyze the contributions on the output variables of the different inner material phenomena that were simulated. Then, the numerical model was used to investigate the effect of the different microstructural phenomena on the machining process variables of interest and surface integrity, giving a fundamental instrument to properly design the manufacturing parameters and the functional properties of the finite product.

5.3.1 *Ti6Al4V – Deformation Mechanisms*

Severe deformation processes significantly influence the microstructural status of a general polycrystalline material. In particular, as previously explained, the machining-induced microstructural modifications, both on surface and subsurface of the worked material, can be considered as a local *SPD*, and modelled as such [27]. Under large deformation conditions, many metallurgical phenomena pertain the processed surface, modifying the macroscale behavior of the involved material. The initial microstructure can be altered taking into account the strain, strain rate and temperature configuration of the domain that is object of study [72]. These physical variables can be controlled through a proper set up of the machining parameters, moving from a slight grain deformation under gentle machining conditions, to depth and consistent inner changes on the microstructure, that can strongly affect the surface behavior of the final product [61]. Once the material grains are deformed by the processing tool action, both dislocation motion and multiplication are accommodated, resulting in a global hindrance for the material flow. Fig. 32 gives a simplified schematic representation of the surface modifications on the machined surface, here it is possible to relief that higher thermo-mechanical loads induced by severer cutting parameters result in more prominent microstructural modifications.
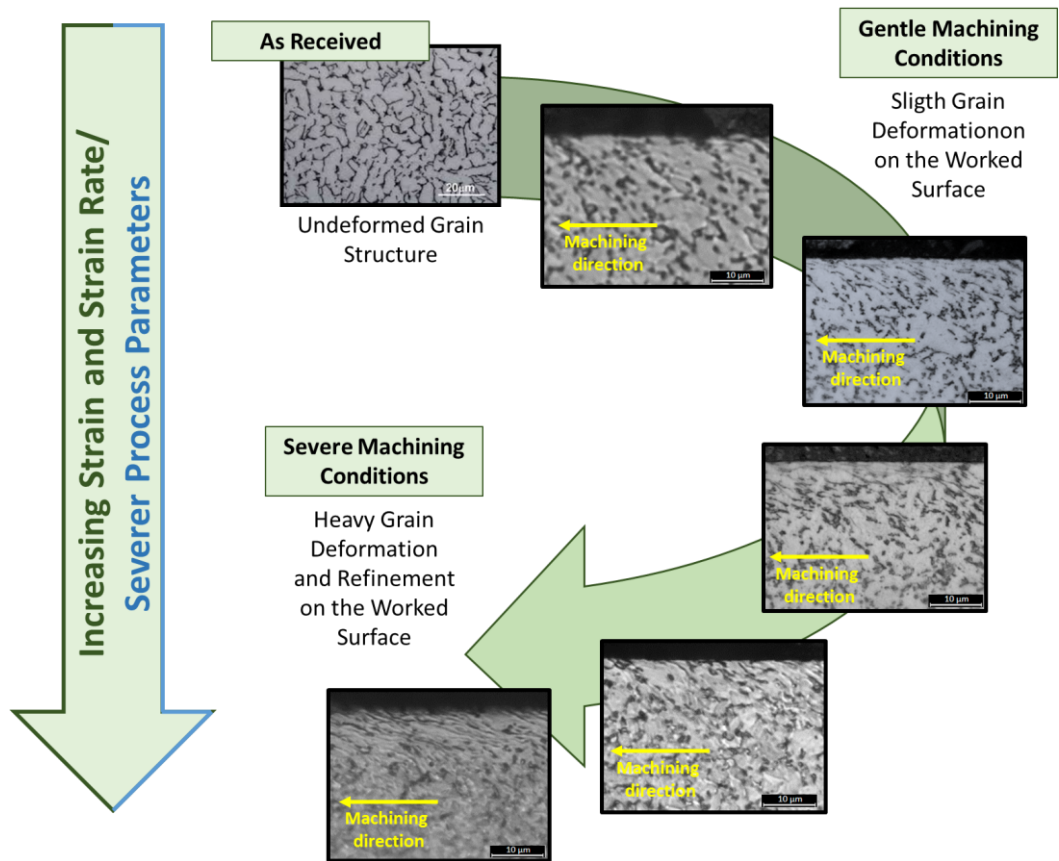
Fig. 32 Deformation mechanisms induced on *Ti6Al4V* machined surface depending on the severity of the process conditions.

The local inner modification of the processed material can lead to suitable or untoward final product performances. Such as, an accumulation of dislocation represents a substantial strengthening of the material surface due to work hardening effect [185]. On the other hand, an excessively plasticized surface can be a source of persistent slip bands, that represent one of the main causes of crack nucleation under cyclic load operative conditions [186].

The microstructural phenomena occurring during material flow, that represent the plastic strengthening evolution in terms of metallurgical modifications, can be physically discriminated into the sum of those ones related to the short-range fields (σ_{th}) and the long-range (σ_{μ}) order stress fields [187].

At low temperatures, involving also the temperature fields that are extremely lower than the environmental temperature, the main barrier for dislocation gliding are the short-range obstacles, such as the *Peierls* potential. At middle temperatures, ranging from the room temperature and around the 50% of the melting temperature, the main material flow hindrances are the long-range

obstacles, primarily represented by the self-interaction of the dislocation inside the crystal grains, the grain boundaries, and the large precipitates [188].

Another important short-range phenomenon occurring on the severely plastically deformed materials, when they are subjected to high strain rate deformation loads, as in machining, is the dislocation drag effect. This is due to the anharmonic interaction and scattering of phonons by a moving dislocation, the so-called phonon wind, that imparts a drag force on the moving dislocation, significantly increasing the material strain rate sensitivity, and contributing in a higher short-range strengthening effect (σ_D) [87, 189].

5.3.2 *Ti6Al4V – Physics based modeling*

The proposed physics based model describes the flow stress (σ_{pl}) as the algebraic sum of the different material strengthening terms and each one accounting for the contribution to the material plasticity of the main microstructural long-range and short-range phenomena that cause material strengthening or softening and occur during general materials high strain rate deformation processes.

The constitutive model is formulated considering the thermally activated short-range fields, the thermal contribution of the long-range stress field, once formulated as the sum of the strengthening effect induced by the resistance offered by grain boundaries, and dislocation forests, and, finally, the dislocation drag effect (Eq. 47).

$$\sigma_{pl} = \sigma_{th} + \sigma_{\mu} + \sigma_D = \sigma_{th} + \sigma_{HP} + \sigma_G + \sigma_D \tag{47}$$

Where σ_{th} represents the *Peierls* stress, that models the resistance of the material to plastic deformation where thermal activated mechanisms support the applied stress in moving dislocations through the lattice. σ_{HP} is the *Hall-Petch* stress and indicates the contribution of the grain size to the plastic flow and depends on the mean grain diameter, while σ_G designates the strain hardening phenomena due to the generation and accumulation of dislocations. Finally, σ_D represents the material strengthening due to the nano-scale phenomenon of dislocation drag.

5.3.2.1 Long-range Strengthening, Dislocation Accumulation Induced Stress

The interaction between the mobile and immobile dislocations is the physical basis of the strengthening of a general metal material and is usually described by the well-known Taylor equation (Eq. 48).

$$\sigma_G = \alpha_G M G b \sqrt{\rho_i} \tag{48}$$

Where α_G is a proportional constant, M is the Taylor factor, ρ_i is the density of immobile dislocations, G is the thermally dependent shear modulus expressed in GPa (Eq. 49) and b is the Burger's vector [87].

$$G = 43.6 * \left[1 - \frac{1.2(T-300)}{1923}\right] \tag{49}$$

Where T is the absolute temperature.

The dislocation density evolution is described by the two terms of Eq. 50. In detail, $\dot{\rho}_i^{(+)}$ represents the material strengthening due to the accumulation of dislocation nucleating during the large deformation process, while $\dot{\rho}_i^{(-)}$ represents the material softening due to the grain recovery effects [190].

$$\dot{\rho}_i = \dot{\rho}_i^{(+)} - \dot{\rho}_i^{(-)} \tag{50}$$

The motion of the dislocation can be obstructed by the presence of lattice obstacles causing a strengthening effect in the material flow stress. This phenomenon is described by Eq. 51 [190].

$$\dot{\rho}_i^{(+)} = \left(\frac{1}{s} + \frac{1}{D}\right) \left(\frac{M}{b}\right) \dot{\varepsilon}^p \tag{51}$$

Where $\dot{\varepsilon}$ is the equivalent plastic strain rate, D is the initial grain size and s is the crystal cell size and its evolution is described by Eq. 52 [190].

$$s = K_c / \sqrt{\rho_i} \tag{52}$$

Where K_c is a calibration constant [190].

The material softening due to the recovery effect is described by Eq. 53.

$$\dot{\rho}_i^{(-)} = \Omega \rho_i \dot{\varepsilon} \tag{53}$$

Where Ω is the recovery function [190].

5.3.2.2 Long-range Strengthening, Hall-Petch stress

The mean grain size D was predicted considering the common mixture law in order to take into account the contribution of both the grain structures previously existing into the material and the fraction of new grains generated by the dynamic recrystallization phenomenon (Eq. 54):

$$D = D_{DRX}X_{DRX} + D_0(1 - X_{DRX}) \tag{54}$$

Where D_0 is the average initial grain size (5 μm), D_{DRX} is the dynamically recrystallized grain size (Eq. 55) [191], and X_{DRX} is the volume fraction of the recrystallized grains, this latter is described by the Avrami model (Eq. 56) [192].

$$D_{DRX} = 1.847Z^{-0.13} \tag{55}$$

$$X_{DRX} = 1 - exp\left(-0.9339\left(\frac{\varepsilon - \varepsilon_{cr}}{\varepsilon_{0.5}}\right)^{0.5994}\right) \tag{56}$$

As showed by Eq. 62, the volume fraction of recrystallized grains depends on material strain (ε) and the critical strain for the nucleation of the recrystallized grains (ε_{cr}), as described by Eq. 57, $\varepsilon_{0.5}$ (Eq. 58) that is the strain that refers to the 50% of recrystallized grains fraction, and Z that is the Zener-Hollomon (*Z-H*) parameter that is described by Eq. 59 [191, 192].

$$\varepsilon_{cr} = 0.1311 * 0.0064\dot{\varepsilon}^{0.0801} * exp\left(\frac{26430}{RT}\right) \tag{57}$$

$$\varepsilon_{05} = 0.022 * \dot{\varepsilon}^{0.11146} * exp\left(\frac{30579}{RT}\right) \tag{58}$$

$$Z = \dot{\varepsilon}exp\left(\frac{341700}{RT}\right) \tag{59}$$

The *Hall-Petch* stress (σ_{HP}) depends on the mean grain size of the investigated material and represents the contribution to the material strengthening given by the grain boundaries that tends to hinder the dislocation motion. Its expression is given by Eq. 60 [87, 193].

$$\sigma_{HP} = \alpha_{HP}G\sqrt{b/D} \tag{60}$$

Where α_{HP} is a calibration constant [87].

5.3.2.3 Short range Strengthening, Peierls Stress

The σ_{th} term in Eq. 53 represents the material resistance (*Peierls* stress) to plastic deformation due to the short-range interactions where thermal activated mechanisms assist the applied stress in moving dislocations and is described by Eq. 61.

$$\sigma_{th} = \tau_0 G \left(1 - \left(\frac{k_b T}{\Delta f_0 G b^3} ln\left(\frac{\dot{\varepsilon}_{ref}}{\dot{\varepsilon}}\right) \right)^{1/q} \right)^{1/p} \tag{61}$$

Where τ_0 is the frictional shear stress, Δf_0, q and p are calibration parameter, k_b is the Boltzmann constant (1.38064852E-23 m²kg/(s²K)), T is the absolute temperature and $\dot{\varepsilon}_{ref}$ is a reference strain rate typically taken as 10^6 [39]. The *Peierls* stress plays a fundamental role below approximatively the 20% of the melting temperature of a metal inhibiting the probability of the dislocation cross-slip dynamic [87].

5.3.2.4 Short range Strengthening, Dislocation Drag Stress

The specific strengthening effect that is due to the dislocation drag phenomena is described by Eq. 62, as formulated by [87] for *Ti6Al4V* processed at extremely high cutting speeds.

$$\sigma_d = M\tau_d \left(1 - exp(-\alpha_d \dot{\varepsilon}) \right) \tag{62}$$

Where τ_d and α_d are two numerical constants representative of the investigated material.

The value of the constants used in the proposed model were obtained by a broad literature analysis [87, 187, 190, 192, 193] and are reported in Table 9.

Table 9 *Ti6Al4V* Physics based model constants values.

Numerical Constant	Value	Numerical Constant	Value
b [m]	3.47E-10	τ_0	0.025
α_G	2.3	Δf_0	0.5
M	3.07	p	0.3
ϱ_0 [m^{-2}]	1E14	q	1.8
K_c	40	$M*\tau_d$	225
Ω	38	α_d	0.001
α_{HP}	0.612		

In order to confirm the compatibility of the proposed flow stress model with the material used for the experimental tests a comparison with experimental tensile tests was carried out showing a good match (R^2 higher than 90%).

5.3.2.5 Hardness Prediction Model

The surface and subsurface hardening effect obtained downstream of the machining induced thermo-mechanical loads was modelled considering the long-range strengthening phenomena occurring during the material processing. As relieved by the employed microstructure prediction numerical model, the hardening contribution due to the dislocation accumulation on the processed surface, that is the main domain of investigation of this research, was found to be approximately constant. Moreover, exploiting the same model, on the processed surface was found a predominance of new nucleated grains (about 85%) that tends to grow extremely poor of dislocations [194]. Taking into account these results and aiming to reduce the simulations computational load, the hardness prediction model was expressed as function of the predominant strengthening effect on the processed surface, the grain refinement, as reported in Eq. 63, in accordance with [195] and [31].

$$HV = HV_0 + \frac{K_{HP}}{\sqrt{D}} \tag{63}$$

Where HV_0 and K_{HP} are numerical constants calibrated using experimental tests (209 and 393 respectively).

In Fig. 33 is reported the prediction strategy implemented by *FORTRAN* sub-routine into the *FE* software SFTC Deform® in order to simulate the constitutive material behavior of *Ti6Al4V* during machining operations.
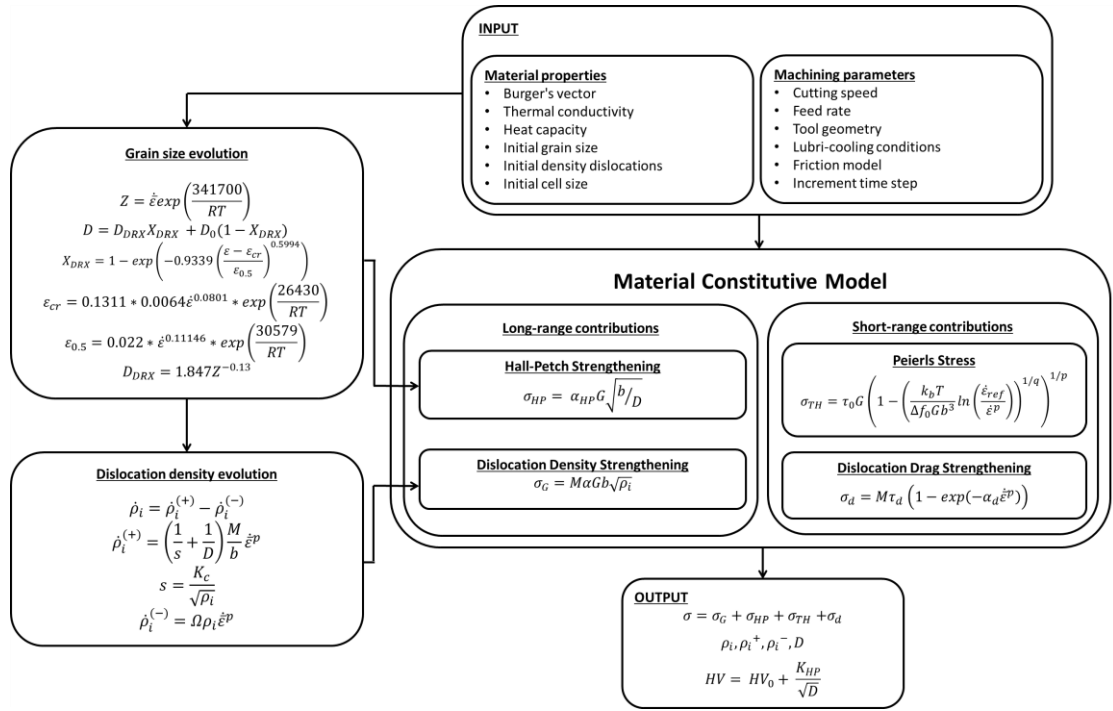
Fig. 33 Flow Chart representative of the prediction strategy implemented via sub-routine to simulate the material thermo-viscoplastic behavior and to predict the material hardness of *Ti6Al4V* during turning operations under different lubri-cooling conditions.

5.3.3 *Ti6Al4V – FE Numerical Model*

A Finite Element model of the machining process was developed using the commercial software SFTC Deform®. A 3D thermo-mechanical multiphysics analysis was performed via Update-Lagrangian code coupled with remeshing technique in order to permit a better prediction of the large deformations that involve the geometrical evolution of the processed material during the machining operations.

FE 3D modeling was based on the assumptions of a rigid machining tool (meshed into 100000 elements), while the workpiece was modelled as plastic body and divided into 200000 tetrahedral elements. The mesh density was increased at the workpiece-tool edge interface area, with a minimum element size of 7 μm, in order to have a better prediction of the surface variable induced by the machining process. In detail, the machining process has been modelled by setting up a fixed workpiece and a moving cutting tool.

The workpiece-tool thermal interaction was taken into account by setting the global heat transfer coefficient of $h=10^5$ kW/(m²K) at the interface as suggested by the specific scientific literature for the same material under machining conditions [36]. Concerning the machining tests under *HPAJ*, *MQL*, and cryogenic lubri-cooling condition, to better simulate the three different cooling effects more consideration was done than dry cutting simulations. In detail, an environmental window for heat exchange have been considered and three different values for the heat transfer coefficient (h_{local}) has been set at the tool-chip interface for each lubri-cooling condition. According with [196], the specific value of h_{local} has been calculated for each cooling condition considering the different fluids characteristics and equipment conditions, employing model represented in Eq. 64.

$$h_{local} = \frac{0.20}{e^{0.35}g^{0.33}} \frac{V_f^{0.65}k_f^{0.67}c_p^{0.33}\gamma_f^{0.33}}{v_f^{0.32}} \tag{64}$$

Where e is the equivalent length and g is the gravitational acceleration, while the remaining parameters are related to the cutting fluid: V_f is the velocity, k_f is the thermal conductivity, γ_f is the specific weight, v_f is the dynamic viscosity and c_p is the specific heat capacity of the lubri-coolant fluid considered. In this specific case, the equivalent length was referred to the diameter of the nozzle. The thermal boundary conditions were set as suggested by Umbrello et al. [195] for 3D orthogonal machining. More in detail, the temperatures at the bottom and contour sides of the workpiece as well as the top and left sides of the cutting tool were set equal to the room temperature, which was assumed to be of 20 °C. The left and the top sides of the workpiece as well as the right and bottom sides of the cutting tool were allowed to exchange heat with the environment. The overall details about the setting of the numerical model and the assignment of the boundary conditions are visible in Fig. 34a, while the tool-workpiece contact interface is in Fig. 34b.
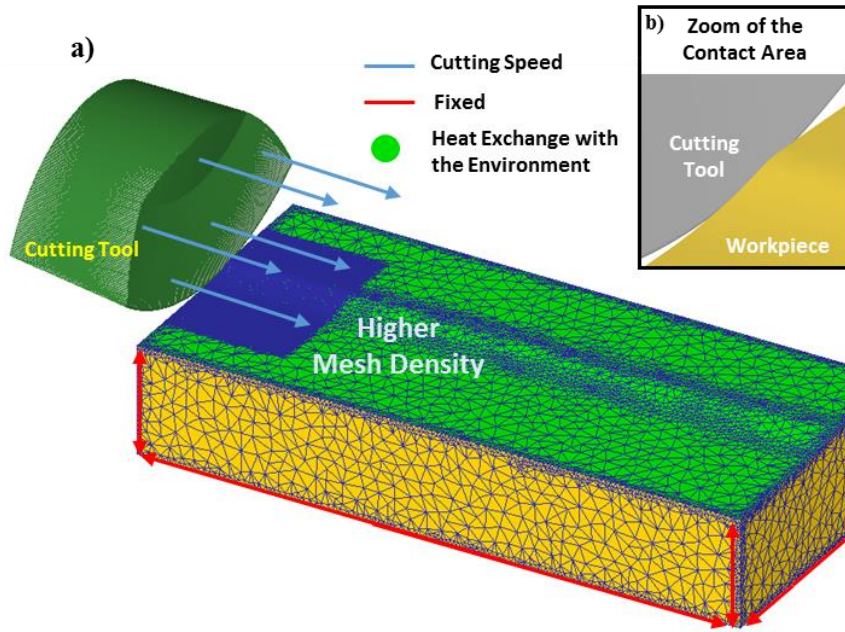
Fig. 34 Movement setup, thermal boundary conditions (a) and tool-workpiece contact area (b).

5.3.4 Friction Modeling and Calibration Strategy

The contact behavior at the tool-workpiece interface represent an aspect of fundamental importance to properly simulate a general metal machining process, aiming to obtain consistent results concerning the variables of the process that are object of investigation.

It is well documented in scientific literature that the contact normal and tangential stresses at the tool-workpiece interface shown particularly non-linear behavior. Consequently, it is possible to distinguish two fundamental region along the contact length, the sticking zone and the sliding zone [29, 197], as schematically shown in Fig. 35a. The hybrid friction model can properly simulate the intrinsic contact behavior of the two zones. The sliding zone is predominantly governed by the contact pressures imposed by the workpiece on the tool and is modelled considering the Coulomb friction behavior, while the sticking zone is characterized by a tribological behavior strongly affected by the material plastic shearing. The threshold point that represent the transition from sticking to sliding behavior is characterized by the attainment of the plastic flow stress of the material, therefore the contact behavior can be modelled in terms of friction considering Eq. 65.

$$\begin{cases} \tau = \mu p \ (\mu p < m\tau_f) \\ \tau = m\tau_0 \ (\mu p > m\tau_f) \end{cases} \tag{65}$$

The friction coefficients *m* and *μ* were found from a "Trial and Error" calibration procedure, following the flow chart that is visible in Fig. 35b, for the different lubri-cooling techniques used and the obtained values are reported in Table 10. The calibration procedure was carried out until the error obtained comparing the numerical predicted variables with the experimental results was minimized in a general good agreement with the experimental results of all the involved cutting parameters at the same lubri-cooling conditions.
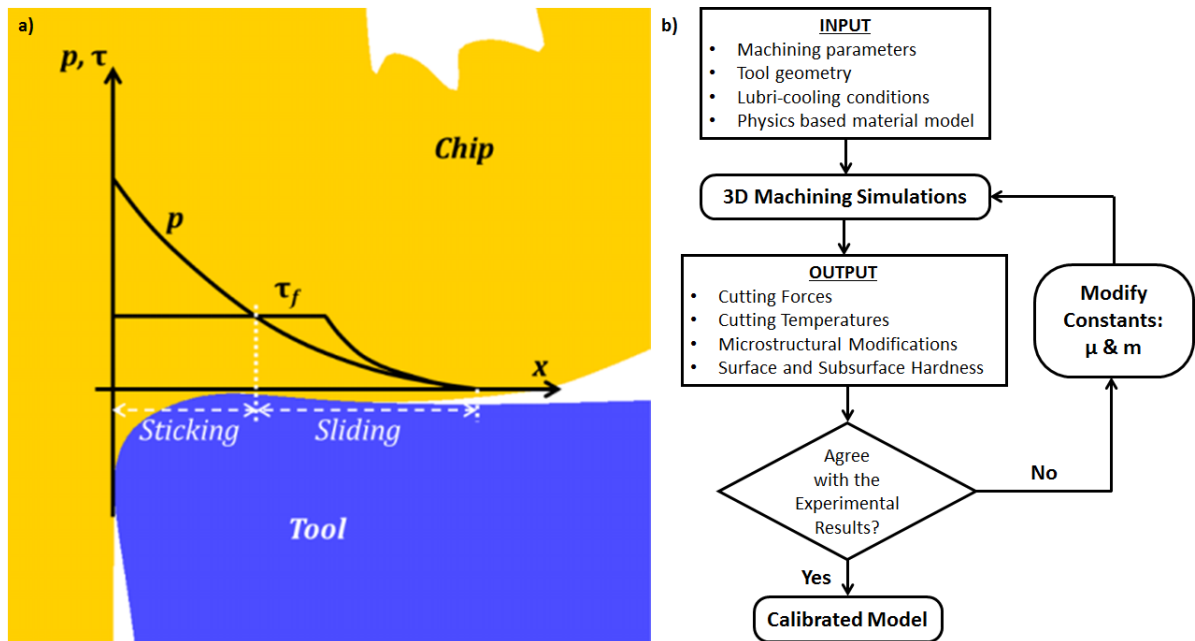
Fig. 35 Contact length at the tool-chip interface, highlighting the sticking and sliding zones.

Table 10 *Ti6Al4V* machining friction numerical constants values.

Lubri-cooling Methodology	Values of μ	Values of m
Dry	0.7	1
Cryogenic	0.6	0.9
HPAJ	0.5	0.6
MQL	0.2	0.3

According with Courbon et al. [198], for *Ti6Al4V* cryogenic lurbi-cooling conditions, the friction coefficients result to be slightly lower than the dry machining conditions, while considering *HPAJ* and *MQL* conditions, the found friction coefficients tends to reduce depending on the lubricant capabilities of the employed technique.

CHAPTER VI

In Chapter VI the validation procedure of the proposed numerical models is carried out. The procedure is faced for all the investigated materials in different paragraphs. Moreover, the analysis of the results given from the numerical results is given when they are compared with the experimental results. Finally, for each case study, a Finite Element Analysis is carries out as resulting application, exploiting the numerical models as analysis tools to investigate unexplored machining conditions.

Results and Discussion

Considering that all the approximations that have to be taken during the numerical modeling path, the validation procedure of the proposed models is the most critical part in the overall mathematical modeling process. The evaluation of the experimental results is of fundamental importance at this step. In order to carry out this procedure, the global values that can be kept from the experimental results have to be compared with the numerically predicted ones, and, so far as the error relieved from the matching of the results is acceptable, the model can be considered as validated. Thus, the validated model can be employed as an analysis tool to investigate unexplored process operative conditions, giving important preliminary information that can be considered extremely reliable for a preliminary analysis.

6.1. *Waspaloy* – Friction Calibration and *FE* Model Validation

The contact behavior model employed in machining simulations was the well-known hybrid friction model, that is particularly suited to simulate machining operations [29, 31, 32, 122]. This model depends on two coefficients (μ and m) and singularly describes the effects of sticking and sliding conditions that happen at the tool-chip interface. The aim of the calibration phase was to obtain the numerical value of the friction coefficients on varying cutting speed and feed rate. The values of the coefficients were determined through an iterative calibration strategy based on classical "trial and error" technique. Particularly, it consisted to compare the experimental cutting forces and temperatures with those predicted, modifying the friction coefficients until the error did not reach value lower than 10%. The calibration was carried out by *FE* analysis considering various cutting speeds and feed rates for each individual lubri-cooling condition and interpolating the

obtained coefficients values through Response Surface Optimization Methodology (*RSM*) using the commercial software MATLAB© curve fitting tool. These values, visible in Table 11, represent the results of the best trade-off regarding the absolute error between the considered variables (cutting forces and temperatures).

Table 11 *Waspaloy* overall error obtained at the end of the calibration procedure.

	Calibration test		Friction Coeff.		Error %			Overall Mean
	V_c [m/min]	f [mm/rev]	μ	m	F_c	F_t	T	Absolute Error
DRY	40	0.05	0.41	0.37	1.55%	11.81%	-4.18%	5.85%
	40	0.15	0.28	0.40	-1.03%	2.55%	-1.04%	1.54%
	55	0.1	0.31	0.30	6.06%	-2.46%	-0.76%	3.09%
	70	0.1	0.28	0.21	8.69%	18.80%	-5.23%	10.91%
WET	40	0.05	0.08	0.08	-0.87%	4.34%	-3.14%	2.78%
	40	0.15	0.30	0.30	-0.30%	-9.77%	3.46%	4.51%
	55	0.1	0.19	0.19	-2.63%	-0.64%	-3.91%	2.39%
	70	0.1	0.20	0.20	-0.54%	4.83%	-6.72%	4.03%
CRYOGENIC	40	0.05	0.37	0.37	9.08%	1.24%	14.29%	8.20%
	40	0.15	0.27	0.27	2.25%	-3.39%	7.33%	4.32%
	55	0.1	0.28	0.28	-2.29%	3.32%	21.96%	9.19%
	70	0.1	0.24	0.24	9.20%	8.78%	7.25%	8.41%
	Overall Mean Absolute Error				3.71%	5.99%	6.60%	

In the calibration phase, it was necessary to employ four proper case studies among the experimental test, because it is the minimum number suggested by the software that allows to develop the friction equations as a bi-linear law. The *RSM* permitted to obtain the previously reported models with very high predictive capacity, having a coefficient of determination R^2 very close to 1. Once the coefficients were calibrated, the *FE* model has been validated by comparing the experimental data with the other corresponding simulation results and the results are reported in Table 12. The predicted principal cutting forces were in a good agreement with the ones found in the experiments, with an overall average error of 4.76%. The predicted feed forces showed a total absolute error equal to 9.21%, that was higher than the principal cutting force. However, due to the very complex deformation process simulated, this specific entity of error was considered acceptable. Moreover, it is important to highlight that the tool geometry changes due to the wear. This aspect was not modelled because of higher computational time caused by a significant number

of equations involved. Therefore, the higher error in feed force was also attributed to the absence of tool wear in the finite element model, which was unavoidably present in the machining processes of super alloys [34, 86]. Concerning the temperature into the cutting zone, it was successfully predicted with an overall average error of 6.97%. This suggest that the developed thermo-mechanical simulation methodology was correctly modelled.

Table 12 *Waspaloy* overall error obtained at the end of the validation procedure.

	Validation test		Friction Coeff.		Error %			Overall Mean Absolute Error
	V_c [m/min]	f [mm/rev]	μ	m	F_c	F_t	T	
DRY	40	0.1	0.34	0.39	0.54%	-9.46%	4.13%	4.71%
	55	0.05	0.37	0.28	1.49%	7.23%	-10.38%	6.37%
	70	0.05	0.34	0.20	1.27%	31.89%	-1.91%	11.69%
WET	40	0.1	0.19	0.19	-5.57%	-5.45%	-2.07%	4.36%
	55	0.05	0.08	0.08	1.45%	12.20%	-3.46%	5.70%
	55	0.15	0.30	0.30	3.04%	-15.13%	-5.91%	8.02%
	70	0.05	0.09	0.09	1.82%	16.21%	-8.17%	8.74%
	70	0.15	0.31	0.31	9.10%	2.09%	-6.29%	5.83%
CRYOGENIC	40	0.1	0.32	0.32	18.13	7.03%	19.15%	14.77%
	55	0.05	0.33	0.33	4.44%	7.32%	12.43%	8.06%
	55	0.15	0.23	0.23	-1.26%	-11.51%	4.52%	5.76%
	70	0.05	0.29	0.29	5.09%	7.58%	-6.91%	6.53%
	70	0.15	0.19	0.19	8.68%	-5.50%	5.35%	6.51%
	Overall Absolute Mean Error				4.76%	9.21%	6.97%	

At the end of the calibration, the equations describing the trends of the friction coefficients μ and m, were defined dependent on the cutting parameters (cutting speed V_c and feed rate f), as illustrated in Eq. 66 and Eq. 67 for dry condition, Eq. 68 and Eq. 69 for wet machining conditions, Eq. 70 and Eq. 71 for cryogenic machining conditions:

$$\mu(V_c, f)_{DRY} = 0.5567 - 0.00227 * V_c - 1.213 * f \tag{66}$$

$$m(V_c, f)_{DRY} = 0.5881 - 0.00581 * V_c + 0.3048 * f \tag{67}$$

$$\mu(V_c, f)_{WET} = -0.04 + 0.000222 * V_c + 2.2 * f \tag{68}$$

$$m(V_c, f)_{WET} = -0.04 + 0.000222 * V_c + 2.2 * f \tag{69}$$

$$\mu(V_c, f)_{CRYO} = 0.5306 - 0.00278 * V_c - f \tag{70}$$

$$m(V_c, f)_{CRYO} = 0.5306 - 0.00278 * V_c - f \tag{71}$$

Taking into account the friction coefficient values showed in Table 11 and in Table 12, they show a decreasing trend with the increase of the cutting speed. Considering dry and cryogenic machining conditions, the coefficients tend to maintain slightly different value, in good agreement with the results found by Courbon et al. [198]. On the other hand, the usage of the lubri-coolant in wet conditions gravely reduces the friction effects and so the values of the coefficients.

The numerical values of the predicted variables (cutting and feed forces and temperatures) compared with the experimental ones are also reported in Fig. 36 for dry cutting condition, in Fig. 37 for wet cutting condition, and in Fig. 38 for cryogenic condition.

As previously explained, during the chip serration formation it is possible to observe both *HSSZ* and *LSSZ* due to the competition of strain hardening and thermal softening phenomena. This experimental evidence was also successfully predicted, as shown in Fig. 39, Fig. 40, and Fig. 41 in dry, wet and cryogenic machining conditions respectively. Taking into account the micrographs, the deformed region changes its morphology depending on the cutting parameters and cooling conditions. The *HSSZ* was characterized by strong deformed grains with severe modifications of substructures, while in *LSSZ* was possible to see that grains were slightly deformed or in the cases that showed a strongly serrated chip, grains were very similar to material not deformed (e.g. $V_c =$ 40 m/min, $f = 0.15$ mm/rev, under dry machining condition). The chip predicted by the numerical model showed a low strain value exactly in the *LSSZ* while higher values of plastic deformation were reached into the thin shear zone (*HSSZ*).

It is also important to highlight that the occurrence of segmentation, as well as almost continuous chip formation at varying cutting parameters and cooling conditions was predicted by the model. As suggested by Umbrello [199], a good measure of the accuracy of a machining numerical model is also suggested by its capability to correctly predict the chip formation during the machining process, this statement suggests the excellent robustness of the proposed numerical model.
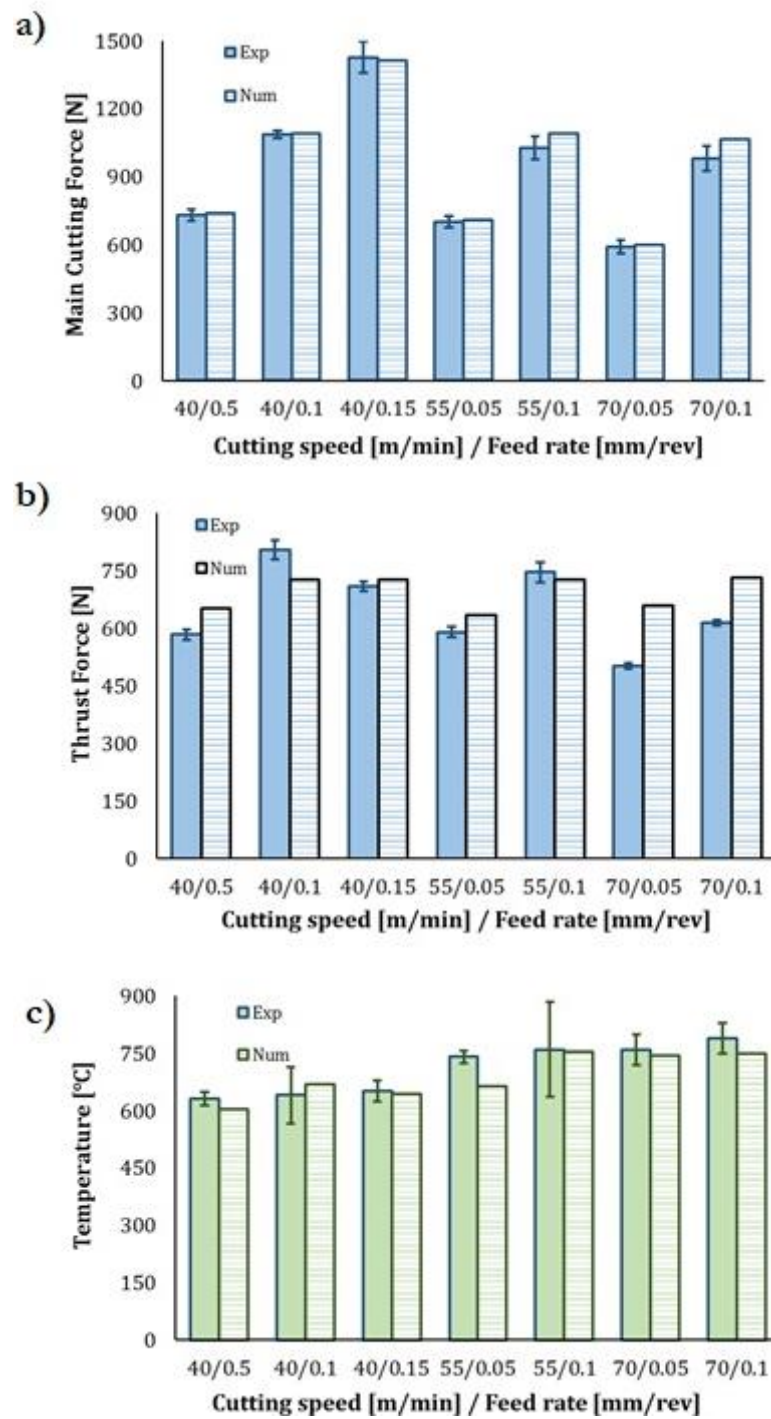
Fig. 36 Mean and variation of experimental (Exp) and numerical simulated (Num) cutting force (a), thrust force (b) and temperatures (c) for different cutting parameters in dry cutting condition.

Fig. 37 Mean and variation of experimental (Exp) and numerical simulated (Num) cutting force (a), thrust force (b) and temperatures (c) for different cutting parameters in wet cutting condition.
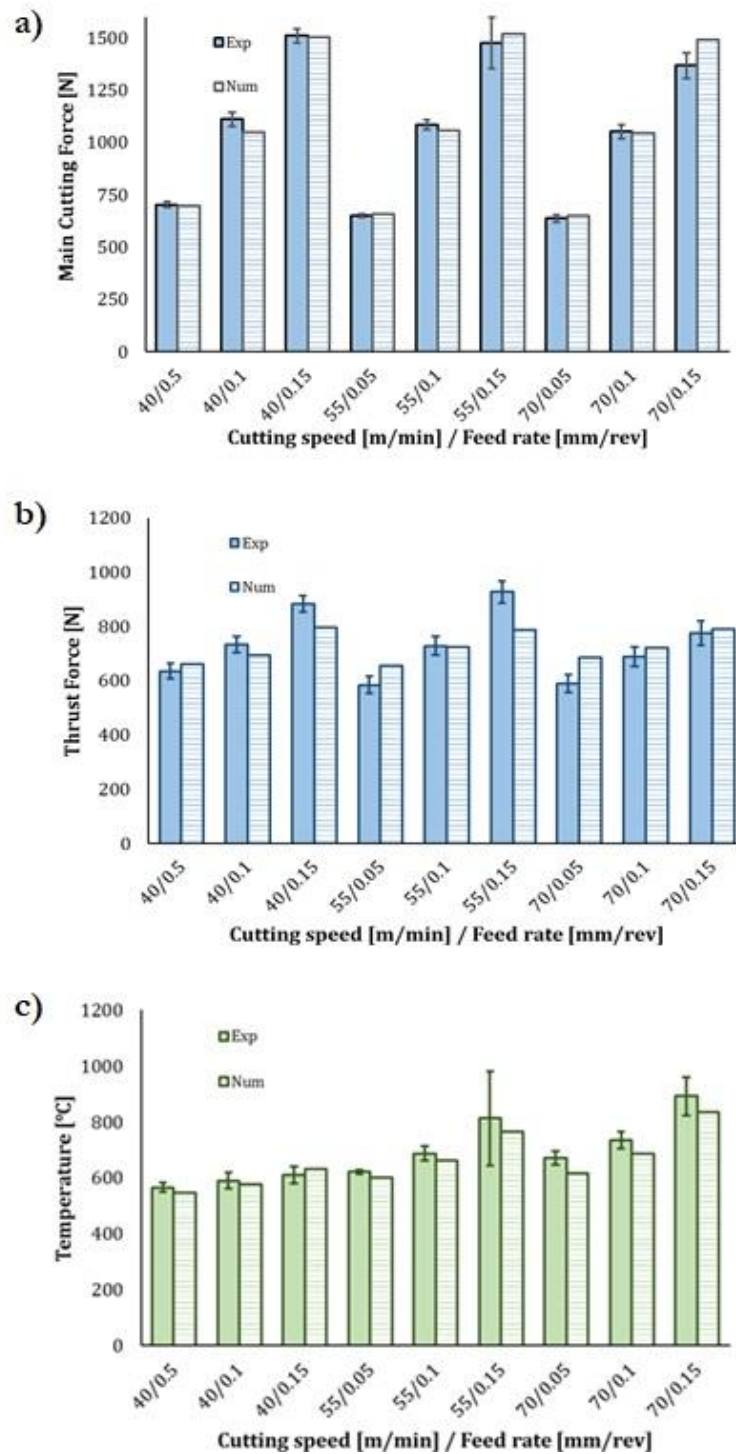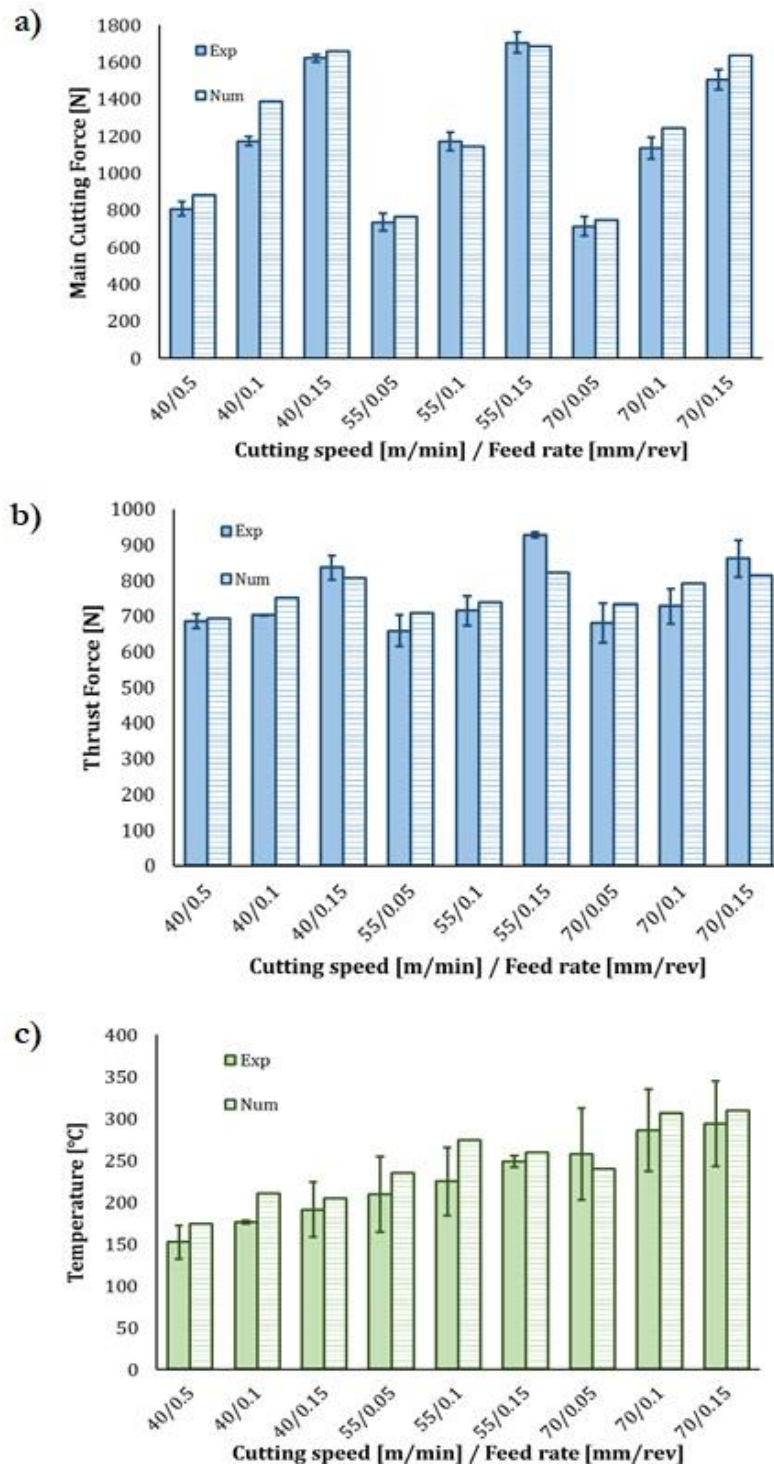
Fig. 38 Mean and variation of experimental (Exp) and numerical simulated (Num) cutting force (a), thrust force (b) and temperatures (c) for different cutting parameters in cryogenic cutting condition.

Fig. 39 Comparison between experimental and numerical predicted chip formation at different cutting parameters in dry machining condition.
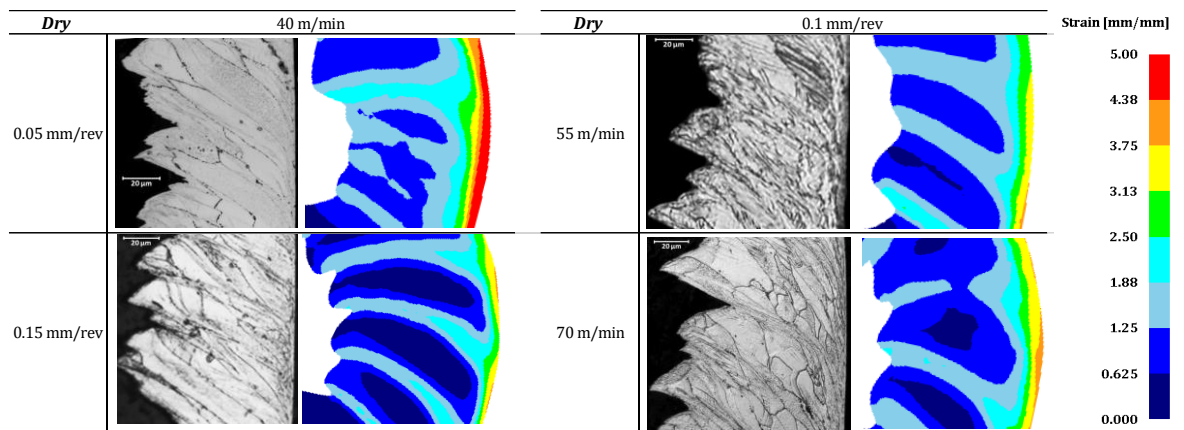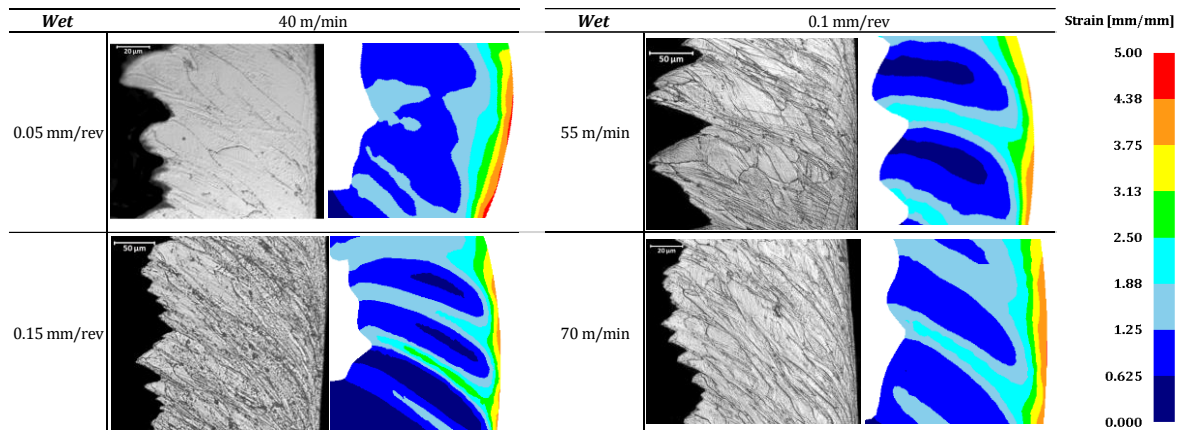

Fig. 40 Comparison between experimental and numerical predicted chip formation at different cutting parameters in wet machining condition.
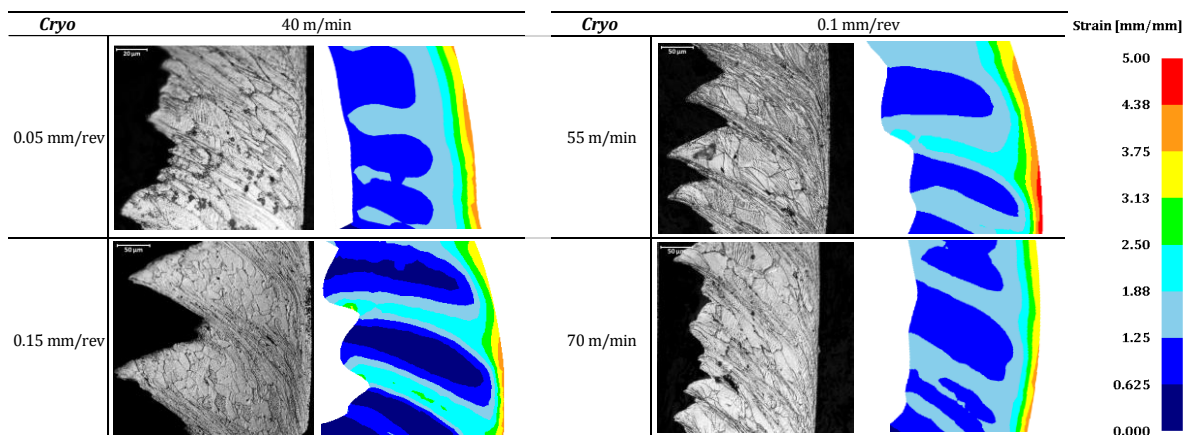

Fig. 41 Comparison between experimental and numerical predicted chip formation at different cutting parameters in cryogenic machining condition.

6.1.1 Surface integrity analysis: results and discussion

The thermo-mechanical loads induced by machining process caused substantial microstructural modifications on the worked surface [153]. The trigger and the evolution of these microstructural changes is extremely hard to be evaluated via experimental analysis, but the physics based *FE* model allows to have a complete assessment of these phenomena while they start and evolve during the machining process.

The microstructural modifications experimentally observed were deeply investigated through the numerical model once the validation phase was completed. In particular, they usually consisted of large deformed grains; but depending on the cutting speeds, feed rate and cooling conditions, further dynamic phenomena usually occurred. Beneath the worked surface, it was possible to observe plastically deformed grains characterized by diffused intersecting slip bands due to the localized shear effects. The slip bands behave as preferred site for development of highly misoriented structures [95]. These phenomena were more evident in *HSSZ* of the chip microstructure, where plastic deformation was extremely higher. Huang and Logé [93] described the metallurgical phenomena that happens into the strongly deformed region, where it was possible to relief a high concentration of dislocations arranged into cellular substructures, which generally are considered as preferred grains nucleation zones, causing *DRX* phenomena. The *FE* simulation was able to easily predict the grain size changes due to the thermo-mechanical load induced by cutting into the chip as well as on the machined surface. Although, the high refinement made difficult the experimental quantitative analysis of the microstructure into the shear band and in the ultrafine grain layers beneath the machined surface, the numerical model showed a reliable predictive capability related to these phenomena.
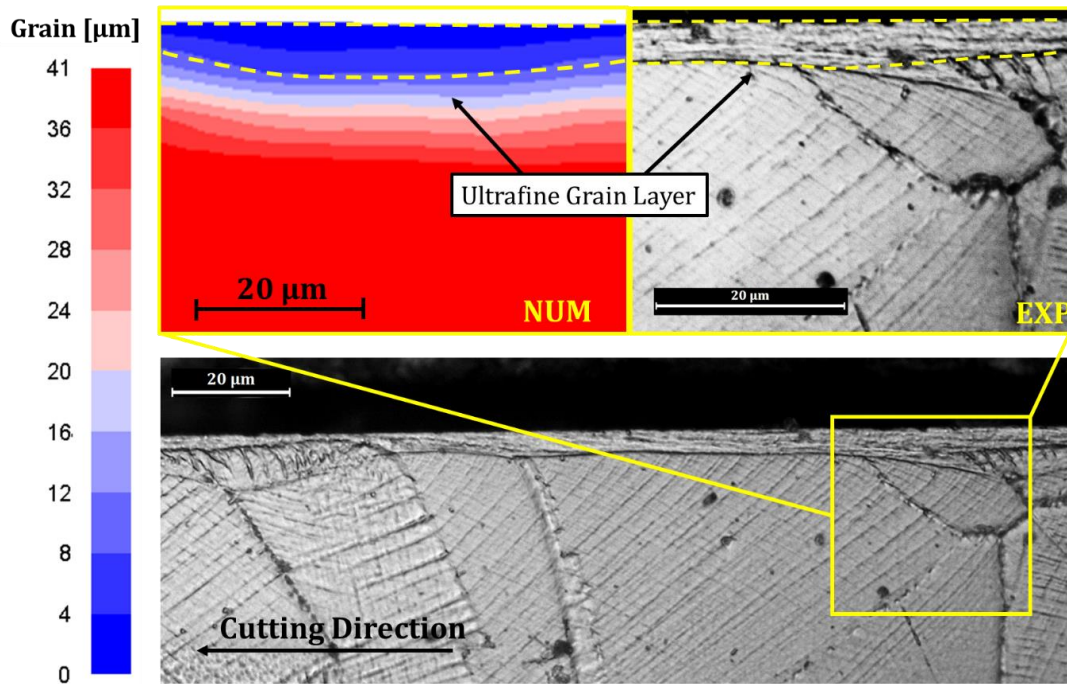
Fig. 42 Microstructure prediction and comparison with the micrographs of the machined surface (V_c = 70 m/min, f = 0.1 mm/rev, cryogenic condition).

It is important to highlight that the model was able to predict not only the new grains formation and evolution, but also the dimension of the region characterized by the severe grain refinement (altered layer thickness beneath the machined surface). In detail, taking into account Fig. 42, the optical micrograph showed a thin homogeneous layer (almost 8 μm) in which the grains were very small and thus it was difficult to quantify their dimensions.

The comparison with the numerical prediction suggested that the very thin layer was mainly characterized by very small grains with dimensions lower than 4 μm difficult to be caught by optical microscopy. Moreover, the dimension of the affected layer predicted was perfectly comparable with the experimental one; therefore, the numerical developed model was able to predict the thickness of the altered material. The very good numerical results were also obtained changing cutting parameters and cooling strategy. The reason of the grain refinement, as suggested by the numerical prediction strategy, was due to the dynamic phenomena as *DRX*. Therefore, based on the *FE* model outcomes, it is possible to claim that dynamically recrystallized grains mainly characterize the very thin layer. This latter was mainly experimentally observed in the case studied where the cutting parameters were critical (V_c = 70 m/min, f = 0.15 mm/rev) under cryogenic conditions. These ultrafine grain layers were less evident on the samples machined under dry conditions while the wet conditions totally avoided this kind of phenomenon. The presence of dynamically recrystallized grains particularly promoted by the cryogenic environment during

113

machining processes was extensively investigated and confirmed from many researchers [115, 200, 201]. Indeed, the cryogenic fluid immediately freezes the very hot material into the cutting zone totally avoiding any grain growth and recovery effect. The physics based model showed the ultrafine grain layer formation due to *DRX* only when the cryogenic machining was simulated. Indeed, the thermal conditions that modelled the presence of liquid nitrogen were set through environmental windows into the cutting zone, while to simulate the dry conditions, only the exchange heat with the environment was used due to the lack of lubri-coolants. Therefore, it is clear that the thermal conditions also play an important role in inducing microstructural changes. The capability of the cryogenic machining to promote the *DRX* and avoid the recovery phenomena is well assessed by the scientific community [202] and this aspect is well represented by the *FE* model. Therefore, the developed simulation methodology can be effectively used to comprehend the reason of the thin layer formation, its composition, the microstructure size and its evolution depending on the cutting parameters and cooling conditions.

In Fig. 43 is reported the comparison between the numerical and experimental microstructural alteration due to the cutting operation within the chip. As previously mentioned, the serrated chip was characterized by two regions with different microstructural features. The experimental observation did not permit to deeply know the metallurgical phenomena that occurred into the *HSSZ* as well as their evolution at vary thermo-mechanical loads. However, the *FE* developed strategy allowed to study the occurrence of the new microstructures. As showed by the simulated chip formation, the grain size inside the *HSSZ* was finer than the surrounded one (usually slightly deformed) and the dynamic phenomenon that leads to the grain refinement was the *DRX* due to the combination of high temperature and plastic deformation. The new microstructure consisted of sub-micrometer grains according with the results reported by Ni and Alpas [30], Fernandez-Zelaia [60] and Ravi Shankar [61, 62]. Moreover, the width of the deformed and undeformed zones were clearly distinguishable thanks to the grain size changes (Fig. 43) and were completely comparable with the optical micrograph.
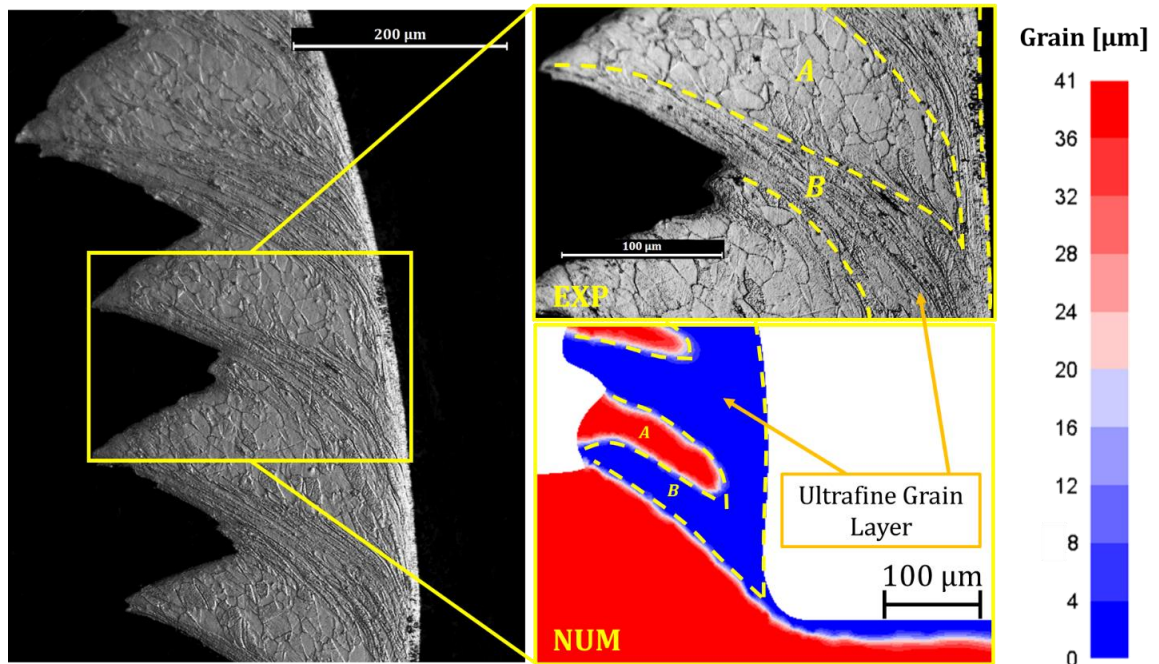
Fig. 43 Microstructure prediction and comparison with the micrographs of the machined chip (V_c = 70 m/min, f = 0.1 mm/rev, cryogenic condition).

It is well known that the tool action on the machined surface typically causes material changes and consequently modification of the material properties. Generally, large plastic deformations lead to work hardening phenomenon that is usually experimentally appreciated by hardness measurements. The hardness variation is commonly attributed by the grain size changes and is analytically described by the *Hall-Petch* equation [203]. However, the regions beneath the machined surface, where the measured hardness showed higher variations, were wider than the layers characterized by *DRX* (Fig. 44). These results suggest that the *DRX* was not the main responsible of hardness increasing, indeed below the *DRX* layer the grains showed regions subjected to substantial slip activities that means increment of dislocation density [151]. Consequently, the numerical model was useful to investigate the role of dislocations in relation with the hardening and recovery phenomena. It is important to highlight that the dislocation density computed on sub-surface were more concentrated in the region experimentally characterized by slip bands. Moreover, the accumulation of dislocations led to hardness variation as predicted by the model, and the results are in agreement with the measurements (Fig. 44).
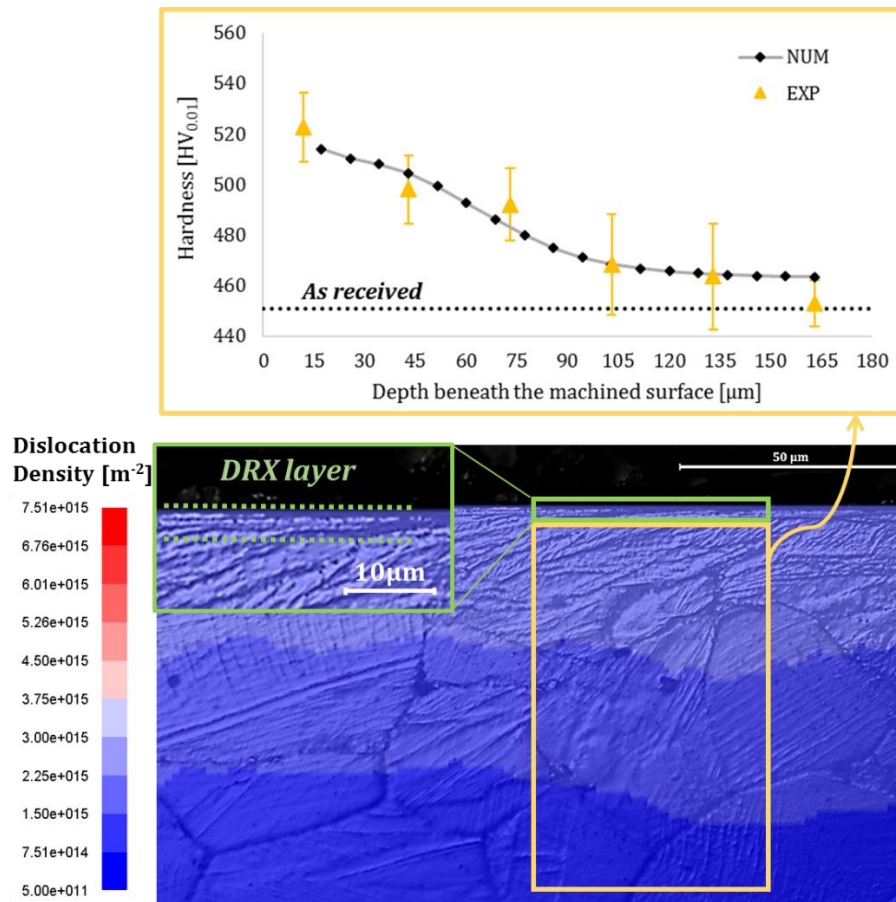
Fig. 44 Dislocation concentration beneath the worked surface and consequent hardness variation, V_c = 40 m/min – f = 0.15 mm/rev – cryogenic (the dislocation density prediction is superposed to the optical micrograph).

The overall comparison between the experimental and numerical hardness value is showed by Fig. 45. The data were collected in all the analyzed cases on the worked subsurface starting from a depth of 15 μm. It is possible to observe (Fig. 45) that the developed model was able to predict the hardness at varying cutting speed, feed rate and cooling conditions. This latter also supported the right modeling strategy used to take into account the cooling phenomenon. The maximum average error between the numerical and experimental results did not exceed the 5%.

Moreover, as suggested by Fig. 46, the robustness of the model was also confirmed by the hardness prediction through the entire affected layer. This very good result is highlighted in Fig. 46a, Fig. 46b and Fig. 46c at various cooling conditions. It is important to point out that the good prediction of the hardness variation by the *FE* model permitted to better evaluate the affected layer thickness.
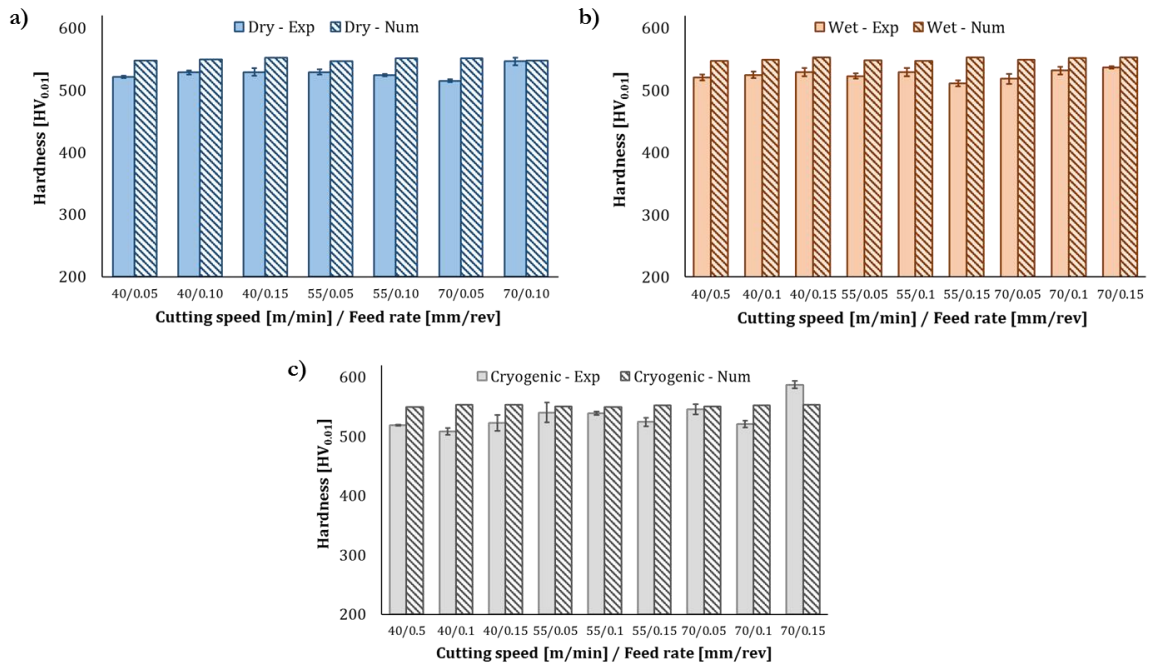
Fig. 45 Mean and variation of experimental (Exp) and numerical simulated (Num) hardness beneath the worked surface in dry (a), wet (b) and cryogenic (c) machining conditions.
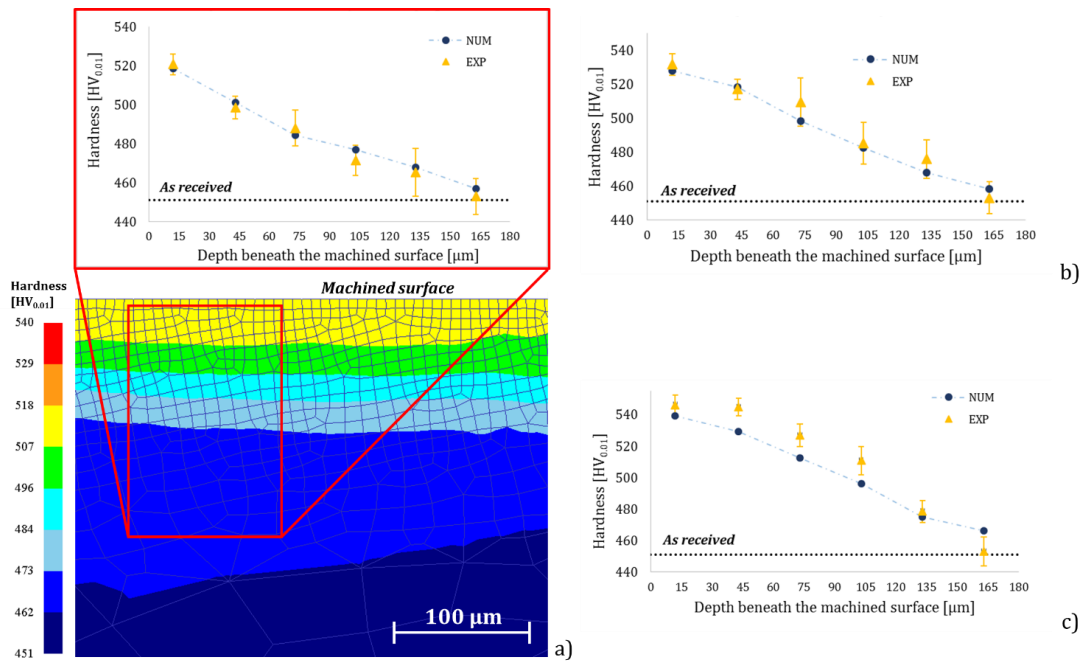

Fig. 46 Comparison between the experimental (EXP) and numerical simulated (NUM) hardness through the affected layer in cryogenic (a), wet (b) and dry (c) cooling conditions at $V_c = 70$ m/min $- f = 0.1$ mm/rev.

6.1.2 Finite Element Analysis (FEA)

The *FE* simulation allowed to predict the cutting forces and temperature as well as to identify the grain size modification range, their related formation mechanism, the dislocations accumulation and their effect on the hardness beneath the machined surface. In detail, as previously mentioned in paragraph 6, the combination of higher cutting parameters (V_c=70 m/min, f=0.15 mm/rev) and the cryogenic fluids led to formation of ultrafine grain layers. These phenomena were less evident on the samples machined under dry conditions while they were never observed under wet machining conditions. The reliability of the model in predicting fundamental variables (cutting forces and temperatures) as well as metallurgical changes were validated; therefore, the developed model can be used to explore the effects of further cutting parameters on the machined surface. Generally, the increment of the cutting speed permits to reduce the manufacturing time leading to an improvement of the overall production, thanks to the developed model it is possible to anticipate the cutting forces, temperatures and surface integrity and thus the global feasibility of the process parameters selected. Therefore, the authors decided to perform a Finite Element Analysis (*FEA*) increasing the cutting speed to 85 m/min keeping the feed rate at two levels (0.05 mm/rev and 0.1 mm/rev) and considering the same cooling strategies (dry, wet and cryogenic). It is important to highlight that the feed rate equal to 0.15 mm/rev was not included in the analysis since the experimental results showed intense tool wear and a catastrophic tool failure during dry tests at the studied cutting speeds (55 m/min and 70 m/min) [34]. As showed in Fig. 47a, Fig. 47b and Fig. 47c, the feed rate and the cooling conditions affect the cutting forces and the temperature.

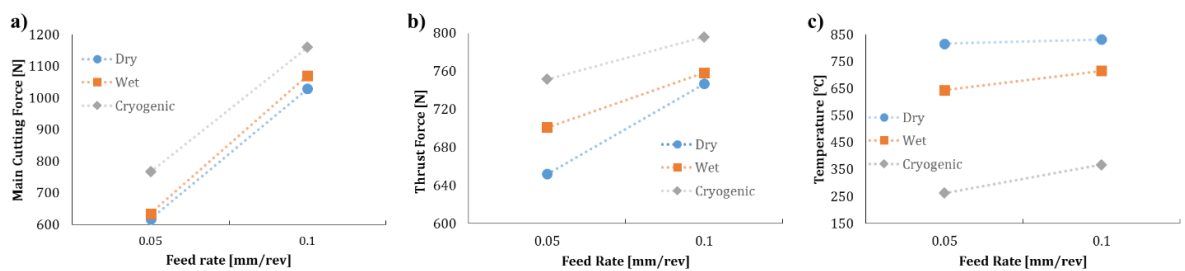Fig. 47 (a) Main Cutting Force; (b) Thrust Force; (c) Temperature at cutting speed of 85 m/min on varying cutting conditions.

Generally, increasing the cutting speed from 70 m/min to 85 m/min with fixed feed rate of 0.05 mm/rev the main cutting and thrust forces slightly decrease of 3% while at feed rate of 0.1 mm/rev the decrease is equal to 5%. It is possible to claim that the cutting forces variation is almost

negligible and the trend reached a steady state. However, at high cutting speed (85 m/min) the difference is still evident at different feed rate and cooling conditions. The lower temperatures produced by the cryogenic fluid led to higher cutting and thrust forces compared to wet and dry conditions. Concerning the metallurgical phenomena, the higher cutting speed led to smaller grains formation due to dynamic recrystallization, indeed the combination of thermo-mechanical load triggered the nucleation and formation of new grains. Regardless the cooling conditions, the formation of larger recrystallized grains induced by a machining operation with cutting speed of 85 m/min respect to the ones obtained at cutting speed of 70 m/min was mainly due to the higher cutting temperatures. On the other hand, a different situation appeared taking into account the dislocations accumulation and thus the hardness on the machined surface.
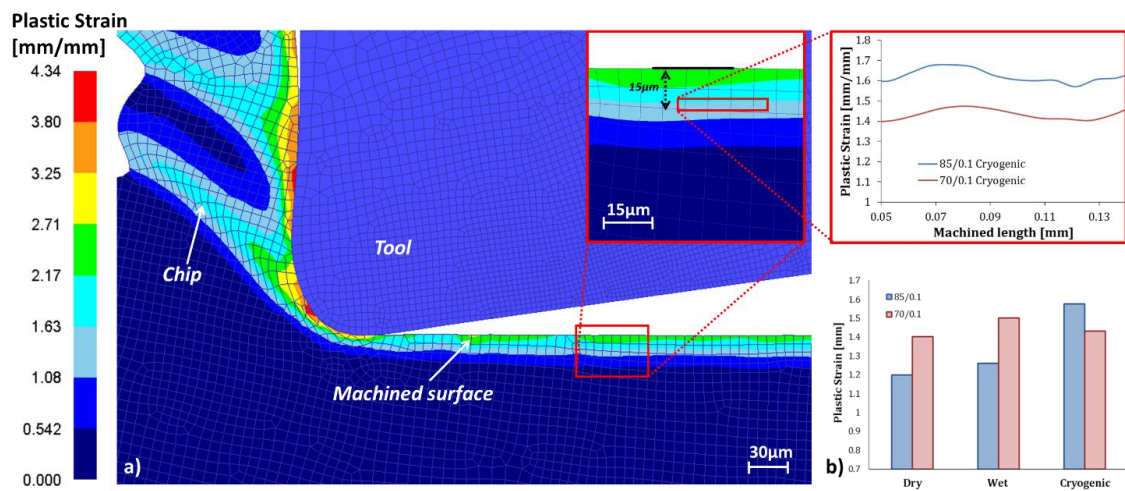

Fig. 48 Predicted plastic strain at (a) cutting speed of 85m/min, feed rate of 0.1 mm/rev under cryogenic conditions; (b) average value of plastic deformation at different cooling conditions.
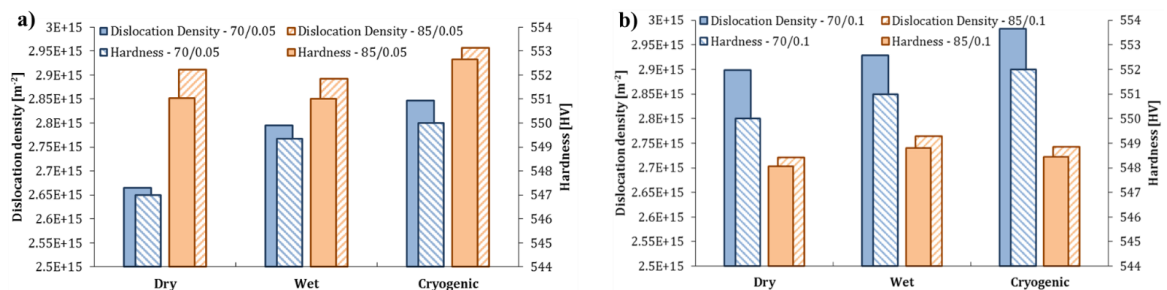

Fig. 49 Computed average value of dislocation density and hardness on varying lubri-cooling conditions at cutting speed of 70 m/min and 85 m/min, (a) feed rate of 0.05 mm/rev and (b) 0.1 mm/rev.

Focusing at 15 µm beneath the machined surface, then excluding the recrystallized region, the dislocations density, the plastic deformation and subsequently the hardness were computed depending on the cutting speed (70 m/min, 85 m/min), feed rate (0.05 mm/rev. 0.1 mm/rev) and cooling strategy (dry, wet and cryogenic) (Fig. 48 and Fig. 49).

Considering the feed rate of 0.05 mm/rev, the increase of the cutting speed from 70 m/min to 85 m/min led to the increase of plastic deformations and temperature on the machine surface. However, the plastic deformation had a predominant effect promoting the dislocations accumulation and thus the raise of hardness. As showed by Fig. 49a, the material exhibited a strain hardening behavior under dry, wet and cryogenic. On the contrary, at higher feed rate (0.1 mm/rev), the increase of cutting speed led to an increase of cutting temperature and consequently a lower accumulation of plastic deformation (dry and wet conditions) causing a decrease of dislocation densities and thus of hardness, as visible in Fig. 48a and Fig. 49b. Taking into account dry and wet conditions, it is possible to observe that despite the plastic strain at higher cutting speed was lower, the cryogenic machining still permitted to reach higher plastic deformations. However, the difference of temperature at feed rate of 0.1 mm/rev was more significant (60 °C) than the one observed at lower feed rate (23 °C), therefore the higher thermal gradient led to a predominant thermal softening effect against the higher plastic strain under cryogenic conditions. Moreover, the higher temperature difference under cryogenic machining led to a lower accumulation of dislocations due to the predominance of recovery (Fig. 49b). This analysis highlights that machining *Waspaloy* with cutting speed higher than 70 m/min does not permit to achieve higher hardness values beneath the machined surface without correctly setting the feed rate parameter. The *FEA* showed an upper limit in improving the surface integrity in terms of hardness, in fact, as showed by Fig. 49b, the cooling strategy did not significantly affect the dislocation density and thus the hardness, but the most relevant variation was due to the cutting speed once the feed rate exceeded the value of 0.05 mm/rev.

6.2. *CP-Ti – FE* Model Validation, Results and Discussion

To validate the *FE* model, the numerical results of cutting forces, chip morphology, deformation and twinning affected layers, and the surface and sub-surface microhardness were compared with those experimentally observed.

Analysing the experimental results, it is evident that the measured forces tend to decrease slightly with increasing cutting speed (Fig. 50), which is attributed to the higher heat generation rate and

consequent material flow softening. Also, as expected, with increasing feed rate, higher force values are observed. As visible in Fig. 50, the trends of the predicted forces are similar to the experimentally observed trends with less than 4% of error for F_c and around 8% of error for F_t.
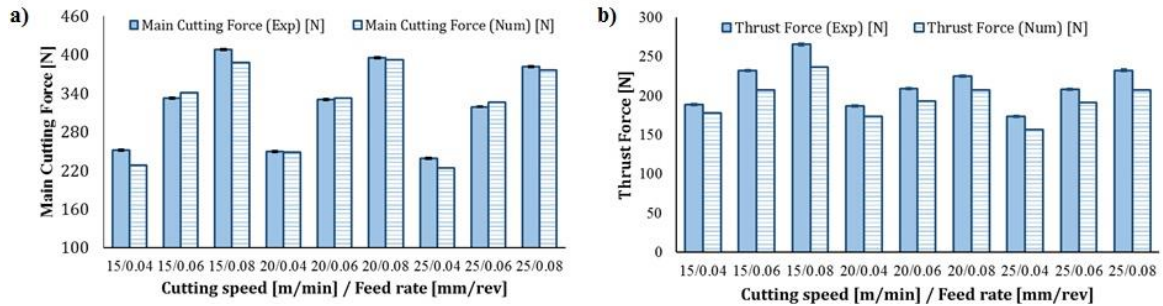

Fig. 50 Comparison between the experimentally measured (Exp) and numerically simulated (Num), (a) Main Cutting Forces and (b) Thrust Forces.

The predicted F_t shows a larger total absolute error than the cutting force (F_c). However, due to the very complex deformation process simulated, this specific entity of error was considered acceptable in accordance with [72, 86]. Moreover, it is important to highlight that during machining, the tool geometry changes due to wear. This aspect was not modelled because of the higher computational time involved and because it can influence the measured values of the thrust forces [204]. Therefore, the slightly higher error in thrust force was also attributed to the absence of tool wear in the FE model, which is unavoidably present, albeit in small amounts, in all metal machining processes.

Fig. 51a shows the comparison of simulated and experimentally evaluated chip geometry. In particular, it is clearly visible that the major features in the experimentally obtained chip are captured by the numerical simulation. Furthermore, it can be seen that proper calibration of the *C&L* constant allows prediction of the evolution of chip serration. In particular, the damage field tends to be localized in a fixed band in the primary shear zone where the shear stress reaches large values [205]. Due to this effect, two different zones are distinguishable in the chip shape (Fig. 51), namely the Low Shear Strain Zone (*LSSZ*) and the High Shear Strain Zone (*HSSZ*) [72]. The LSSZ is largely characterized by material rigid motion, with restrained deformation and consequent reduced stretching of the grains in this region. On the contrary, due to the more intense imposed deformation, the *HSSZ* shows highly deformed grains concentrated into a thin but highly strained shear band, which acts as plastic hinge and promotes the formation of the chip segments [206, 207]. In the *HSSZ*, an intense dislocation accumulation phenomenon is expected to occur as correctly predicted by the numerical model (Fig. 51b).
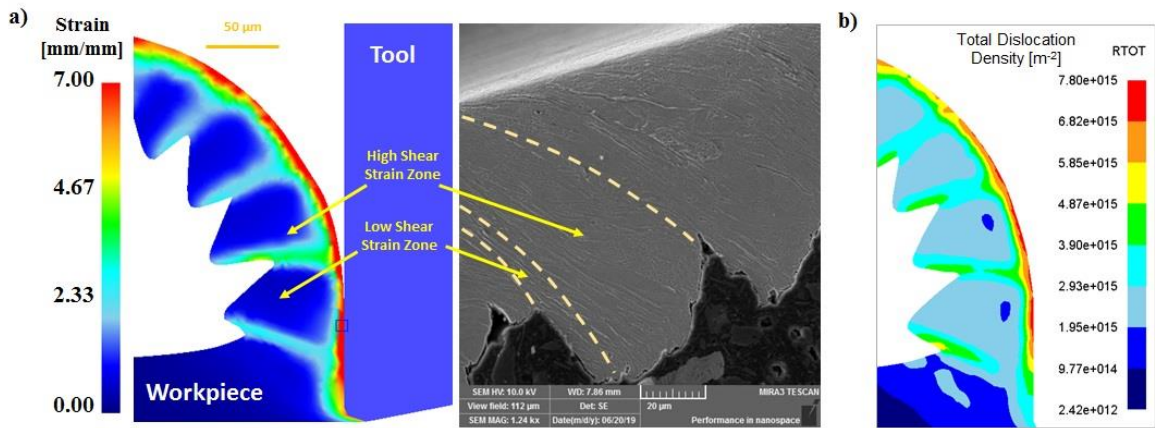
Fig. 51 Comparison between machined chip SEM micrograph and (a) numerically predicted geometry, and (b) dislocation accumulation concentration within the chip plastic shear band at 20 m/min and 0.06 mm/rev.

The chip topography prediction in terms of peak, valley, and pitch size is reported in Fig. 52a and the mean absolute error in measurements are found to be 11%, 8% and 14%, respectively (Fig. 52b, Fig. 52c, and Fig. 52d). These errors are consistent with commonly accepted ranges in the scientific literature, as reported for example in [72, 86].

Considering the relatively small thermo-mechanical loads induced by the machining parameters used in the experimental study, no significant *DRX* phenomenon is expected as shown through subsequent critical strain analysis later in the paper [208]. Thus, the only microstructural modifications detected in the micrographs are an intense grain deformation and twin band generation within the worked surface [209]. The grains are severely deformed near the machined surface, as seen in the *SEM* micrograph in Fig. 53a, and the grain deformation tends to decrease along the depth beneath the machined surface. For all the cases investigated, the thickness of the deformed layer discerned from micrographs is comparable to the predicted strain affected layer (Fig. 53b).

Moreover, analysing the machined surface micrographs, and referring to only the twinned grains, it is possible to identify a twin bands affected layer with a thickness of nearly 100 μm, which is predicted by the *FE* model with a mean absolute error of 4%, as clearly visible in Fig. 54. The presence of this layer can positively affect the machined surface and sub-surface behaviour, providing a particularly functional combination of ductility and strength [82]. This feature enhances the surface mechanical properties, with a particular regard to the wear resistance of machined implants [210, 211].
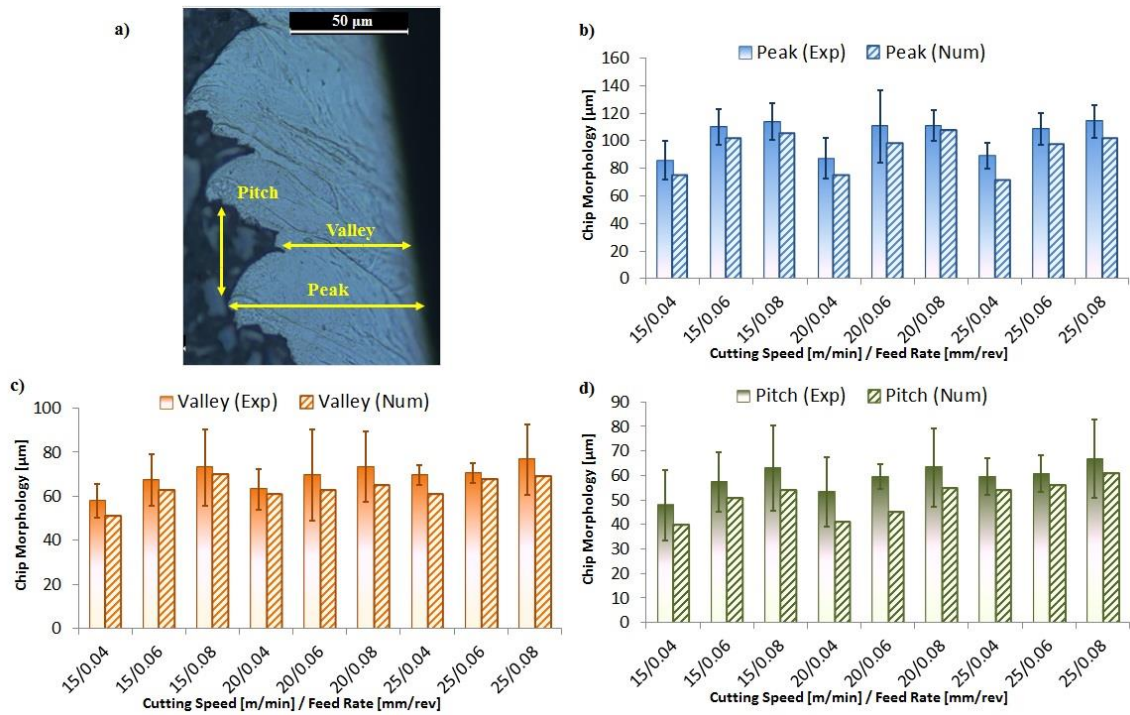
Fig. 52 Chip topography measurement (a) index at 20 m/min and 0.06 mm/rev and comparison between experimentally relieved and numerically predicted machined chip features in terms of (b) peak height, (c) valley depth and (d) pitch.
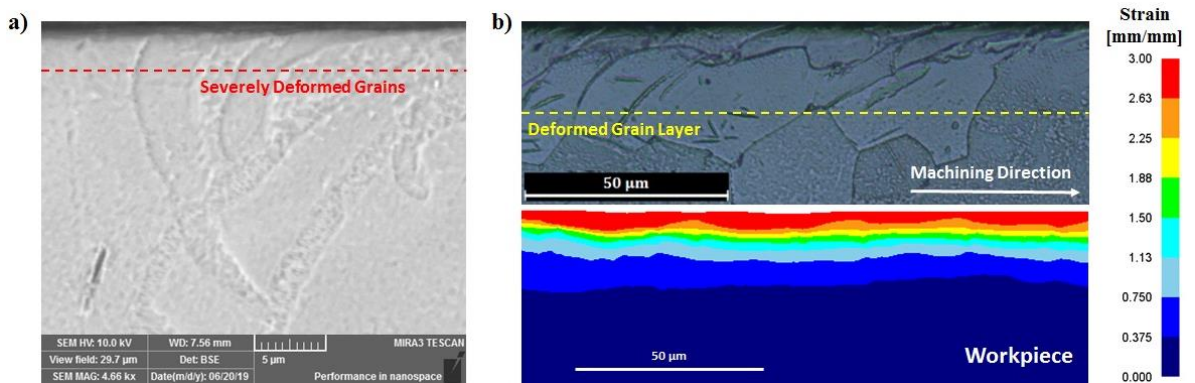
Fig. 53 Severely deformed grains near the machined surface, (a) *SEM* micrograph, and (b) comparison between experimentally measured and numerically predicted grain deformed layer (25 m/min and 0.08 mm/rev).
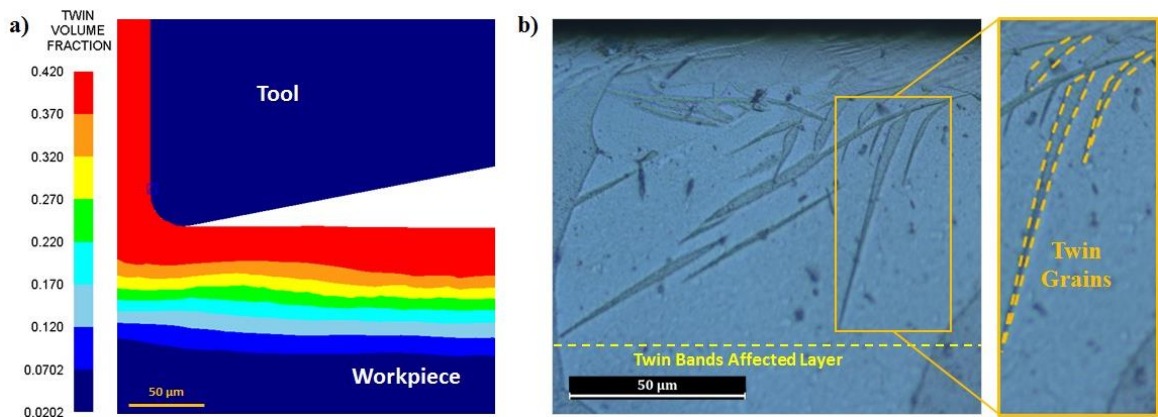
Fig. 54 Comparison of twinning affected layer thickness beneath the machined surface at 20 m/min and 0.06 mm/rev. The layers were numerically predicted in terms of (a) twin volume fraction and (b) experimentally relieved via optical microscope.

The proposed numerical model enables relating the strengthening effects occurring in the machined surface with the surface and sub-surface microhardness. Fig. 55 reports the comparison of the experimentally measured microhardness values with those predicted numerically, demonstrating good agreement all along the hardened layer, as further support of the proper validation of the modeling strategy.
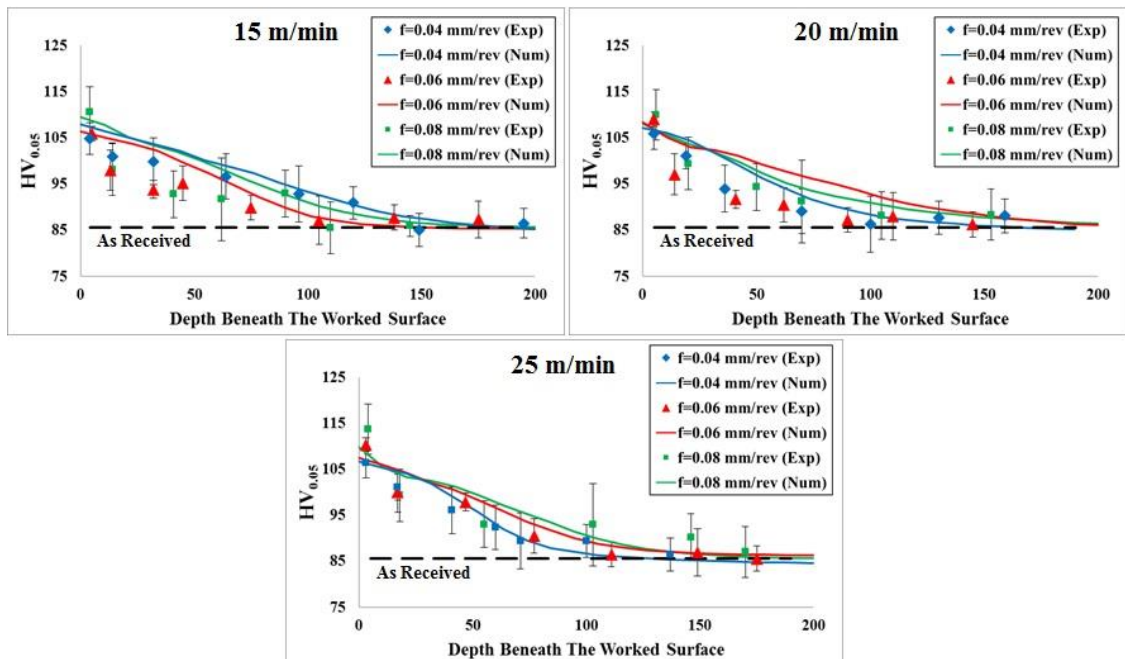
Fig. 55 Comparison between the experimentally measured (Exp) and numerically simulated (Num) workpiece microhardness on the machined surface and along the affected layer.

Considering the individual terms in Eq. 45, it is possible to separately evaluate the different strengthening phenomena and to deconvolute their separate contributions, thus allowing assessment of their significance to the overall material strengthening in the machined sub-surface as shown in Fig. 56.
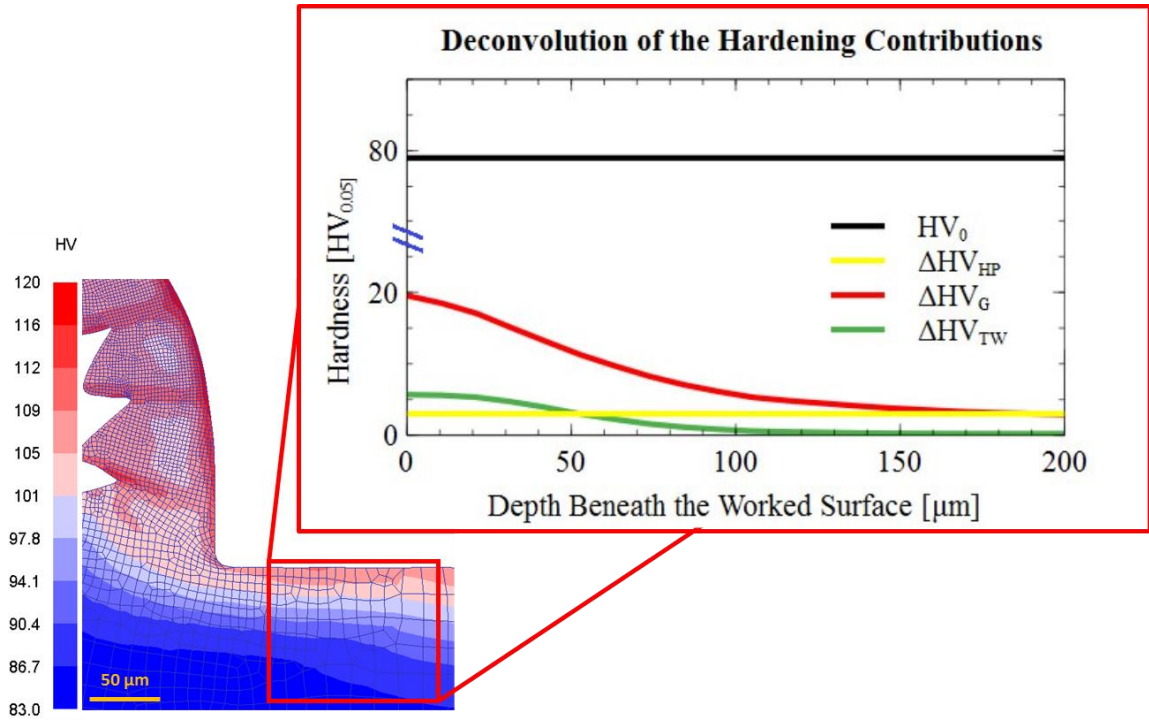
Fig. 56 Deconvolution of the different contributions of the single metallurgical strengthening phenomena to the global surface and sub-surface workpiece hardening (20 m/min and 0.04 mm/rev).

Thus, it is possible to find that on the machined surface the dislocation accumulation induced hardening phenomenon predominates. Besides, the twinning induced contribution is found to be significant as well, with an estimated value of around 25% of the dislocation contribution to the overall hardening increase. Moreover, it is worth noticing that only a slight temperature increase is visible at the tool-workpiece interface, primarily because of the gentle process conditions that are typical of micro cutting [212].

As visible in Fig. 57, even under the most severe cutting conditions, the critical strain required to trigger the *DRX* phenomena is always higher than the equivalent strain reached on the machined surface at each step of cutting. This is due to the relatively low cutting temperatures. Therefore, even when the cutting tool approaches the investigated area of the workpiece, inducing the highest deformation on the machined surface, the plastic strain is always too low to trigger any *DRX*

induced grain refinement, resulting in a constant contribution of *H-P* hardening all along the depth beneath the machined surface.
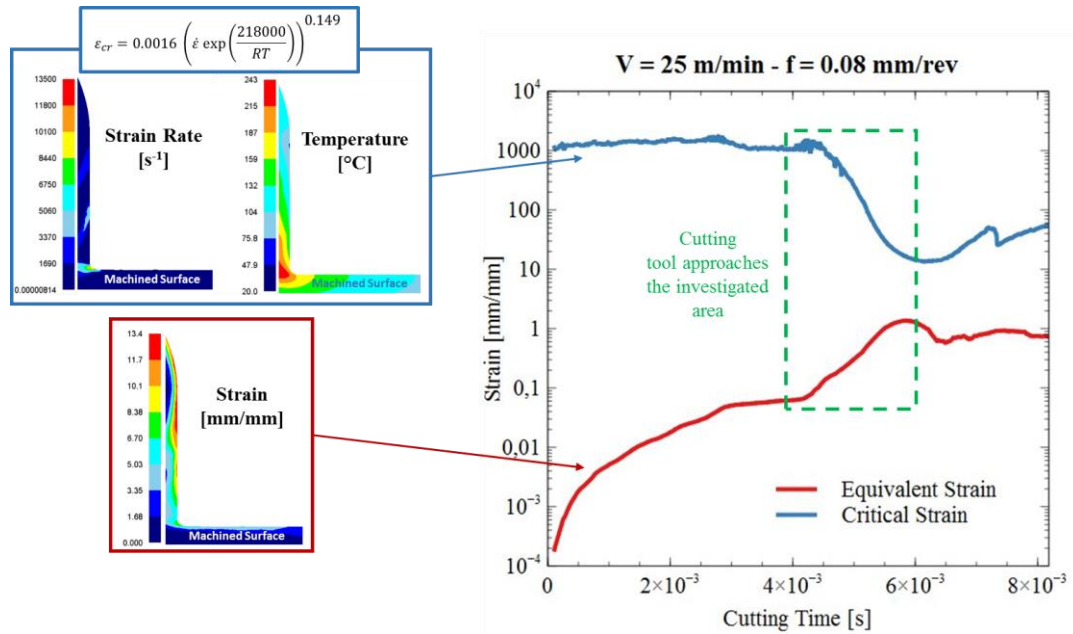
Fig. 57 Evolution of the critical and equivalent strains occurring on the processed surface during the progress of the machining procedure. In the most aggressive machining condition studied, the critical strain is always higher than the equivalent one, avoiding any triggering of *DRX* phenomena.

6.2.1 Finite Element Analysis (FEA)

Once the efficacy of the *FE* model for predicting some variables of interest (such as cutting forces and chip morphology) as well as the metallurgical changes was established, it could be used to investigate the effects of unexplored cutting conditions on the machined surface. Thus, to have a clear comprehension of the different microstructural phenomena, a broad simulation campaign was carried out to explore the strengthening effects by varying the material thermo-mechanical conditions. In particular, the strengthening contributions were studied by varying the strain and the Zener-Hollomon parameter (Eq. 39); the latter was used because it embodies both the strain rate and temperature effects. In Fig. 58 it is noticeable that the twinning induced strengthening tends to remain constant once the saturation strain (around 0.3) is exceeded [135]. In contrast, the dislocation accumulation contribution increases with strain and decreases with reduction in the Zener-Hollomon parameter. These simulated effects in Fig. 58 can be justified by deformation

induced dislocation nucleation and thermally induced dislocation annihilation processes that are at play during cutting.
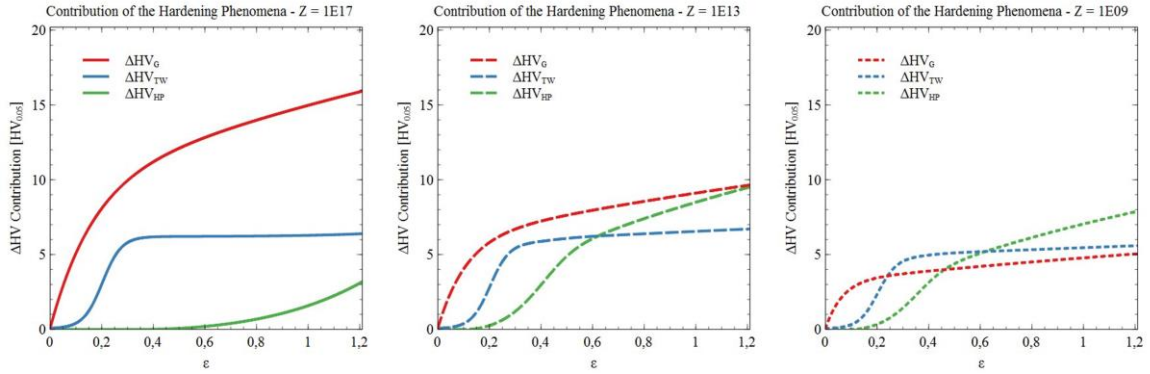
Fig. 58 Application of the proposed model to study the behaviour of the hardening contribution of the single physics phenomena occurring on the processed material on varying Zener-Hollomon parameter, that is representative of both strain rate and temperature evolution.

A lower value of the *Z-H* parameter corresponds to a lower critical strain and hence a premature triggering of *DRX*, which increases the *Hall-Petch* effect contribution. Moreover, all hardening effects tend to be reduced in magnitude at lower *Z-H* values. These results suggest that a proper setup of the *Z-H* parameter is necessary to find the optimum working conditions that yield the best possible contribution of the individual hardening mechanisms. Considering the gentle process conditions in micro cutting, the best strategy for setting up the *Z-H* parameter consists of increasing the material temperature. Therefore, the *FE* model was used to investigate the surface workpiece behaviour when it is preheated, such as in a hot machining process.

According to the literature [213–215], the authors chose to investigate the effects of surface preheating temperature in increments of 100°C, starting from 0°C to 800°C. It can be seen from Fig. 59 that a higher surface hardness strongly concentrated near the worked surface is obtained. Here, only the more interesting results are reported while the global trends are in accordance with previously shown results for the *Z-H* parameter.

Considering the deconvolution of effects, which is shown in Fig. 59b, the substantial hardness increase in the surface at 300°C depends on the higher *H-P* contribution due to a grain refinement layer of around 50 µm (Fig. 59a).

Fig. 59 Effects of different preheating temperatures (a) on sub-surface global hardening (15 m/min and 0.08 mm/rev) allowing to ident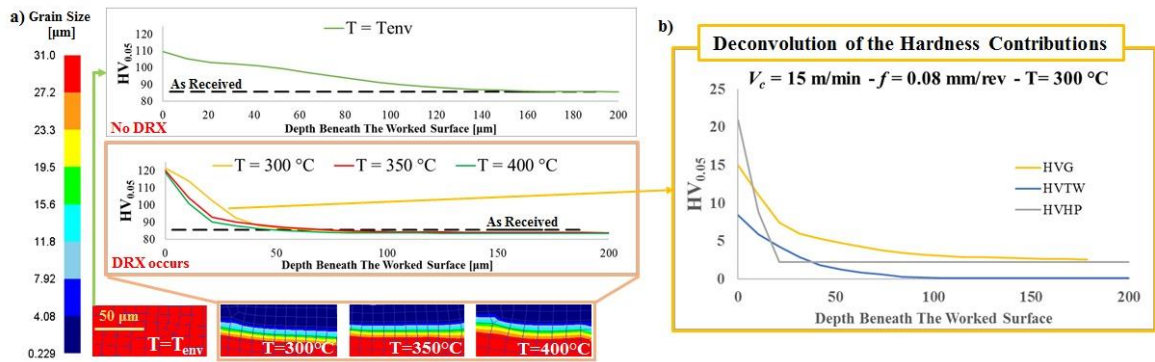ify the best preheating temperature, and (b) deconvolution of the different hardening effects under the found optimum preheating conditions of 300°C.

These outcomes explain the results reported by Baili et al. [215] who found that, when the preheating temperature in hot machining of a *Ti* alloy increases, the surface hardness maintains an almost constant value until it approaches around 30% of its melting temperature, except at a certain temperature where the machined surface hardness shows a significant peak. Accordingly, for the simulated conditions, once the preheating temperature of 300 °C is exceeded, the hardness tends to decrease because of temperature induced dislocation annihilation that is more dominant than the *H-P* effect. The hardness increase obtained in this manner is around 45% of the bulk material hardness, highlighting a remarkable improvement in the surface properties once the workpiece preheating temperature is set to the optimum value of 300 °C. Moreover, because of the higher temperatures involved, a more pronounced dislocation annihilation is noticeable in the machined sub-surface, where the grain refinement tends to be less prominent. This phenomenon results in reduction of the hardening effect due to reduction in the dislocation density because of thermally induced dislocation annihilation, and therefore the thickness of the hardened layer decreases.

6.3. *Ti6Al4V – FE* Model Validation, Results and Discussion

The results of the experimental tests were analysed and employed to validate the prediction capabilities of the *FE* numerical model. Primarily, the numerical results of the three components of the cutting forces and the temperatures at the tool chip interface were compared with the recordings and measurements taken during the experimental tests. Subsequently, the grain size and the surface and subsurface hardness trends were compared with the results and measurements obtained from the metallographic and microhardness analysis.

128

6.3.1 Cutting Forces and Temperatures

In a general 3D machining process, three reciprocally orthogonal privileged directions are usually considered as the basis for the definition of the cutting forces. The Main Cutting Force (F_c) acts in the tangential direction of the tool motion, the Thrust Force (F_t) acts in the radial direction of the turned workpiece, while the Feed Force (F_f) acts along the longitudinal axes of the workpiece. The sum of the square root of these three components leads to the definition of the Total Cutting Force (F_{tot}) that represent the global mechanical load imposed by the workpiece on the machining tool at the contact area [216].

Moreover, because of their strong influence on the material plastic behavior, it is also profitable to have deep information concerning the temperature increment at the tool-workpiece interface. The heat generation results from the plastic shearing work hardening and friction induced by the material flow on the cutting tool, which dramatically elevate the temperature during the material processing [217]. Both cutting forces and temperatures affect the deformation of the machined workpiece, influencing its dimensional accuracy, the machining system stability, and the tool wear progress, vibration and chatter [218].

Fig. 60 reports the experimentally obtained machining forces compared with the numerically predicted ones considering all the investigated machining parameters and lubri-cooling conditions. Conversely, in Fig. 61 the temperatures relieved via *IR* camera at the tool-workpiece interface and the predicted ones are reported.

Following the cutting speed increase, a higher work hardening phenomena occur on the processed material, influencing the material strengthening and the raising of the cutting forces. At the same time, the work hardening increment results in a higher heat development at the tool-workpiece interface, causing an increasing of the cutting temperature. This effect induces a more pronounced stress softening on the material, forcing the cutting forces to descend. Both the hardening and softening phenomena concur together during the machining process, and the predominance of one respect to the other can differently affect the evolution of the force trends with the increasing of the cutting speeds, above all when the material object of study is not particularly prone to be machined [24, 219]. The lowest cutting temperatures are relievable with the employment of cryogenic lubri-coolant and tend to rear when the involved fluid cooling capabilities became more gentle. The temperature increasing, on varying lubri-cooling technique, culminates under *MQL* and dry conditions, that show very few difference in terms of machining temperatures, due to the poor cooling power of the *MQL* technology [34, 220, 221].
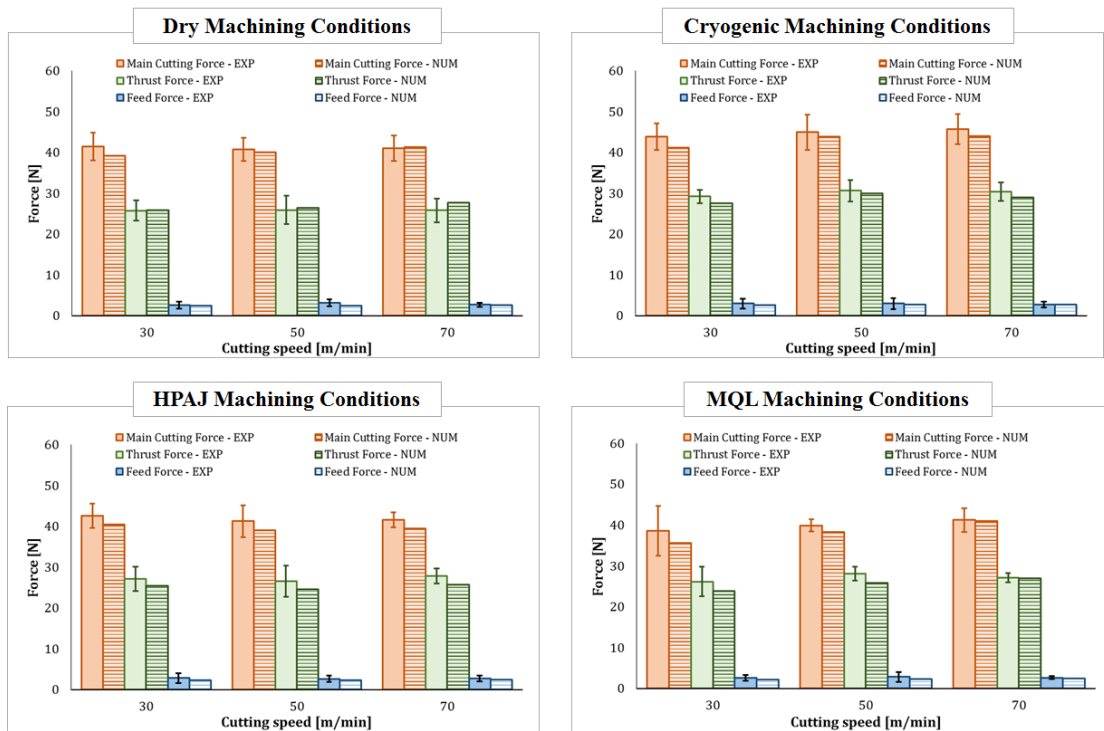
Fig. 60 Mean and variation of experimental (EXP) and numerical simulated (NUM) cutting forces, thrust forces and feed forces for all the investigated process parameters and lubri-cooling conditions.
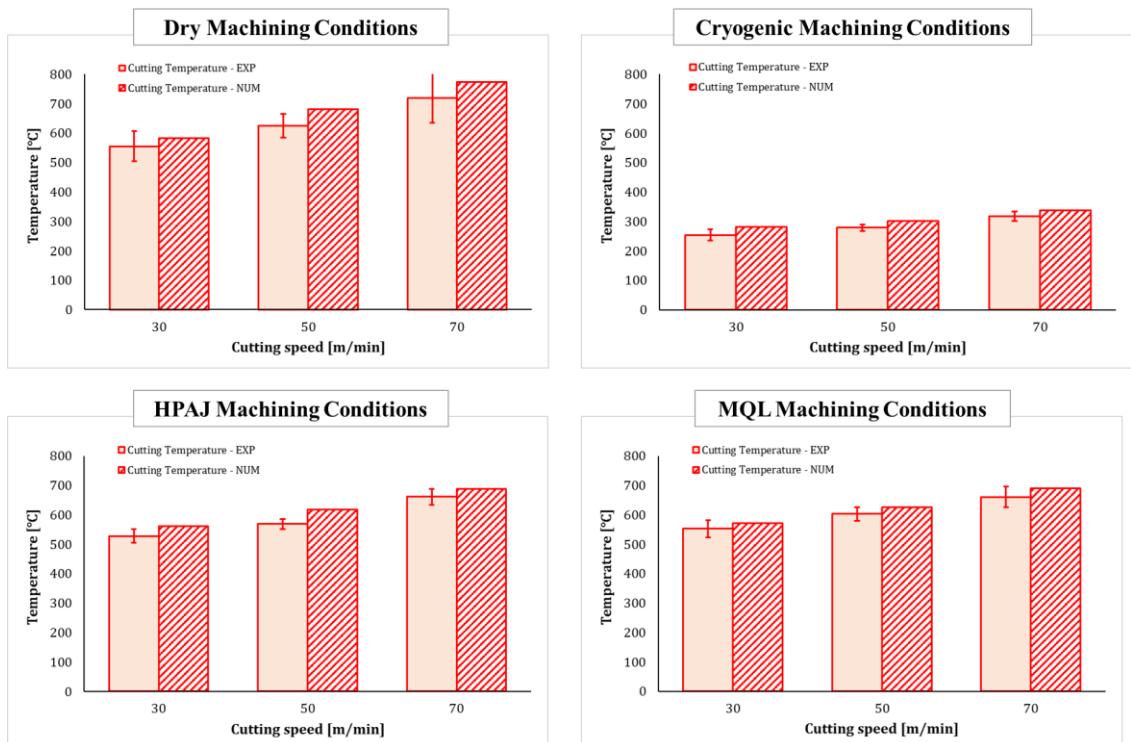

Fig. 61 Mean and variation of experimental (EXP) and numerical simulated (NUM) cutting temperatures for all the investigated process parameters and lubri-cooling conditions.

Under all the analyzed lubri-cooling conditions, it is possible to notice an overall rising trend of all the components of the machining forces. This is attributed to the high work hardening behavior of the workpiece material, that predominates respect to the softening effect. The latter is restrained because of the relatively low temperature increasing trend with the cutting speed rising. On varying the lubri-cooling conditions, it is possible to notice that under cryogenic conditions the highest machining forces are relievable, because of the combined effect of the reduced thermal softening and heightened work hardening induced by the higher friction conditions. Under dry conditions the machining forces are slightly lower, here the cutting temperatures are the highest, nevertheless the elevated friction effects induce the highest deformation work hardening, causing the forces to be approximately comparable with the ones registered under cryogenic conditions. Under *HPAJ* and *MQL* conditions the temperatures decreasing is not so prominent respect to the dry conditions. Therefore, the machining forces are majorly influenced by the inferior friction conditions, resulting in a forces decreasing when the lubricant effect is more accentuated.

In order to properly validate the numerical modeling strategy, a satisfactory comparison have to be found among the experimental results and the output variables obtainable from the *FE* model. In particular, the predicted main cutting forces, considering all the investigated parameters and lubri-cooling conditions, are in good agreement with those that were measured during the experimental procedures, with an overall average absolute error of 4.3%. Similarly, the thrust forces obtained from the model showed a mean absolute error of around 5%, while the feed forces comparison showed an error of 11%. Concerning the cutting temperatures prediction, an average absolute error of around 10% is noticeable. The two latter mean errors are higher than the ones on the main cutting forces and thrust forces. However, due to the very complex deformation process simulated, this specific entity of error was considered plenty acceptable, also referring to the common error ranges that that are available in the scientific literature and commonly accepted [72, 86, 87, 195].

6.3.1.2 Grain Size Evolution

Depending on the machining parameters, different microstructural phenomena may occur on the worked surface and subsurface. Zones of intense slip activity behave as preferred site for grains nucleation, causing *DRX*. In detail, grain refinement affected layers were noticed on the machined surfaces, where the thermo-mechanical loads were more prominent on the machining surface and extremely beneath it [72].

In detail, the thicknesses of these layers are lower than 8 µm for each investigated case and the dimensions of the layers are always comparable with the numerical predicted ones, as visible in Fig. 62a and Fig. 62c for the dry machining conditions.

Fig. 62b shows the comparison between the numerical and the experimental distribution of grain size measured on the machined subsurface and along the depth. In particular, the grain refinement is more significant when the cutting speed is higher because of the higher quantity of deformation and thermal energy imposed by severer machining conditions that cause a significant increment of the plastic work at the tool-workpiece interface and a reduction of the critical strain that, when overcame, triggers the dynamic recrystallization and promotes a premature grain nucleation, resulting in an overall reduction of the mean grain size [191, 192].
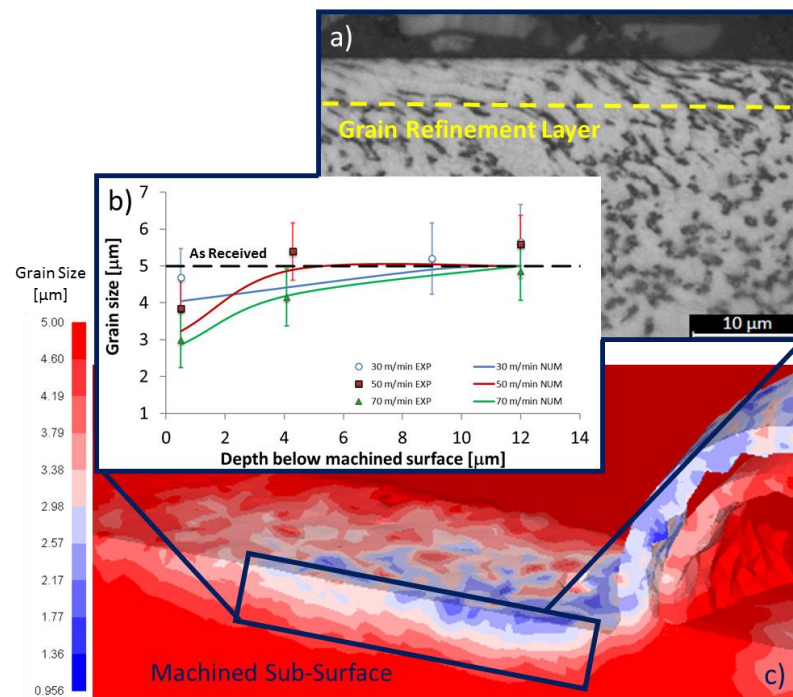
Fig. 62 Measured (EXP) and numerical predicted (NUM) microstructural modifications in terms of grain size in dry machining conditions.

Moreover, referring to Fig. 63, it is possible to observe that the numerical model predicts the grain size on the machined surface with considerable affordability for all the investigated machining parameters and lubri-cooling conditions. In particular, a global mean absolute error of around 5% is shown, giving further positive confirms concerning the correct validation of the numerical model.

According with [36], more aggressive cutting parameters, higher cutting speed in particular, cause an increasing in grain refinement effect in *Ti6Al4V* machining. Besides, lower cutting

temperatures produce a more restrained grain refinement, resulting in a descending trend in grain size with more effective coolant employment, culminating with the usage of cryogenic fluids, that limits the grain growing effects and consequently shows the highest grain refinement phenomenon on the machined surface [222]. The grain size reduction is almost negligible respect to the bulk material under dry machining at the lowest cutting speeds. On the other hand, it reaches a reduction until almost 25% under cryogenic conditions, that represent the optimum machining configuration to obtain the best microstructural improvement in terms of grain size.
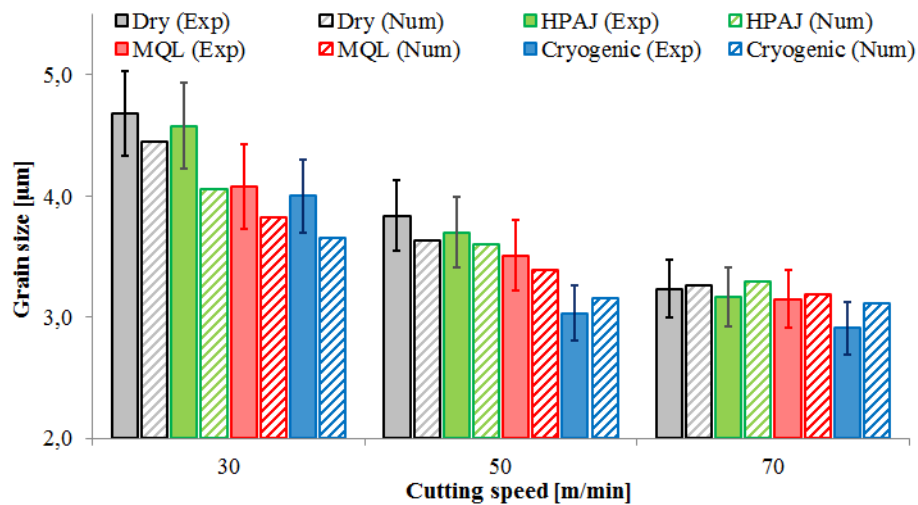
Fig. 63 Comparison between the experimentally measured (Exp) and the numerically predicted (Num) grain size on the machined surface.

6.3.1.3 Surface and Subsurface Microhardness

The grain refinement effect induced by the machining tool accounts for a significant increment in terms of microhardness, both on the processed surface and subsurface. This is an important index to evaluate the quality of a manufactured product, above all concerning its wear and corrosion behavior enhancement and its prediction can represent a significant mean to evaluate the capabilities of a manufacturing process [223]. The comparison between the measured and the predicted microhardness is reported in Fig. 64.

According with the experimental results, it is possible to notice that a hardened layer, that ranges between 50 and 80 μm of thickness, is present beneath the machined surface in all the investigated case studies. A slight increment of hardness is visible with the increasing of the cutting speed, according with the increment rate of grain refinement previously shown (Fig. 62 and Fig. 63).
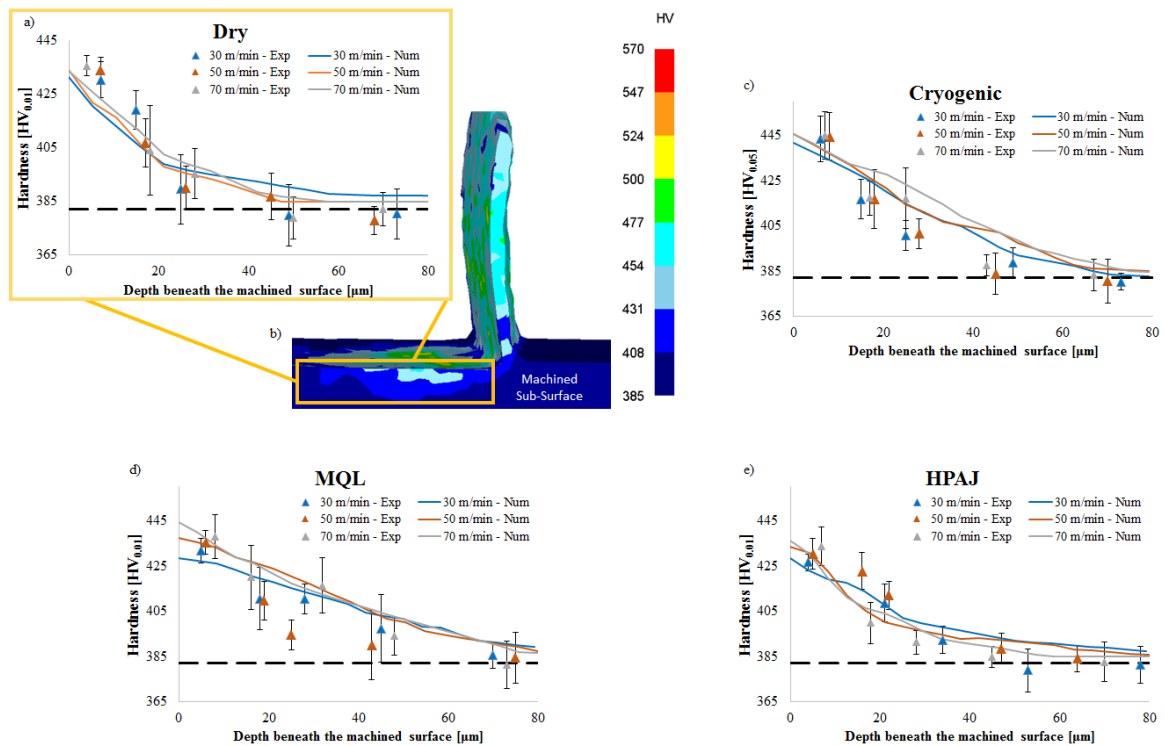
Fig. 64 Measured (Exp) and numerical predicted (Num) surface and subsurface microhardness graphical (a) and (b) visual comparison for dry, (c) cryogenic, (d) *MQL*, and (e) *HPAJ* machining.

The hardness prediction given from the numerical model shows an outstanding agreement with the experimental results, corroborating once again the overall goodness of the proposed model and confirming its effectiveness as a convenient tool able to investigate and predict the metallurgical changes that occur when the investigated alloy is subjected to severe mechanical deformations.

6.3.2 Finite Element Analysis (FEA)

The *FE* simulations allowed to predict the machining forces and temperatures, as well as to identify the occurred microstructural modifications, their related formation mechanism, and their effects on the hardness on the processed surface. Besides, once the reliability of the developed *FE* model for predicting the variables of interest (as well as the metallurgical changes), was proven, it can be used to investigate the effects of unexplored cutting conditions on the machined surface. Thus, to have a clear comprehension of the different microstructural phenomena under unexplored cutting parameters, the authors decided to perform a Finite Element Analysis (*FEA*) increasing the cutting speed to 90, 110 and 130 m/min. The chosen values maintain the cutting speed step increment used in the experimental campaign and they approaches to the severest parameters

explored for 2D orthogonal machining of the same alloy, under dry and cryogenic machining conditions and using a coated carbide inserts [36].

In Fig. 65 are visible the machining forces resulting from the *FEA*, while in Fig. 66 are visible the resulting cutting temperatures. The forces increasing trends with the raising cutting speeds relieved under the experimental analysis are confirmed. However, the cutting temperature under dry, *MQL* and *HPAJ* conditions tends to come near. Therefore, the differences between the respective cutting forces under these machining conditions are less evident, while the highest force values are registered under cryogenic machining conditions, as expected.
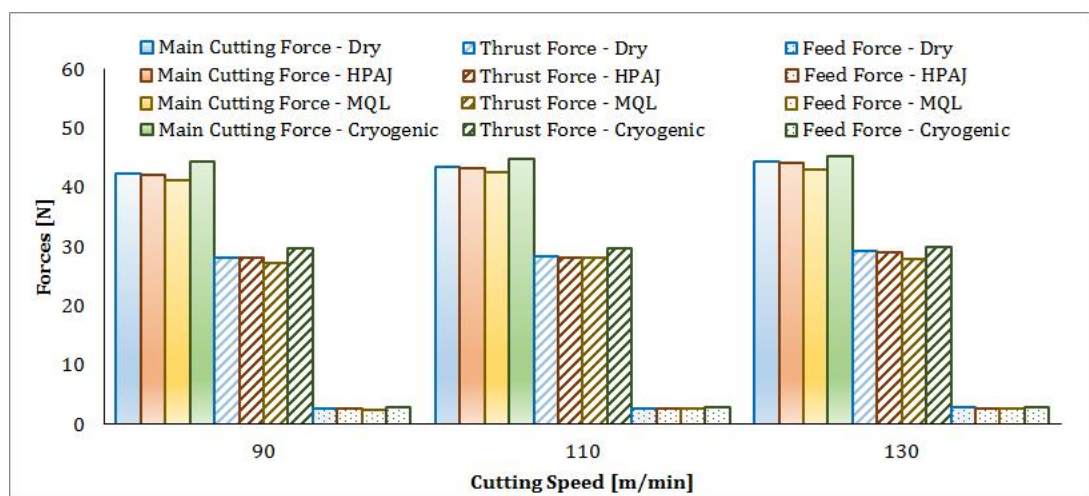
Fig. 65 Finite Element Analysis results: cutting forces, thrust forces and feed forces for the experimentally unexplored cutting parameters.
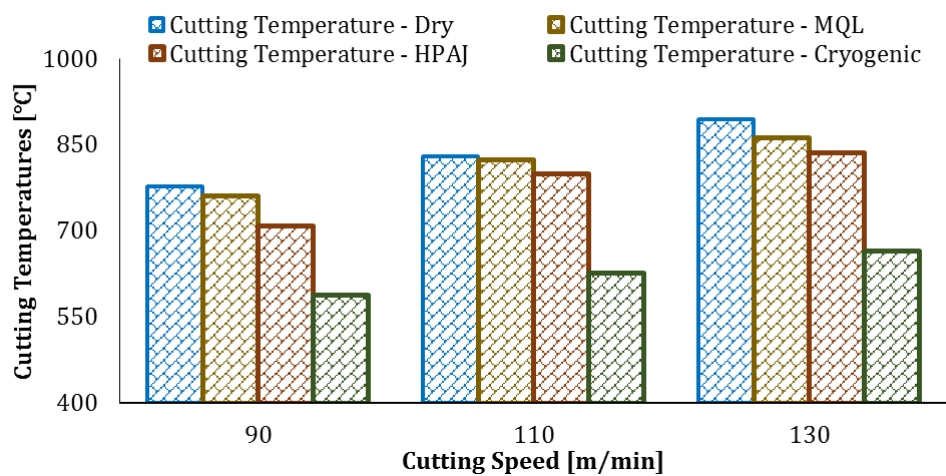
Fig. 66 Finite Element Analysis results: cutting temperatures for the experimentally unexplored cutting parameters.

Concerning the grain size reduction, the decreasing trends at higher cutting speeds are still visible, as relieved during the experimental campaign (Fig. 67). Moreover, the grain refinement dependence from the cutting temperatures is still relievable, resulting, as for the cutting forces, in very similar grain size values under Dry, *MQL* and *HPAJ* machining conditions. However, the employment of cryogenic fluid shows the best proneness to improve the surface integrity in terms of grain size because of the lowest temperatures reached.

The surface and subsurface hardness values are strictly dependent from the grain size because of the *Hall-Petch* effect. Therefore, as visible in Fig. 68, the surface values follow the same reduction trends reported for the grain size. Concerning the thickness of the hardened layer, the ranges tends to remain similar to the ones obtained in the experimental measurements, despite of the severer cutting conditions on the machined surface.
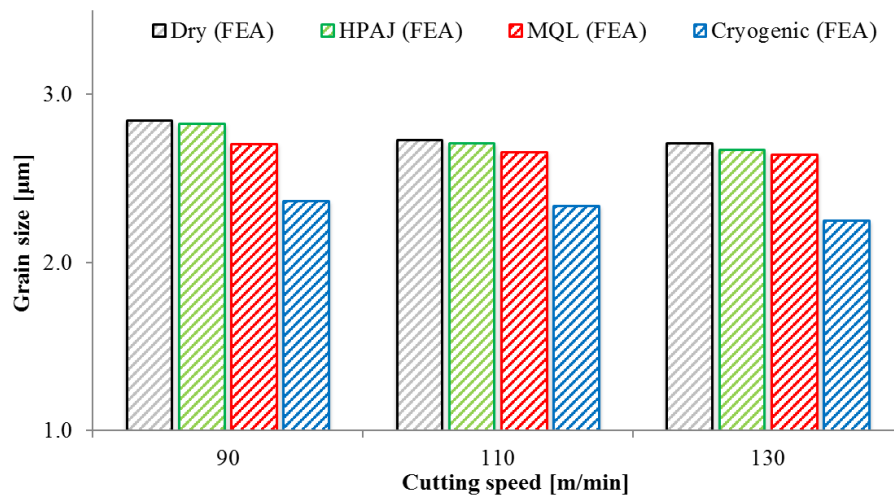
Fig. 67 Finite Element Analysis, grain size values on varying cutting speed and lubri-cooling conditions.
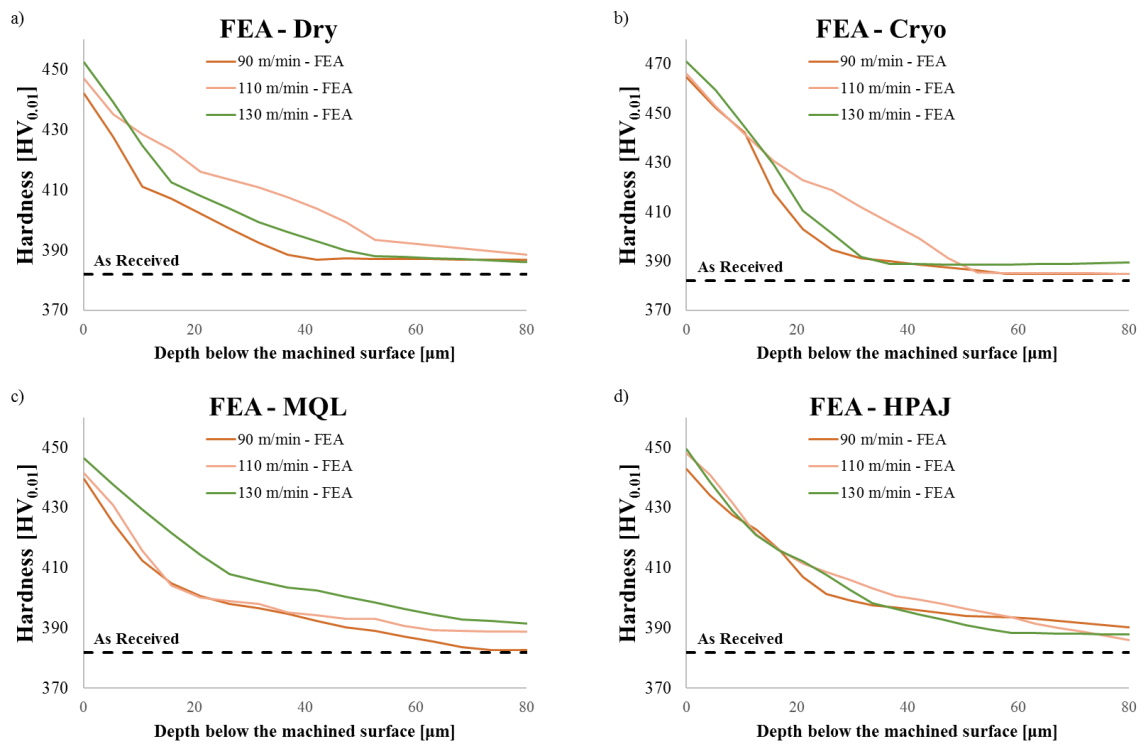
Fig. 68 Finite Element Analysis, surface and subsurface microhardness for (a) dry, (b) cryogenic, (c) *MQL*, and (d) *HPAJ* machining conditions.

Concluding Remarks

The main aim of this research work was to investigate the microstructural behavior of the processed materials and its effects on the process variables and final product quality and performances enhancement. The research work was performed in order to give important guidelines in process optimization and final product design to manufacturers and industries bound to traditional machining processes, aiming to intercept new market segments in occurrence of the negative effects due to the Electric Vehicles Revolution on *ICE* producers. Three particularly critical to machine materials were selected: *Waspaloy*, *CP-Ti* and *Ti6Al4V*. In particular, these materials were chosen because of preponderant interest pointing to intercept new growing sectors where machining operations will be significant: Biomedical, Aerospace/Aeronautic and Defense.

Concerning the first investigated materials, *Waspaloy*, the metallurgical phenomena induced by orthogonal cutting were experimentally investigated and numerically modelled. The main deformation mechanisms that affect the material during plastic deformation were preliminarily studied. The alloy showed significant plastically deformed regions characterized by grains with altered shapes, intense slip activity and, in some cases, crystal grains recrystallization, depending on the thermo-mechanical loads. Subsequently, a proper physics based modeling approach was developed to model the previous mechanisms identified and to study the metallurgical phenomena that were hard to be experimentally investigated. The reliability of the *FE* modeling procedure was confirmed by the good prediction of the global process variables, cutting forces and temperatures. Furthermore, the model predicted the metallurgical phenomena that occur on the chip and on the machined surface and subsurface, such as grain refinement layers and dislocation accumulation on the strongly deformed regions. In detail, the appearance of very thin layers of deformed material characterized by very small and indiscernible grains was numerically analyzed via *FE* simulations. The obtained results evidenced the new grain formations (sub-micrometer dimension) as dynamic recrystallization phenomenon due to the combination of very large strains and rapid freezing of the machined surface. Furthermore, the hardness variation induced by machining operation was experimentally measured. This variation was observed in a larger region characterized especially by deformed grains subjected to intense slip activity instead of grain refinement. Subsequently a FEA was performed to study the effect of higher cutting speed, namely 85m/min, on the cutting forces, temperature and surface integrity. The FEA showed that when the feed rate was fixed to 0.05mm/rev, the Waspaloy showed a strain hardening effect predominant when the cutting speed was increased while at higher feed rate (0.1mm/rev) the higher cutting speed led to thermal

softening effect predominant. This latter led to recovery effect, less accumulation of dislocation and thus sub-surface hardness.

For what concerns the *CP-Ti* processing investigation under macro/micromachining conditions, a physics based modeling approach was presented. The flow stress incorporates the different material strengthening/softening mechanisms, which evolve during severe plastic deformation, including dislocation accumulation, crystal twinning, and the *Hall-Petch* effects. Moreover, the model allows quantification of the hardening contributions of the different microstructure related physical mechanisms. The model was validated through comparison with experimental results (cutting forces, chip morphology, twin and deformed surface and subsurface layers and microhardness) showing good agreement. The machining forces were slightly affected by the cutting speed, and they showed a visible increment with increase in feed rate. The twinning affected layer was nearly 100 µm in depth, while the grain distortion effects are strongly visible for around 50 µm beneath the machined surface, for all the investigated case studies. Moreover, it was verified that using the best machining condition, the material hardening is around 25% higher than the bulk material. A *FE* analysis was also conducted to investigate unexplored cutting conditions. This analysis suggests that a further surface hardening of significant importance is obtainable through *DRX* in the worked surface, leading to an increase up to the 45% of the bulk material hardness. The *DRX* effect is not promoted under the gentle parameters that are typical of micro cutting, but can be enabled by the integration of an external workpiece preheating technology, thereby keeping the cutting parameters more typical of micromachining conditions and avoiding the employment of more aggressive process parameters. This approach can be utilized to design more efficient manufacturing process chains to pro- duce implants with superior mechanical properties.

Finally, concerning the third analyzed processed material, a physically based finite element constitutive model was proposed, in order to investigate the machining behavior of *Ti6Al4V*. The main aim was to explore the metallurgical phenomena that occur during the industrial process. In particular, the strengthening/softening phenomena of dislocation accumulation, grain refinement and dislocation drag were taken into account to formulate a proper flow stress model. Experimentally obtained machining forces and temperatures under different cutting speeds and lubri-cooling conditions were used to validate a 3D machining *FE* numerical model. The numerical data were in good agreement with the experimental ones. The average total error between the predicted and the measured main cutting forces and thrust forces was not higher than 5% in both cases, while the mean absolute error on feed force and cutting temperature prediction was of

around 13% and 7% respectively. Through the *FE* simulation, it was possible to predict also the metallurgical changes inside the layer beneath the machined surface induced by the turning process, both in terms of grain size and hardness. Indeed, according with the numerical model predictions, the hardening effect was attributed to the grain refinement phenomenon and modelled using the *H-P* strengthening model, showing a good matching with the microhardness measured on the processed surface. Under the optimum found machining conditions, a grain size reduction of around 35% and a hardness increment of the 17% respect the as received material were obtained. Subsequently, a Finite Element Analysis was performed to study the effect of untested cutting speed on the cutting forces, temperatures and metallurgical modifications. The experimentally relieved trends are followed under the numerically investigated process parameters, and higher surface performances are reached, finding new working ranges that allow to reach even better surface microstructural performances, with a grain size reduction lower than the 50% and a hardness increment until the 23% compared with the as received material.

The engagement of a physics based model allows to get a deeper understanding of the metallurgical phenomena occurring when large plastic strains are involved with a better prediction of the experimental data, that is a fundamental tenet in the design of high performance and reliable industrial processes.

Future Research Directions

According with the results reported in this research work, the exploited numerical investigation approach results to be extremely flexible and versatile. Therefore, its investigation capacities can be applied to other materials for critical applications in the market sectors that were chosen as target for this research work, such as AISI 52100 steel alloy, advanced aluminum alloys and titanium superalloys. All the listed materials result to be particularly susceptible when machined under aggressive, or in some case also under moderate, cutting parameters, and in scientific literature there is a visible lack of knowledge for what concern their physics based model based investigation. Moreover, Molecular Dynamics represents an even stronger inspection methodology that can be used for machined materials. However, it is even more difficult to be implemented than physics based modeling, and this issue discourage the researcher to build up simulations based on this technique. On the other hand, the latter can be integrated into physics based models, allowing the researcher to obtain similar results, avoiding high implementation complexity and excessive computational loads.

REFERENCES

[1]   Chan CC (1993). An Overview of Electric Vehicle Technology. Proceedings of the IEEE 81:1202–1213. https://doi.org/10.1109/5.237530

[2]   Du J, Ouyang M (2013). Review of electric vehicle technologies progress and development prospect in China. World Electric Vehicle Journal 6:1086–1093. https://doi.org/10.3390/wevj6041086

[3]   Shen C, Shan P, Gao T (2011). A comprehensive overview of hybrid electric vehicles. International Journal of Vehicular Technology 2011:. https://doi.org/10.1155/2011/571683

[4]   BloomberNEF (2020). Electric Vehicles to Accelerate to 54% of New Car Sales by 2040

[5]   Lang T (2020). Electric vehicles coming of age

[6]   Sohrabi C, Alsafi Z, O'Neill N, et al (2020). World Health Organization declares global emergency: A review of the 2019 novel coronavirus (COVID-19). International Journal of Surgery 76:71–76. https://doi.org/10.1016/j.ijsu.2020.02.034

[7]   Lucintel© (2020). ASSESSING THE IMPACT OF COVID - 19 ON VARIOUS INDUSTRIES COVID 19 – Assessing its Impact

[8]   Little AD (2020). Win the automotive COVID-19 rebound

[9]   Collie B, Grover P, Huber T, et al (2020). Auto companies will outlast COVID-19 and come out stronger. Boston Consulting Group 1–14

[10]   Hader M (2020). Covid-19 – How We Will Need To Rethink the Aerospace Industry

[11]   Oliver Wyman (2020). COVID-19 Impact On Commercial Aviation Maintenance

[12]   Xu L, Deng W, Liu W, et al (2014). Optimization of process planning for cylinder block based on feature machining elements. Conference Proceedings - IEEE International Conference on Systems, Man and Cybernetics 2014-Janua:2575–2580. https://doi.org/10.1109/smc.2014.6974315

[13]   Kibkalt D, Mayr A, Von Lindenfels J, Franke J (2019). Towards a Data-Driven Process Monitoring for Machining Operations Using the Example of Electric Drive Production. 2018 8th Int Electr Drives Prod Conf EDPC 2018 - Proc. https://doi.org/10.1109/EDPC.2018.8658293

[14]   Allen DM, Simpkins M, Almond H (2010). A novel photochemical machining process for magnesium aerospace and biomedical microengineering applications. Journal of Micromechanics and Microengineering 20:. https://doi.org/10.1088/0960-1317/20/10/105010

[15]   Dambatta YS, Sarhan AAD, Sayuti M, Hamdi M (2017). Ultrasonic assisted grinding of advanced materials for biomedical and aerospace applications—a review. International Journal of Advanced Manufacturing Technology 92:3825–3858. https://doi.org/10.1007/s00170-017-0316-z

[16]   Kumar Sharma V, Kumar A (2014). Micro Machining-A Review. Certified Institute) Ghaziabad 4:2250–2459

[17]   Porter DL, Totemeier TC (2003). Mechanical properties of metals and alloys

[18] Davim JP, Astakhov VP (2011). Machining of Hard Metals

[19] MarketsAndMarkets (2021). Aerospace High Performance Alloys Market, by Alloy Type, by Product Type, by Alloying Element, by Geography, Forecast to 2021

[20] Grand View Research (2017). High Performance Alloys Market Size, Share & Trend Analysis Report By Product (Non-ferrous, Platinum group, Refractory, Super alloys), By Material, By Application, And Segment Forecasts, 2018 - 2024

[21] Grand View Research (2017). Osseointegration Implants Market Size, Share & Trends Analysis Report By End Use (ASCs, Hospitals, Dental Clinics), By Product (Dental, Knee, Hip, Spinal Implants), By Region, And Segment Forecasts, 2018 - 2026

[22] IDataResearch (2019). Dental Implants Market Analysis , Size , Trends 2019-2025

[23] Yang S, Pu Z, Puleo DA, et al (2011). Advances in Sustainable Manufacturing. Adv Sustain Manuf. https://doi.org/10.1007/978-3-642-20183-7

[24] Sun Z, Ji X, Zhang W, et al (2020). Microstructure evolution and high temperature resistance of Ti6Al4V/Inconel625 gradient coating fabricated by laser melting deposition. Materials and Design 191:108644. https://doi.org/10.1016/j.matdes.2020.108644

[25] Muñoz JA, Higuera OF, Benito JA, et al (2019). Analysis of the micro and substructural evolution during severe plastic deformation of ARMCO iron and consequences in mechanical properties. Materials Science and Engineering A 740–741:108–120. https://doi.org/10.1016/j.msea.2018.10.100

[26] Bai Y, Chaudhari A, Wang H (2020). Investigation on the microstructure and machinability of ASTM A131 steel manufactured by directed energy deposition. Journal of Materials Processing Technology 276:116410. https://doi.org/10.1016/j.jmatprotec.2019.116410

[27] Raof NA, Ghani JA, Haron CHC (2019). Machining-induced grain refinement of AISI 4340 alloy steel under dry and cryogenic conditions. Journal of Materials Research and Technology 8:4347–4353. https://doi.org/10.1016/j.jmrt.2019.07.045

[28] Imbrogno S, Rinaldi S, Umbrello D, et al (2018). A physically based constitutive model for predicting the surface integrity in machining of Waspaloy. Materials and Design 152:. https://doi.org/10.1016/j.matdes.2018.04.069

[29] Arrazola PJ, Özel T, Umbrello D, et al (2013). Recent advances in modelling of metal machining processes. CIRP Annals - Manufacturing Technology 62:695–718. https://doi.org/10.1016/j.cirp.2013.05.006

[30] Melkote SN, Grzesik W, Outeiro J, et al (2017). Advances in material and friction data for modelling of metal machining. CIRP Annals - Manufacturing Technology 66:731–754. https://doi.org/10.1016/j.cirp.2017.05.002

[31] Caruso S, Imbrogno S, Rinaldi S, Umbrello D (2017). Finite element modeling of microstructural changes in Waspaloy dry machining. International Journal of Advanced Manufacturing Technology 89:227–240. https://doi.org/10.1007/s00170-016-9037-y

[32] Jafarian F, Imaz Ciaran M, Umbrello D, et al (2014). Finite element simulation of machining Inconel 718 alloy including microstructure changes. International Journal of Mechanical Sciences 88:110–121. https://doi.org/10.1016/j.ijmecsci.2014.08.007

[33] Usui E, Shirakashi T, Kitagawa T (1984). Analytical prediction of cutting tool wear. Wear 100:129–151. https://doi.org/10.1016/0043-1648(84)90010-3

[34] Rinaldi S, Caruso S, Umbrello D, et al (2018). Machinability of Waspaloy under different cutting and lubri-cooling conditions. International Journal of Advanced Manufacturing Technology 94:3703–3712. https://doi.org/10.1007/s00170-017-1133-0

[35] Umbrello D, Yang S, Dillon OW, Jawahir IS (2012). Effects of cryogenic cooling on surface layer alterations in machining of AISI 52100 steels. Materials Science and Technology (United Kingdom) 28:1320–1331. https://doi.org/10.1179/1743284712Y.0000000052

[36] Rotella G, Umbrello D (2014). Finite element modeling of microstructural changes in dry and cryogenic cutting of Ti6Al4V alloy. CIRP Annals - Manufacturing Technology 63:69–72. https://doi.org/10.1016/j.cirp.2014.03.074

[37] Ulutan D, Ozel T (2011). Machining induced surface integrity in titanium and nickel alloys: A review. International Journal of Machine Tools and Manufacture 51:250–280. https://doi.org/10.1016/j.ijmachtools.2010.11.003

[38] Astakhov VP, Davim JP (2010). Surface integrity in machining

[39] Field M, Kahles JF, Cammett JT (1972). Review of Measuring Methods for Surface Integrity. Ann CIRP 21:219–238

[40] Sharma S, Meena A (2020). Microstructure attributes and tool wear mechanisms during high-speed machining of Ti-6Al-4V. Journal of Manufacturing Processes 50:345–365. https://doi.org/10.1016/j.jmapro.2019.12.029

[41] Minkowycz WJ, Sparrow EM, Murthy JY, Abraham JP (2009). Handbook of Numerical Heat Transfer: Second Edition. Handbook of Numerical Heat Transfer: Second Edition 1–968. https://doi.org/10.1002/9780470172599

[42] Ulutan D, Erdem Alaca B, Lazoglu I (2007). Analytical modelling of residual stresses in machining. Journal of Materials Processing Technology 183:77–87. https://doi.org/10.1016/j.jmatprotec.2006.09.032

[43] Ghanem F, Braham C, Fitzpatrick ME, Sidhom H (2002). Effect of near-surface residual stress and microstructure modification from machining on the fatigue endurance of a tool steel. Journal of Materials Engineering and Performance 11:631–639. https://doi.org/10.1361/105994902770343629

[44] Arisoy YM, Özel T (2015). Prediction of machining induced microstructure in Ti-6Al-4V alloy using 3-D FE-based simulations: Effects of tool micro-geometry, coating and cutting conditions. Journal of Materials Processing Technology 220:1–26. https://doi.org/10.1016/j.jmatprotec.2014.11.002

[45] Özel T, Ulutan D (2012). Prediction of machining induced residual stresses in turning of titanium and nickel based alloys with experiments and finite element simulations. CIRP Annals - Manufacturing Technology 61:547–550. https://doi.org/10.1016/j.cirp.2012.03.100

[46] Novovic D, Dewes RC, Aspinwall DK, et al (2004). The effect of machined topography and integrity on fatigue life. International Journal of Machine Tools and Manufacture 44:125–134. https://doi.org/10.1016/j.ijmachtools.2003.10.018

[47] Chrzanowski W, Neel EAA, Armitage DA, Knowles JC (2008). Effect of surface treatment on the bioactivity of nickel-titanium. Acta Biomaterialia 4:1969–1984. https://doi.org/10.1016/j.actbio.2008.05.010

[48]   Raabe D (1998). Computational Materials Science - The Simulation of Materials Microstructures and Properties. Wiley-VCH

[49]   Rosenblueth A, Wiener N (1945). The Role of Models in Science. Philosophy of Science 12:316–321

[50]   Salsa S (2008). Partial Differential Equations in Space. Springer-Verlag Italia srl –

[51]   Howison S (2005). Practical applied mathematics: Modelling, analysis, approximation. Cambridge University Press

[52]   Khosrow-Pour M (1984). Materials Science and Engineering: Concepts, Methodologies, Tools, and Applications. Information Resources Management Association USA

[53]   Hergert W, Ernst A, Dane M (2004). Computational Material Science. Springer, Berlin Heidelberg

[54]   Needleman A (2000). Computational mechanics at the mesoscale. Acta Materialia 48:105–124. https://doi.org/10.1016/S1359-6454(99)00290-6

[55]   Onck P, Van Der Giessen E (1998). Growth of an initially sharp crack by grain boundary cavitation. Journal of the Mechanics and Physics of Solids 47:99–139. https://doi.org/10.1016/S0022-5096(98)00078-7

[56]   Needleman A (1994). Computational modeling of material failure. Applied Mechanics Reviews 47:S34–S42. https://doi.org/10.1115/1.3124437

[57]   Fleck NA, Muller GM, Ashby MF, Hutchinson JW (1994). Strain gradient plasticity: Theory and experiment. Acta Metallurgica Et Materialia 42:475–487. https://doi.org/10.1016/0956-7151(94)90502-9

[58]   De Guzman MS, Neubauer G, Flinn P, Nix WD (1993). MATERIALS. Materials Research Society Symposium Proceedings 308:613–618

[59]   Daoud M, Chatelain JF, Bouzid A (2017). Effect of rake angle-based Johnson-Cook material constants on the prediction of residual stresses and temperatures induced in Al2024-T3 machining. International Journal of Mechanical Sciences 122:392–404. https://doi.org/10.1016/j.ijmecsci.2017.01.020

[60]   Luo J, Li M, Li X, Shi Y (2010). Constitutive model for high temperature deformation of titanium alloys using internal state variables. Mechanics of Materials 42:157–165. https://doi.org/10.1016/j.mechmat.2009.10.004

[61]   Atmani Z, Haddag B, Nouari M, Zenasni M (2016). Combined microstructure-based flow stress and grain size evolution models for multi-physics modelling of metal machining. International Journal of Mechanical Sciences 118:77–90. https://doi.org/10.1016/j.ijmecsci.2016.09.016

[62]   Das AJ (2007). Tensors: the mathematics of relativity theory and continuum mechanics. Springer

[63]   Braess D (2007). Finite elements: theory, fast solvers, and applications in elasticity theory. Cambridge University Press

[64]   Javier Bonet, Wood RD (1997). NONLINEAR CONTINUUM MECHANICS FOR FINITE ELEMENT ANALYSIS. Cambridge University Press

[65]   Nes E (1997). Modelling of work hardening and stress saturation in FCC metals. Progress

in Materials Science 41:129–193. https://doi.org/10.1016/S0079-6425(97)00032-7

[66] Kocks UF, Mecking H (2003). Physics and phenomenology of strainhardening: the FCC case. Progress in Materials Science 48:71–273. https://doi.org/10.4324/9781315279015

[67] Zehetbauer M, Seumer V (1993). Cold work hardening in stages IV and V of F.C.C. metals-I. Experiments and interpretation. Acta Metallurgica Et Materialia 41:577–588. https://doi.org/10.1016/0956-7151(93)90088-A

[68] Lin YC, Chen MS, Zhong J (2008). Constitutive modeling for elevated temperature flow behavior of 42CrMo steel. Computational Materials Science 42:470–477. https://doi.org/10.1016/j.commatsci.2007.08.011

[69] Follansbee PS, Kocks UF (1988). A constitutive description of the deformation of copper based on the use of the mechanical threshold stress as an internal state variable. Acta Metallurgica 36:81–93. https://doi.org/10.1016/0001-6160(88)90030-2

[70] Johnson GR, Cook WH (1983). A Computational Constitutive Model and Data for Metals Subjected to Large Strain, High Strain Rates and High Pressures. the Seventh International Symposium on Ballistics 541–547

[71] Dorogoy A, Rittel D (2009). Determination of the johnson-cook material parameters using the SCS specimen. Experimental Mechanics 49:881–885. https://doi.org/10.1007/s11340-008-9201-x

[72] Imbrogno S, Rinaldi S, Umbrello D, et al (2018). A physically based constitutive model for predicting the surface integrity in machining of Waspaloy. Materials and Design 152:140–155. https://doi.org/10.1016/j.matdes.2018.04.069

[73] Yanagimoto F, Shibanuma K, Suzuki K, Matsumoto T (2019). A physics based model to simulate brittle crack arrest in steel plates incorporating experimental and numerical evidences. Engineering Fracture Mechanics 221:106660. https://doi.org/10.1016/j.engfracmech.2019.106660

[74] Motaman SAH, Prahl U (2019). Microstructural constitutive model for polycrystal viscoplasticity in cold and warm regimes based on continuum dislocation dynamics. Journal of the Mechanics and Physics of Solids 122:205–243. https://doi.org/10.1016/j.jmps.2018.09.002

[75] Taylor GI (1934). The mechanism of plastic deformation of crystals. Part I. — Theoretical. Proceedings of the Royal Society of London Series A, Containing Papers of a Mathematical and Physical Character 145:362–387. https://doi.org/10.1098/rspa.1934.0107

[76] Taylor GI (1934). The mechanism of plastic deformation of crystals. Part II.—Comparison with observations. Proceedings of the Royal Society of London Series A, Containing Papers of a Mathematical and Physical Character 145:388–404. https://doi.org/10.1098/rspa.1934.0107

[77] Mughrabi H (1983). Dislocation wall and cell structures and long-range internal stresses in deformed metal crystals. Acta Metallurgica 31:1367–1379. https://doi.org/10.1016/0001-6160(83)90007-X

[78] Prinz FB, Argon AS (1984). The evolution of plastic resistance in large strain plastic flow of single phase subgrain forming metals. Acta Metallurgica 32:1021–1028

[79] Nix WD, Gibeling JC, Hughes DA (1985). Time-dependent deformation of metals.

Metallurgical Transactions A 16:2215–2226. https://doi.org/10.1007/BF02670420

[80] Estrin Y, Mecking H (1984). A unified phenomenological description of work hardening and creep based on one-parameter models. Acta Metallurgica 32:57–70. https://doi.org/10.1016/0001-6160(84)90202-5

[81] Estrin Y, Kubin LP (1986). Local strain hardening and nonuniformity of plastic deformation. Acta Metallurgica 34:2455–2464. https://doi.org/10.1016/0001-6160(86)90148-3

[82] Gutierrez-Urrutia I, Raabe D (2012). Multistage strain hardening through dislocation substructure and twinning in a high strength and ductile weight-reduced Fe-Mn-Al-C steel. Acta Materialia 60:5791–5802. https://doi.org/10.1016/j.actamat.2012.07.018

[83] Mulford RA (1979). Analysis of strengthening mechanisms in alloys by means of thermal-activation theory. Acta Metallurgica 27:1115–1124. https://doi.org/10.1016/0001-6160(79)90129-9

[84] Hull R, Bean JC, Logan RA (1993). Misfit dislocations in strained layer epitaxy. Solid State Phenomena 32–33:417–432. https://doi.org/10.4028/www.scientific.net/SSP.32-33.417

[85] Svoboda A, Wedberg D, Lindgren LE (2010). Simulation of metal cutting using a physically based plasticity model. Modelling and Simulation in Materials Science and Engineering 18:. https://doi.org/10.1088/0965-0393/18/7/075005

[86] Melkote SN, Liu R, Fernandez-Zelaia P, Marusich T (2015). A physically based constitutive model for simulation of segmented chip formation in orthogonal cutting of commercially pure titanium. CIRP Annals - Manufacturing Technology 64:65–68. https://doi.org/10.1016/j.cirp.2015.04.060

[87] Fernandez-Zelaia P, Melkote S, Marusich T, Usui S (2017). A microstructure sensitive grain boundary sliding and slip based constitutive model for machining of Ti-6Al-4V. Mechanics of Materials 109:67–81. https://doi.org/10.1016/j.mechmat.2017.03.018

[88] Bernstein J (2018). Advanced Quantum Mechanics

[89] Chen X, Xiong L, McDowell DL, Chen Y (2017). Effects of phonons on mobility of dislocations and dislocation arrays. Scripta Materialia 137:22–26. https://doi.org/10.1016/j.scriptamat.2017.04.033

[90] Tian D, Zhou CJ, He JH (2018). Hall-Petch effect and inverse Hall-Petch effect: A fractal unification. Fractals 26:. https://doi.org/10.1142/S0218348X18500834

[91] Sargent GA, Zane AP, Fagin PN, et al (2008). Low-temperature coarsening and plastic flow behavior of an alpha/beta titanium billet material with an ultrafine microstructure. Metallurgical and Materials Transactions A: Physical Metallurgy and Materials Science 39:2949–2964. https://doi.org/10.1007/s11661-008-9650-y

[92] Doherty RD, Hughes DA, Humphreys FJ, et al (1997). Current issues in recrystallization: A review. Materials Science and Engineering A 238:219–274. https://doi.org/10.1016/S0921-5093(97)00424-3

[93] Huang K, Logé RE (2016). A review of dynamic recrystallization phenomena in metallic materials. Materials and Design 111:548–574. https://doi.org/10.1016/j.matdes.2016.09.012

[94] Glover G, Sellars CM (1973). RECOVERY AND RECRYSTALLIZATION DURING

HIGH TEMPERATURE DEFORMATION OF alpha -IRON. Metall Trans 4:765–775. https://doi.org/10.1007/BF02643086

[95]   Sakai T, Belyakov A, Kaibyshev R, et al (2014). Dynamic and post-dynamic recrystallization under hot, cold and severe plastic deformation conditions. Progress in Materials Science 60:130–207. https://doi.org/10.1016/j.pmatsci.2013.09.002

[96]   Ding R, Guo ZX (2001). Coupled quantitative simulation of microstructural evolution and plastic flow during dynamic recrystallization. Acta Materialia 49:3163–3175. https://doi.org/10.1016/S1359-6454(01)00233-6

[97]   Zhu YT, Langdon TG (2005). Influence of grain size on deformation mechanisms: An extension to nanocrystalline materials. Materials Science and Engineering A 409:234–242. https://doi.org/10.1016/j.msea.2005.05.111

[98]   Zhu YT, Liao XZ, Wu XL (2012). Deformation twinning in nanocrystalline materials. Progress in Materials Science 57:1–62. https://doi.org/10.1016/j.pmatsci.2011.05.001

[99]   Wusatowska-Sarnek AM, Miura H, Sakai T (2002). Nucleation and microtexture development under dynamic recrystallization of copper. Materials Science and Engineering A 323:177–186. https://doi.org/10.1016/S0921-5093(01)01336-3

[100]   Courtney TH (2000). Mechanical behavior of materials. Waveland Press, INC

[101]   Zheng K, Li Y, Yang S, et al (2020). Investigation and modeling of the preheating effects on precipitation and hot flow behavior for forming high strength AA7075 at elevated temperatures. Journal of Manufacturing and Materials Processing 4:. https://doi.org/10.3390/JMMP4030076

[102]   Lugovy M, Slyunyayev V, Brodnikovskyy M (2020). Solid solution strengthening in multiprincipal element fcc and bcc alloys: Analytical approach. Progress in Natural Science: Materials International 1–10. https://doi.org/10.1016/j.pnsc.2019.02.008

[103]   Bhadeshia H, Honeycombe R (2006). Steels: Microstructure and Properties. Elsevier Ltd

[104]   Ma K, Wen H, Hu T, et al (2014). Mechanical behavior and strengthening mechanisms in ultrafine grain precipitation-strengthened aluminum alloy. Acta Materialia 62:141–155. https://doi.org/10.1016/j.actamat.2013.09.042

[105]   Orowan E (1934). Zur Kristallplastizit�t. II. Zeitschrift f�r Physik 89:614–633. https://doi.org/10.1007/bf01341479

[106]   Seeger A, Schöck G (1953). The splitting of dislocations in metals with close-packed lattices. Acta Metallurgica 1:519–530. https://doi.org/10.1016/0001-6160(53)90082-0

[107]   Gil Sevillano J, van Houtte P, Aernoudt E (1980). Large strain work hardening and textures. Progress in Materials Science 25:69–134. https://doi.org/10.1016/0079-6425(80)90001-8

[108]   Mohamed FA (2003). A dislocation model for the minimum grain size obtainable by milling. Acta Materialia 51:4107–4119. https://doi.org/10.1016/S1359-6454(03)00230-1

[109]   Ding H, Shen N, Shin YC (2011). Modeling of grain refinement in aluminum and copper subjected to cutting. Computational Materials Science 50:3016–3025. https://doi.org/10.1016/j.commatsci.2011.05.020

[110]   Ding H, Shin YC (2014). Dislocation density-based grain refinement modeling of orthogonal cutting of titanium. Journal of Manufacturing Science and Engineering,

Transactions of the ASME 136:. https://doi.org/10.1115/1.4027207

[111] Ding H, Shin YC (2013). Multi-physics modeling and simulations of surface microstructure alteration in hard turning. Journal of Materials Processing Technology 213:877–886. https://doi.org/10.1016/j.jmatprotec.2012.12.016

[112] Ding H, Shin YC (2012). A metallo-thermomechanically coupled analysis of orthogonal cutting of AISI 1045 steel. Journal of Manufacturing Science and Engineering, Transactions of the ASME 134:. https://doi.org/10.1115/1.4007464

[113] Liu K, Melkote SN (2007). Finite element analysis of the influence of tool edge radius on size effect in orthogonal micro-cutting process. International Journal of Mechanical Sciences 49:650–660. https://doi.org/10.1016/j.ijmecsci.2006.09.012

[114] Wu H, Ma J, Lei S (2018). FEM prediction of dislocation density and grain size evolution in high-speed machining of Al6061-T6 alloy using microgrooved cutting tools. International Journal of Advanced Manufacturing Technology 95:4211–4227. https://doi.org/10.1007/s00170-017-1476-6

[115] Thakur A, Gangopadhyay S (2016). State-of-the-art in surface integrity in machining of nickel-based super alloys. International Journal of Machine Tools and Manufacture 100:25–54. https://doi.org/10.1016/j.ijmachtools.2015.10.001

[116] Birosca S, Di Gioacchino F, Stekovic S, Hardy M (2014). A quantitative approach to studying the effect of local texture and heterogeneous plastic strain on the deformation micromechanism in RR1000 nickel-based superalloy. Acta Materialia 74:110–124. https://doi.org/10.1016/j.actamat.2014.04.039

[117] Jianguo L, Pietrzyk M, Balint D (2012). Microstructure Evolution in Metal Forming Processes: Modelling and Applications

[118] Liew PJ, Shaaroni A, Sidik NAC, Yan J (2017). An overview of current status of cutting fluids and cooling techniques of turning hard steel. International Journal of Heat and Mass Transfer 114:380–394. https://doi.org/10.1016/j.ijheatmasstransfer.2017.06.077

[119] Zerilli FJ, Armstrong RW (1987). Dislocation-mechanics-based constitutive relations for material dynamics calculations. Journal of Applied Physics 61:1816–1825. https://doi.org/10.1063/1.338024

[120] Chamanfar A, Jahazi M, Gholipour J, et al (2014). Evolution of flow stress and microstructure during isothermal compression of Waspaloy. Materials Science and Engineering A 615:497–510. https://doi.org/10.1016/j.msea.2014.07.093

[121] Shen G, Semiatin SL, Shivpuri R (1995). Modeling microstructural development during the forging of Waspaloy. Metallurgical and Materials Transactions A 26:1795–1803. https://doi.org/10.1007/BF02670767

[122] Del Prete A, Filice L, Umbrello D (2013). Numerical simulation of machining nickel-based alloys. Procedia CIRP 8:540–545. https://doi.org/10.1016/j.procir.2013.06.147

[123] Umbrello D, Filice L, Rizzuti S, et al (2007). On the effectiveness of Finite Element simulation of orthogonal cutting with particular reference to temperature prediction. Journal of Materials Processing Technology 189:284–291. https://doi.org/10.1016/j.jmatprotec.2007.01.038

[124] Matykina E, Arrabal R, Valiev RZ, et al (2015). Electrochemical Anisotropy of

Nanostructured Titanium for Biomedical Implants. Electrochimica Acta 176:1221–1232. https://doi.org/10.1016/j.electacta.2015.07.128

[125] Aparicio C, Javier Gil F, Fonseca C, et al (2003). Corrosion behaviour of commercially pure titanium shot blasted with different materials and sizes of shot particles for dental implant applications. Biomaterials 24:263–273. https://doi.org/10.1016/S0142-9612(02)00314-9

[126] J.A. S, E. MJ, S. D, et al (2005). Analysis of Failed Commercially Pure Titanium Dental Implants : A Scanning. Journal of Periodontology 76:1092–1099. https://doi.org/10.1902/jop.2005.76.7.1092

[127] Zhou Q, Wang L, Zou CH (2017). Enhanced surface precipitates on ultrafine-grained titanium in physiological solution. Metals 7:. https://doi.org/10.3390/met7070245

[128] Colafemina JP, Jasinevicius RG, Duduch JG (2007). Surface integrity of ultra-precision diamond turned Ti (commercially pure) and Ti alloy (Ti-6Al-4V). Proceedings of the Institution of Mechanical Engineers, Part B: Journal of Engineering Manufacture 221:999–1006. https://doi.org/10.1243/09544054JEM798

[129] Cheng EH, Lin MJ, Tsai TL, Yeh NM (2012). Study on machining dental implants by whirling approach. Applied Mechanics and Materials 117–119:1506–1513. https://doi.org/10.4028/www.scientific.net/AMM.117-119.1506

[130] Kim JG, Enikeev NA, Seol JB, et al (2018). Superior Strength and Multiple Strengthening Mechanisms in Nanocrystalline TWIP Steel. Scientific Reports 8:1–10. https://doi.org/10.1038/s41598-018-29632-y

[131] Schneider M, George EP, Manescau TJ, et al (2020). Analysis of strengthening due to grain boundaries and annealing twin boundaries in the CrCoNi medium-entropy alloy. International Journal of Plasticity 124:155–169. https://doi.org/10.1016/j.ijplas.2019.08.009

[132] Wang C, Xuan FZ, Zhao P (2019). A dislocation-based constitutive model for the cyclic response of nanolath strengthened steels. International Journal of Mechanical Sciences 155:475–487. https://doi.org/10.1016/j.ijmecsci.2019.03.010

[133] Iijima D, Yoneyama T, Doi H, et al (2003). Wear properties of Ti and Ti-6Al-7Nb castings for dental prostheses. Biomaterials 24:1519–1524. https://doi.org/10.1016/S0142-9612(02)00533-1

[134] Miura-Fujiwara E, Okumura T, Yamasaki T (2015). Frictional and wear behavior of commercially pure Ti, Ti-6Al-7Nb, and SUS316L stainless steel in artificial saliva at 310K. Materials Transactions 56:1648–1657. https://doi.org/10.2320/matertrans.M2015094

[135] Salem AA, Kalidindi SR, Semiatin SL (2005). Strain hardening due to deformation twinning in α-titanium: Constitutive relations and crystal-plasticity modeling. Acta Materialia 53:3495–3502. https://doi.org/10.1016/j.actamat.2005.04.014

[136] Khan MK, Fitzpatrick ME, Hainsworth S V., et al (2011). Application of synchrotron X-ray diffraction and nanoindentation for the determination of residual stress fields around scratches. Acta Materialia 59:7508–7520. https://doi.org/10.1016/j.actamat.2011.08.034

[137] Chauhan A, Bergner F, Etienne A, et al (2017). Microstructure characterization and strengthening mechanisms of oxide dispersion strengthened (ODS) Fe-9%Cr and Fe-14%Cr extruded bars. Journal of Nuclear Materials 495:6–19. https://doi.org/10.1016/j.jnucmat.2017.07.060

[138] Sgambitterra E, Maletta C, Furgiuele F (2015). Temperature dependent local phase transformation in shape memory alloys by nanoindentation. Scripta Materialia 101:64–67. https://doi.org/10.1016/j.scriptamat.2015.01.020

[139] Cao S, Gu D, Shi Q (2017). Relation of microstructure, microhardness and underlying thermodynamics in molten pools of laser melting deposition processed TiC/Inconel 625 composites. Journal of Alloys and Compounds 692:758–769. https://doi.org/10.1016/j.jallcom.2016.09.098

[140] Sajadifar SV, Yapici GG (2014). Elevated temperature mechanical behavior of severely deformed titanium. Journal of Materials Engineering and Performance 23:1834–1844. https://doi.org/10.1007/s11665-014-0947-2

[141] Alexandrov I, Chembarisova R, Sitdikov V, Kazyhanov V (2008). Modeling of deformation behavior of SPD nanostructured CP titanium. Materials Science and Engineering A 493:170–175. https://doi.org/10.1016/j.msea.2007.11.073

[142] Kendig KL, Miracle DB (2002). Strengthening mechanisms of an Al-Mg-Sc-Zr alloy. Acta Materialia 50:4165–4175. https://doi.org/10.1016/S1359-6454(02)00258-6

[143] Liu K, Melkote SN (2006). Material strengthening mechanisms and their contribution to size effect in micro-cutting. Journal of Manufacturing Science and Engineering, Transactions of the ASME 128:730–738. https://doi.org/10.1115/1.2193548

[144] Anand RS, Patra K (2014). Modeling and simulation of mechanical micro-machining - A review. Machining Science and Technology 18:323–347. https://doi.org/10.1080/10910344.2014.925377

[145] Ucun I, Aslantasx K, Gökcxe B, Bedir F (2014). Effect of tool coating materials on surface roughness in micromachining of Inconel 718 super alloy. Proceedings of the Institution of Mechanical Engineers, Part B: Journal of Engineering Manufacture 228:1550–1562. https://doi.org/10.1177/0954405414522217

[146] Yuan S, Lin N, Zou J, et al (2020). In-situ fabrication of gradient titanium oxide ceramic coating on laser surface textured Ti6Al4V alloy with improved mechanical property and wear performance. Vacuum 176:109327. https://doi.org/10.1016/j.vacuum.2020.109327

[147] Wang B, Xiao X, Astakhov VP, Liu Z (2020). A quantitative analysis of the transition of fracture mechanisms of Ti6Al4V over a wide range of stress triaxiality and strain rate. Engineering Fracture Mechanics 231:107020. https://doi.org/10.1016/j.engfracmech.2020.107020

[148] Ma R, Liu Z, Wang W, et al (2020). Microstructures and mechanical properties of Ti6Al4V-Ti48Al2Cr2Nb alloys fabricated by laser melting deposition of powder mixtures. Materials Characterization 110321. https://doi.org/10.1016/j.matchar.2020.110321

[149] Ding H, Shin YC (2012). Dislocation density-based modeling of subsurface grain refinement with laser-induced shock compression. Computational Materials Science 53:79–88. https://doi.org/10.1016/j.commatsci.2011.08.038

[150] Zenasni Z, Haterbouch M, Atmani Z, et al (2019). Physics-based plasticity model incorporating microstructure changes for severe plastic deformation. Comptes Rendus - Mecanique 347:601–614. https://doi.org/10.1016/j.crme.2019.06.001

[151] Reuber C, Eisenlohr P, Roters F, Raabe D (2014). Dislocation density distribution around an indent in single-crystalline nickel: Comparing nonlocal crystal plasticity finite-element

predictions with experiments. Acta Materialia 71:333–348. https://doi.org/10.1016/j.actamat.2014.03.012

[152] Roters F, Eisenlohr P, Hantcherli L, et al (2010). Overview of constitutive laws, kinematics, homogenization and multiscale methods in crystal plasticity finite-element modeling: Theory, experiments, applications. Acta Materialia 58:1152–1211. https://doi.org/10.1016/j.actamat.2009.10.058

[153] Jawahir IS, Brinksmeier E, M'Saoubi R, et al (2011). Surface integrity in material removal processes: Recent advances. CIRP Annals - Manufacturing Technology 60:603–626. https://doi.org/10.1016/j.cirp.2011.05.002

[154] Messerschmidt U (2010). Dislocation dynamics during plastic deformation

[155] Lee WS, Lin CF, Chen TH, Chen HW (2011). Dynamic mechanical behaviour and dislocation substructure evolution of Inconel 718 over wide temperature range. Materials Science and Engineering A 528:6279–6286. https://doi.org/10.1016/j.msea.2011.04.079

[156] Ni H, Alpas AT (2003). Sub-micrometer structures generated during dry machining of copper. Materials Science and Engineering A 361:338–349. https://doi.org/10.1016/S0921-5093(03)00530-6

[157] Furukawa M, Horita Z, Nemoto M, et al (1996). Microhardness measurements and the hall-petch relationship in an Al-Mg alloy with submicrometer grain size. Acta Materialia 44:4619–4629. https://doi.org/10.1016/1359-6454(96)00105-X

[158] Conrad H (1970). The athermal component of the flow stress in crystalline solids. Materials Science and Engineering 6:265–273. https://doi.org/10.1016/0025-5416(70)90054-6

[159] Artz E (1998). Size effects in materials due to microstructural and dimensional constraints: a comparative review. Acta Materialia 46:5611–5626. https://doi.org/10.1016/s0957-5820(99)70836-0

[160] Ohno T, Watanabe R, Fukui T, Tanaka K (1988). Isothermal forging of Waspaloy in air with a new die material. Transactions of the Iron and Steel Institute of Japan 28:958–964. https://doi.org/10.2355/isijinternational1966.28.958

[161] Bergström Y (1970). A dislocation model for the stress-strain behaviour of polycrystalline α-Fe with special emphasis on the variation of the densities of mobile and immobile dislocations. Materials Science and Engineering 5:193–200. https://doi.org/10.1016/0025-5416(70)90081-9

[162] Bergstrom Y (1971). A Dislocation Model for the Strain-Ageing Behaviour of Steel. Materials Science and Engineering 101–110

[163] Estrin Y (1998). Dislocation theory based constitutive modelling: Foundations and applications. Journal of Materials Processing Technology 80–81:33–39. https://doi.org/10.1016/S0924-0136(98)00208-8

[164] Schoeck G (1956). Dislocation Theory of Plasticity of Metals. Advances in Applied Mechanics 4:229–279. https://doi.org/10.1016/S0065-2156(08)70374-0

[165] Holt DL (1970). Dislocation cell formation in metals. Journal of Applied Physics 41:3197–3201. https://doi.org/10.1063/1.1659399

[166] Bergström Y, Hallén H (1982). An improved dislocation model for the stress-strain behaviour of polycrystalline α-Fe. Materials Science and Engineering 55:49–61.

https://doi.org/10.1016/0025-5416(82)90083-0

[167] Johnston TL, Feltner CE (1970). Grain size effects in the strain hardening of polycrystals. Metallurgical and Materials Transactions 1:1161–1167. https://doi.org/10.1007/BF02900226

[168] Scattergood RO, Koch CC (1992). A modified model for hall-petch behavior in nanocrystalline materials. Scripta Metallurgica et Materiala 27:1195–1200. https://doi.org/10.1016/0956-716X(92)90598-9

[169] Thomas GJ, Siegel RW, Eastman JA (1990). Grain boundaries in nanophase palladium: high resolution electron microscopy and image simulation. 24:201–206

[170] Wunderlich W, Ishida Y, Maurer R (1990). HREM-studies of the microstructure of nanocrystalline palladium. Scripta Metallurgica et Materiala 24:403–408. https://doi.org/10.1016/0956-716X(90)90279-P

[171] Shen G, Rollins J, Furrer D (1996). Microstructure Modeling of Forged Waspalay Discs. Superalloys 1996 613–620. https://doi.org/\url{10.7449/1996/Superalloys{\textunderscore }1996{\textunderscore }613{\textunderscore }620}

[172] D. Caillard JLM (2003). Thermally Activated Mechanisms in Crystal Plasticity, Volume 8. Pergamon, Oxford

[173] Kocks UF (1970). The relation between polycrystal deformation and single-crystal deformation. Metallurgical and Materials Transactions 1:1121–1143. https://doi.org/10.1007/BF02900224

[174] Chen YJ, Li YJ, Walmsley JC, et al (2010). Microstructure evolution of commercial pure titanium during equal channel angular pressing. Materials Science and Engineering A 527:789–796. https://doi.org/10.1016/j.msea.2009.09.005

[175] Dini G, Ueji R, Najafizadeh A, Monir-Vaghefi SM (2010). Flow stress analysis of TWIP steel via the XRD measurement of dislocation density. Materials Science and Engineering A 527:2759–2763. https://doi.org/10.1016/j.msea.2010.01.033

[176] Hayashi M, Yoshimura H, Ishii M, Harada H (1994). Recrystallization behavior of commercially pure titanium during hot rolling. Nippon Steel Tech. Rep. 64–68

[177] Sajadifar SV, Yapici GG (2014). Workability characteristics and mechanical behavior modeling of severely deformed pure titanium at high temperatures. Materials and Design 53:749–757. https://doi.org/10.1016/j.matdes.2013.07.057

[178] Gao C, Lu W (2012). Thermomechanical response of commercially pure titanium under large plastic deformation at high strain rates. Advanced Materials Research 548:174–178. https://doi.org/10.4028/www.scientific.net/AMR.548.174

[179] Naik SN, Walley SM (2020). The Hall–Petch and inverse Hall–Petch relations and the hardness of nanocrystalline metals. Journal of Materials Science 55:2661–2681. https://doi.org/10.1007/s10853-019-04160-w

[180] Regazzoni G, Kocks UF, Follansbee PS (1987). Dislocation kinetics at high strain rates. Acta Metallurgica 35:2865–2875. https://doi.org/10.1016/0001-6160(87)90285-9

[181] Chen Y, Gao N, Sha G, et al (2016). Microstructural evolution, strengthening and thermal stability of an ultra fine-grained Al e Cu e Mg alloy. Acta Materialia 109:202–212.

https://doi.org/10.1016/j.actamat.2016.02.050

[182] Du M, Cheng Z, Wang S (2019). Finite element modeling of friction at the tool-chip-workpiece interface in high speed machining of Ti6Al4V. International Journal of Mechanical Sciences 163:. https://doi.org/10.1016/j.ijmecsci.2019.105100

[183] Koyee RD, Schmauder S, Heisel U, Eisseler R (2015). Numerical modeling and optimization of machining duplex stainless steels. Production and Manufacturing Research 3:36–83. https://doi.org/10.1080/21693277.2014.990539

[184] Kumar P, Chakkingal U (2008). Workability limits of commercial purity titanium subjected to equal channel angular pressing. Materials Science Forum 584-586 PA:275–280. https://doi.org/10.4028/www.scientific.net/msf.584-586.275

[185] Yang Z, Welzel U (2005). Microstructure-microhardness relation of nanostructured Ni produced by high-pressure torsion. Materials Letters 59:3406–3409. https://doi.org/10.1016/j.matlet.2005.05.077

[186] Liu HW (1999). A dislocation barrier model for fatigue limit - As determined by crack non-initiation and crack non-propagation. International Journal of Fracture 96:331–345. https://doi.org/10.1023/A:1018654430344

[187] Duryat RS, Kim CU (2014). A model-inspired phenomenology constitutive equation for the temperature-dependence of flow stress at confined dimension II. IOP Conference Series: Materials Science and Engineering 58:. https://doi.org/10.1088/1757-899X/58/1/012021

[188] Tanaka M, Higashida K (2016). Temperature dependence of effective stress in severely deformed ultralow-carbon steel. Philosophical Magazine 96:1979–1992. https://doi.org/10.1080/14786435.2016.1183828

[189] Blaschke DN, Mottola E, Preston DL (2020). Dislocation drag from phonon wind in an isotropic crystal at large velocities. Philosophical Magazine 100:571–600. https://doi.org/10.1080/14786435.2019.1696484

[190] Babu B, Lindgren LE (2013). Dislocation density based model for plastic deformation and globularization of Ti-6Al-4V. International Journal of Plasticity 50:94–108. https://doi.org/10.1016/j.ijplas.2013.04.003

[191] Quan GZ, Luo GC, Liang JT, et al (2015). Modelling for the dynamic recrystallization evolution of Ti-6Al-4V alloy in two-phase temperature range and a wide strain rate range. Computational Materials Science 97:136–147. https://doi.org/10.1016/j.commatsci.2014.10.009

[192] Matsumoto H, Velay V (2017). Mesoscale modeling of dynamic recrystallization behavior, grain size evolution, dislocation density, processing map characteristic, and room temperature strength of Ti-6Al-4V alloy forged in the (α+β) region. Journal of Alloys and Compounds 708:404–413. https://doi.org/10.1016/j.jallcom.2017.02.285

[193] Long Y, Zhang H, Wang T, et al (2013). High-strength Ti-6Al-4V with ultrafine-grained structure fabricated by high energy ball milling and spark plasma sintering. Materials Science and Engineering A 585:408–414. https://doi.org/10.1016/j.msea.2013.07.078

[194] Zhang Z, Ódor É, Farkas D, et al (2020). Dislocations in Grain Boundary Regions: The Origin of Heterogeneous Microstrains in Nanocrystalline Materials. Metallurgical and Materials Transactions A: Physical Metallurgy and Materials Science 51:513–530. https://doi.org/10.1007/s11661-019-05492-7

[195] Umbrello D, Bordin A, Imbrogno S, Bruschi S (2017). 3D finite element modelling of surface modification in dry and cryogenic machining of EBM Ti6Al4V alloy. CIRP Journal of Manufacturing Science and Technology 18:92–100. https://doi.org/10.1016/j.cirpj.2016.10.004

[196] Astakhov VP, Joksch S (2012). Metalworking fluids (MWFs) for cutting and grinding. Woodhead Publishing

[197] Filice L, Micari F, Rizzuti S, Umbrello D (2007). A critical analysis on the friction modelling in orthogonal machining. International Journal of Machine Tools and Manufacture 47:709–714. https://doi.org/10.1016/j.ijmachtools.2006.05.007

[198] Courbon C, Pusavec F, Dumont F, et al (2013). Tribological behaviour of Ti6Al4V and Inconel718 under dry and cryogenic conditions - Application to the context of machining with carbide tools. Tribology International 66:72–82. https://doi.org/10.1016/j.triboint.2013.04.010

[199] Umbrello D (2008). Finite element simulation of conventional and high speed machining of Ti6Al4V alloy. Journal of Materials Processing Technology 196:79–87. https://doi.org/10.1016/j.jmatprotec.2007.05.007

[200] Krishnamurthy G, Bhowmick S, Altenhof W, Alpas AT (2017). Increasing efficiency of Ti-alloy machining by cryogenic cooling and using ethanol in MRF. CIRP Journal of Manufacturing Science and Technology 18:159–172. https://doi.org/10.1016/j.cirpj.2017.01.001

[201] Schoop J, Sales WF, Jawahir IS (2017). High speed cryogenic finish machining of Ti-6Al4V with polycrystalline diamond tools. Journal of Materials Processing Technology 250:1–8. https://doi.org/10.1016/j.jmatprotec.2017.07.002

[202] Jawahir IS, Attia H, Biermann D, et al (2016). Cryogenic manufacturing processes. CIRP Annals - Manufacturing Technology 65:713–736. https://doi.org/10.1016/j.cirp.2016.06.007

[203] Lindgren LE, Hao Q, Wedberg D (2017). Improved and simplified dislocation density based plasticity model for AISI 316 L. Mechanics of Materials 108:68–76. https://doi.org/10.1016/j.mechmat.2017.03.007

[204] Liang X, Liu Z, Wang B, Hou X (2018). Modeling of plastic deformation induced by thermo-mechanical stresses considering tool flank wear in high-speed machining Ti-6Al-4V. International Journal of Mechanical Sciences 140:1–12. https://doi.org/10.1016/j.ijmecsci.2018.02.031

[205] Razanica S, Malakizadi A, Larsson R, et al (2020). FE modeling and simulation of machining Alloy 718 based on ductile continuum damage. International Journal of Mechanical Sciences 171:105375. https://doi.org/10.1016/j.ijmecsci.2019.105375

[206] Hua J, Shivpuri R (2004). Prediction of chip morphology and segmentation during the machining of titanium alloys. Journal of Materials Processing Technology 150:124–133. https://doi.org/10.1016/j.jmatprotec.2004.01.028

[207] Komanduri R, Brown RH (1981). On the mechanics of chip segmentation in machining. Journal of Manufacturing Science and Engineering, Transactions of the ASME 103:33–51. https://doi.org/10.1115/1.3184458

[208] Pan Z, Feng Y, Liang SY (2017). Material microstructure affected machining: A review.

Manufacturing Review 4:. https://doi.org/10.1051/mfreview/2017004

[209] Wang Q, Liu Z (2016). Plastic deformation induced nano-scale twins in Ti-6Al-4V machined surface with high speed machining. Materials Science and Engineering A 675:271–279. https://doi.org/10.1016/j.msea.2016.08.076

[210] Wang CT, Gao N, Gee MG, et al (2012). Effect of grain size on the micro-tribological behavior of pure titanium processed by high-pressure torsion. Wear 280–281:28–35. https://doi.org/10.1016/j.wear.2012.01.012

[211] Liu S, Qian L, Meng J, et al (2017). Simultaneously increasing both strength and ductility of Fe-Mn-C twinning-induced plasticity steel via Cr/Mo alloying. Scripta Materialia 127:10–14. https://doi.org/10.1016/j.scriptamat.2016.08.034

[212] Peng Z, Li J, Yan P, et al (2018). Experimental and simulation research on micro-milling temperature and cutting deformation of heat-resistance stainless steel. International Journal of Advanced Manufacturing Technology 95:2495–2508. https://doi.org/10.1007/s00170-017-1091-6

[213] Pal DK, Basu SK (1969). Hot machining of Austenitic Manganese Steel by Shaping. International Journal of Machine Tools and Manufacture 11:45–61

[214] Parida AK, Maity K (2018). Experimental investigation on tool life and chip morphology in hot machining of Monel-400. Engineering Science and Technology, an International Journal 21:371–379. https://doi.org/10.1016/j.jestch.2018.04.003

[215] Baili M, Wagner V, Dessein G, et al (2011). An experimental investigation of hot machining with induction to improve Ti-5553 machinability. Applied Mechanics and Materials 62:67–76. https://doi.org/10.4028/www.scientific.net/AMM.62.67

[216] Niu Q, Chen M, Ming W, An Q (2013). Evaluation of the performance of coated carbide tools in face milling TC6 alloy under dry condition. International Journal of Advanced Manufacturing Technology 64:623–631. https://doi.org/10.1007/s00170-012-4043-1

[217] Hong SY, Ding Y, Jeong W cheol (2001). Friction and cutting forces in cryogenic machining of Ti-6Al-4V. International Journal of Machine Tools and Manufacture 41:2271–2285. https://doi.org/10.1016/S0890-6955(01)00029-3

[218] Kiran Sagar C, Kumar T, Priyadarshini A, Kumar Gupta A (2019). Prediction and optimization of machining forces using oxley's predictive theory and RSM approach during machining of WHAs. Defence Technology 15:923–935. https://doi.org/10.1016/j.dt.2019.07.004

[219] Zhao Z, To S, Zhu Z, Yin T (2020). A theoretical and experimental investigation of cutting forces and spring back behaviour of Ti6Al4V alloy in ultraprecision machining of microgrooves. International Journal of Mechanical Sciences 169:105315. https://doi.org/10.1016/j.ijmecsci.2019.105315

[220] Tasdelen B, Thordenberg H, Olofsson D (2008). An experimental investigation on contact length during minimum quantity lubrication (MQL) machining. Journal of Materials Processing Technology 203:221–231. https://doi.org/10.1016/j.jmatprotec.2007.10.027

[221] Kumar Sharma A, Kumar Tiwari A, Rai Dixit A, Kumar Singh R (2020). Measurement of machining forces and surface roughness in turning of AISI 304 steel using alumina-MWCNT hybrid nanoparticles enriched cutting fluid. Measurement: Journal of the International Measurement Confederation 150:107078.

https://doi.org/10.1016/j.measurement.2019.107078

[222] Huang Y, Prangnell PB (2008). The effect of cryogenic temperature and change in deformation mode on the limiting grain size in a severely deformed dilute aluminium alloy. Acta Materialia 56:1619–1632. https://doi.org/10.1016/j.actamat.2007.12.017

[223] Zou J, Stein N, Boulanger C, et al (2007). Grain Refinement and Improved Hardness/Corrosion Balance by Pulsed Electron Beam Surface Treatment of a FeAl Alloy. Scripta Materialia 58:19–22. https://doi.org/10.1051/names2007013